Technische Universität München
Fakultät für Luftfahrt, Raumfahrt und Geodäsie
Lehrstuhl für Methodik der Fernerkundung

RETRIEVAL OF GLACIOLOGICAL PARAMETERS FROM SAR DATA AND MASS BALANCE MODELLING OF GLACIERS IN NORTHEAST GREENLAND

Lukas Raphael Krieger

Vollständiger Abdruck der von der Fakultät für Luftfahrt, Raumfahrt und Geodäsie der Technischen Universität München zur Erlangung des akademischen Grades eines
Doktor-Ingenieurs (Dr.-Ing.)
genehmigten Dissertation.

Vorsitzender:

Prof. Dr. Florian Seitz

Prüfende der Dissertation:

1. Hon.-Prof. Dr. rer. nat. Michael Eineder
2. Prof. Dr.-Ing. habil. Richard H. G. Bamler
3. Prof. Dr.-Ing. Martin Horwath, Technische Universität Dresden

Die Dissertation wurde am 16.04.2020 bei der Technischen Universität München eingereicht und durch die Fakultät für Luftfahrt, Raumfahrt und Geodäsie am 10.09.2020 angenommen.

Lukas Raphael Krieger: *Retrieval of glaciological parameters from SAR data and mass balance modelling of glaciers in Northeast Greenland,* This work represents a cumulative dissertation 2021-02-02

ABSTRACT

Spaceborne synthetic aperture radar (SAR) and interferometric SAR (InSAR) systems have evolved into widely applied tools for remote sensing of the Earth's ice sheets since the launch of the European Remote Sensing Satellites (ERSs) in the 1990s. These satellite systems are used to document the reaction of glaciers and ice sheets to climate change and help predict global sea level rise. While first SAR acquisitions have been sparse and with coarse resolution, recent satellite missions like TerraSAR-X (TSX), TanDEM-X (TDM) or Sentinel-1 are now used operationally to derive glaciological parameters of interest at the individual glacier scale up to several times per week.

Time-series of these parameters describe the dynamic behaviour of the ice sheets and provide insight to study the effect of environmental forcing caused by the ocean and the atmosphere. The ice sheet mass balance is an important result of these observations which describes how much ice mass is lost or gained during a specific time period. There are two frequently used approaches to estimate the mass changes of individual glaciers with remote sensing methods. One is to convert measured volume changes to mass change with the help of modelled ice and firn densities. In the other approach, a regional climate model is combined with ice velocities to capture all processes of mass gain or loss on the glacier surface and the export of ice separately. In both methods, SAR and InSAR measurements play key roles. However, InSAR acquisitions have not yet contributed to volumetric mass balance measurements at large ice sheet outlet glaciers. At these, the surface elevation change has been mainly derived with altimeters and InSAR was only used to analyse dynamic changes of the ice surface. InSAR derived mass balance is only available for comparatively small glaciers.

The focus of this cumulative dissertation is to develop a framework for deriving volumetric mass changes on ice sheets with the help of InSAR measurements and to study dynamic and geometric changes in the Northeast Greenland region. While major outlet glaciers in the west and the south-east of Greenland have shown dramatic speed-ups and increased mass loss since the late 1990s, the Northeast Greenland region experienced a delayed start of these changes. In the present thesis, the transformations caused by the increased atmospheric and oceanic warming are documented in time-series of ice velocities and surface elevation change. Additionally, an algorithm working towards the automatic delineation of glacier calving fronts in SAR imagery was developed. Specifically for the ice shelf of Nioghalvfjersfjorden (79North) the grounding line was observed since 2010 and a thinning of the floating ice tongue caused by increased oceanic warming was measured.

To be able to partition SAR measurements to the individual glacier level, a modified watershed algorithm has been developed which delineates individual catchments for outlet glaciers on the ice sheet. The methodology has been applied to the Northeast Greenland region, forming 31 catchments with the help of measured ice flow directions from SAR offset tracking. The partitioning reveals in particular the large basins of the outlet glaciers Zachariæ Isstrøm (ZI) and 79North of the Northeast Greenland

Ice Stream (NEGIS) draining approx. 12% of the total Greenland Ice Sheet (GrIS) area.

Finally, the geodetic mass balance was derived for two major outlet glaciers ZI and 79North from surface elevation change measurements by the CryoSat-2 (CS-2) radar altimeter in combination with time-series of high resolution TDM digital elevation models (DEMs). In the time between Jan. 2011 and Dec. 2013, ZI has lost $3.59 \pm 1.15\,\mathrm{Gt\,a^{-1}}$ and has shown considerable calving front retreat of 2.1 km. Less mass loss has been observed at 79North for the same time frame. Its measured mass balance amounts to $-1.01 \pm 0.95\,\mathrm{Gt\,a^{-1}}$. Additionally, the floating ice tongue at 79North has thinned at an average rate of $5.4\,\mathrm{m\,a^{-1}}$ while the grounding line has remained stable over the time period. With the developed synergistic approach, the uncertainties compared to previously reported geodetic mass balance estimations of individual outlet glaciers have been reduced.

ZUSAMMENFASSUNG

Satellitengestütztes Synthetisches Apertur Radar (SAR) und die Radarinterferometrie (InSAR) sind spätestens seit dem Start der European Remote Sensing Satellites (ERSs) in den 90er Jahren weit verbreitete Werkzeuge, die zur Fernerkundung von Eisschilden benutzt werden. Mit ihnen können die Veränderungen von Gletschern und Eisschilden als Reaktion auf den Klimawandel beobachtet werden und sie helfen mit ihren Messungen den globalen Meeresspiegelanstieg vorherzusagen. Während die ersten SAR Missionen eine niedrige Auflösung hatten und noch nicht regelmäßig in der Lage waren große Gebiete abzudecken, können heute neuartige Missionen wie TerraSAR-X (TSX), TanDEM-X (TDM) oder Sentinel-1 mehrmals pro Woche für die operationelle Ableitung von glaziologischen Parametern von einzelnen Gletschern benutzt werden.

Zeitreihen dieser Parameter beschreiben die dynamische Entwicklung der Gletscher und geben Aufschluss darüber welche Auswirkungen die Veränderungen der Atmosphäre oder der Ozeane auf die Eisschilde haben. Ein wichtiges Ergebnis dieser Beobachtungen ist die Massenbilanz, welche beschreibt wie viel Eismasse in einem bestimmten Zeitraum abgeschmolzen ist oder angesammelt wurde. Häufig werden für die Bestimmung der Massenbilanz zwei unabhängige Fernerkundungsmethoden benutzt. In der ersten Herangehensweise wird aus gemessenen Eishöhenänderungen und den daraus resultierenden Volumenänderungen mit Hilfe von modellierten Firndichten die Massenbilanz abgeleitet. Die zweite Methode kombiniert regionale Klimamodelle mit Eisgeschwindigkeitsmessungen, um alle Prozesse des Massenzugewinns und des Verlust von Eis zu erfassen. Dabei spielen SAR und InSAR Messungen jeweils eine wichtige Rolle. InSAR Eisvolumenänderungen haben jedoch bis jetzt nicht zu der Bestimmung der Massenbilanz von großen Ausflussgletschern der Eisschilde beigetragen. Für diese wurde bisher nur die Satellitenaltimetrie benutzt und aus InSAR abgeleitete Massenbilanzen waren nur für vegleichsweise kleine Gletscher verfügbar. Zudem wurden InSAR Volumenänderungen nur dazu benutzt, um dynamische Veränderungen zu analysieren nicht aber die Massenänderung zu bestimmen.

Der Fokus dieser publikationsbasierten Dissertation liegt auf der Entwicklung einer Methode um Massenbilanzen für einzelne Gletscher auf Eisschilden über Volumenänderungen mit InSAR zu messen und dynamische und geometrische Änderungen in Nordost Grönland zu untersuchen. Während große Ausflussgletscher im Westen und Südosten Grönlands bereits seit den 90er Jahren dramatische Beschleunigungen der Eisflussgeschwindigkeit und erhöhten Eismassenverlust aufweisen, haben diese Prozesse in Nordost Grönland später eingesetzt. In der vorliegenden Arbeit wurden diese Veränderungen in Zeitreihen von Eisgeschwindigkeit und Eishöhen dokumentiert, die durch die Erwärmung der Atmosphäre und des Ozeans hervorgerufen wurden. Zusätzlich wurde ein Algorithmus entwickelt um die Kalbungsfront von Ausflussgletschern automatisch aus SAR Aufnahmen abzuleiten. Im speziellen Fall von Nioghalvfjersfjorden (79North) wurde die Eisaufsetzlinie der frei

schwimmenden Eiszunge seit 2010 beobachtet und ein Eisdickenverlust aufgrund der Ozeanerwärmung festgestellt.

Um die SAR Messungen einzelnen Gletschern zuordnen zu können wurde ein modifizierter Wasserscheiden Algorithmus für die Bestimmung der Eiseinzugsgebiete von Ausflussgletschern auf Eisschilden entwickelt. Diese Methode wurde auf das Gebiet in Nordost Grönland angewandt und mit Hilfe der aus SAR Offset Tracking gemessenen Eisflussrichtung wurden 31 Eiseinzugsgebiete bestimmt. Diese Einteilung offenbart die besonders großen Eiseinzugsgebiete der Ausflussgletscher Zachariæ Isstrøm (ZI) und 79North des Nordostgrönländischen Eisstroms (NEGIS) die zusammen etwa 12% der Grönländischen Eisfläche einnehmen.

Zuletzt wurde die Massenbilanz mit der geodätischen Methode für ZI und 79North mit Hilfe von Eishöhenänderungen bestimmt. Dazu wurden kombinierte Messungen des Radaraltimeters CryoSat-2 (CS-2) zusammen mit Zeitreihen aus hochauflösenden Höhenmodellen von TDM verwendet. Zwischen Jan. 2011 und Dez. 2013 hat sich die Kalbungsfront von ZI durchschnittlich um 2.1 km zurückgezogen und ZI hat $3.59 \pm 1.15\,\mathrm{Gt\,a^{-1}}$ an Eismasse verloren. Im selben Zeitraum hingegen hat 79North mit $1.01 \pm 0.95\,\mathrm{Gt\,a^{-1}}$ weniger Masse verloren. Die Dicke der schwimmende Eiszunge von 79North hat sich um $5.4\,\mathrm{m\,a^{-1}}$ verringert während die Eisaufsetzline an einer stabilen Position verblieben ist. Durch die Entwicklung eines synergetischen Ansatzes wurden die Unsicherheiten gegenüber vorhergehenden geodätischen Abschätzungen individueller Gletscher Massenbilanzen verringert.

ACKNOWLEDGMENTS

I would like to express my deepest gratitude to Dr. Dana Floricioiu, who has supervised my thesis from the very beginning. She introduced me to many scientists in the field and enabled me to take part in conferences around the world. Her excitement to work in the field of remote sensing of glaciology creates an enjoyable atmosphere to work in. For all the effort she took I am extremely thankful.

I want to specially thank Prof. Michael Eineder who employed me at the IMF SAR department and always has an open door for discussions. I am also very grateful for Prof. Richard Bamler for enabling me to enrol as a PhD student at TU Munich and asking the right questions to improve my research. Finally, I also want to thank Prof. Martin Horwath for accepting to be an external reviewer and Prof. Florian Seitz for acting as a chairman in my defense, in a time where it wasn't easy to organise an oral exam.

I am also very grateful to all my colleagues at DLR who create a work environment that I can enjoy on a daily basis. In particular I want to thank Helko Breit, who always found spare time to explain SAR concepts to me as a complete novice coming from a different field. Also, I want to extend my special thanks to Dr. Thomas Fritz and Dr. Marie Lachaise who were always there to answer my many questions about TanDEM-X and our interferometric processor.

My (ex-)glaciology colleagues deserve a special mention and thanks. Michael, Tanvir, Wael and Yuting contributed to a team which is both supportive and, on whose knowledge, I could always rely. Together we followed many interesting research directions in a topic which concerns each and every one.

Of all the colleagues at DLR Erling needs a special mention. I couldn't have wished for a better office mate. You were always there when I needed someone to talk to - be it personal or work related. I know you had a lot to endure with me sitting in the same room. I am thinking of my (sometimes weird but mostly) good music taste and my special ventilator setup to deal with the summer heat waves.

I also want to offer my thanks to Christian for the necessary breaks especially towards the finalisation of the thesis, Eike for the occasional ride home (even if I had to endure Andreas Gabalier), Georg for an unforgettable Karaoke night, Gerald for letting me sleep on his floor in Tokyo, Homa for the help anytime my math or SAR knowledge didn't suffice (and also all the advice that is not work related), Matthias for all the interesting (football) discussions in our daily S-Bahn commute, Sina for the great banter that I enjoy the most, Tobi & Sandra for the best summer school memories and sharing their office space whenever I worked at TUM.

Away from my work environment I want to thank Basti, Tobi and the rest of the climbing crew for the countless evenings and yearly vacations that I wouldn't want to miss, as well as, my flatmates Alexa, Becky, Ene, Tabea, Nicki, Puschi and Stefan for apparently being a very Dr.-friendly WG.

Especially thankful I am to my caring and supportive girlfriend Franzi. I am very lucky and grateful to have you.

Above all I want to thank my mother Monika who always supported me venturing off in different directions and who I can always rely on. Also, I want to offer my thanks to my aunt Lisa and my sisters Vroni, Charlie and Pauline who are the best sisters ever. I'm glad to have had you all by my side on this journey.

The list above is incomplete, but also each and every one that I haven't mentioned needs to be thanked. My activities, meetings, travel, laughter and good memories are the things I remembered and looked forward to whenever I had a stressful time at work.

CONTENTS

ABBREVIATIONS

79North	Nioghalvfjersfjorden	iii, v, 2, 7, 18, 31, 70
AIS	Antarctic Ice Sheet	22
AOTIM	Arctic Ocean Tidal Inverse Model	44
ASAR	Advanced Synthetic Aperture Radar	24
ASTER	Advanced Spaceborne Thermal Emission and Reflection Radiometer	24
ATM	Airborne Topographic Mapper	26, 53
AWI	Alfred-Wegener-Institut	62
CATS	Circum-Antarctic Tidal Simulation	44
CCI	Climate Change Initiative	21, 45, 72
CNN	convolutional neural network	42
CS-2	CryoSat-2	iv, 19, 55, 69
DEM	digital elevation model	iv, 12, 18, 32, 69
DFG	Deutsche Forschungsgemeinschaft	3
DInSAR	differential interferometric synthetic aperture radar (SAR) (InSAR)	20, 44, 70
DJ	Daugaard-Jensen	8, 40, 69
DLR	Deutsches Zentrum für Luft- und Raumfahrt	51
EBU	elastic bed uplift	12, 58
ERS	European Remote Sensing Satellite	iii, v, 17, 44, 70
ESA	European Space Agency	21, 45
ETM+	Enhanced Thematic Mapper	17
FC	firn compaction	12, 58
FDM	firn densification model	58
GIA	glacial isostatic adjustment	12, 58
GIMP	Greenland Ice Mapping Project	17, 46
GLAS	Geoscience Laser Altimeter System	18
GLIMS	Global Land Ice Measurements from Space	18
GRACE	Gravity Recovery and Climate Experiment	xi, 11, 17, 28

GRACE-FO	Gravity Recovery and Climate Experiment (GRACE)-Follow-On	11
GrIS	Greenland Ice Sheet	iv, 1, 6, 17, 58, 69
HEM	height error map	52
HG	Helheim-Gletscher	26
HoA	height of ambiguity	14, 53
ICESat	Ice, Cloud and land Elevation Satellite	18, 60, 73
IMAU	Institute for Marine and Atmospheric research Utrecht	58
IMBIE	Ice sheet Mass Balance Inter-comparison Exercise	18
InSAR	interferometric SAR	iii, xi, 1, 5, 20, 44, 69
ITP	Interferometric TDM Processor	51
JI	Jakobshavn Isbræ	26
LOS	line of sight	24
LRM	low resolution mode	62
MAI	multiple-aperture InSAR	24
MCoRDS	Multichannel Coherent Radar Depth Sounder	46
MEaSUREs	Making Earth System Data Records for Use in Research Environments	21, 45
MODIS	Moderate Resolution Imaging Spectroradiometer	19
NCAR	National Center for Atmospheric Research	44, 45
NCEP	National Centers for Environmental Prediction	44, 45
NEGIS	Northeast Greenland Ice Stream	iii, 1, 7, 18, 31, 69
OCOG	offset center of gravity	62
OIB	Operation IceBridge	46, 73
PDF	probability density function	22
PolInSAR	polarimetric InSAR	27
PSI	persistent scatterer interferometry	15
RAA	repeat altimetry analysis	25, 55
RGI	Randolph Glacier Inventory	18, 69
ROA	ratio of averages	41
SAR	synthetic aperture radar	iii, xi, 1, 5, 17, 32, 69

SEC	surface elevation change	12, 25, 51, 70
SECR	surface elevation change rate	10, 52, 72
SIRAL	Synthetic Aperture Interferometric Radar Altimeter	25, 61
SLE	sea level equivalent	6, 38
SMB	surface mass balance	10, 28, 47, 71
SPIRIT	Satellite Pour l'Observation de la Terre (SPOT) 5 stereoscopic survey of Polar Ice: Reference Images and Topographies	26
SPOT	Satellite Pour l'Observation de la Terre	xii, 19
SRTM	Shuttle Radar Topography Mission	26
SSC	Single look Slant range Complex	46
TDM	TanDEM-X	iii, v, 2, 13, 18, 31, 69
TEC	total electron content	15
TFMRA	threshold first-maximum retracker	62
TSX	TerraSAR-X	iii, v, 2, 15, 21, 40, 69
VCR	volume change rate	57
VHR	very high resolution	26
ZI	Zachariæ Isstrøm	iii, vi, 7, 18, 31, 69

1 INTRODUCTION

1.1 SCIENTIFIC MOTIVATION

During the last few decades, the Greenland Ice Sheet (GrIS) has experienced strong environmental changes and mass loss (Mouginot et al., 2019; Shepherd et al., 2012). The most harsh and rapid of these changes have occurred particularly in the west and south-east of Greenland and have been well reported (Joughin et al., 2019; Kehrl et al., 2017; Moon et al., 2012). The northeast of Greenland experienced a later start of this transformation, which provided an excellent opportunity to track the ice sheet's reaction to a warming climate with high resolution satellites. The present work aims at observing the evolution of outlet glaciers in the study area shown in Figure 1.1 by utilising high-resolution synthetic aperture radar (SAR) data from the past and present.

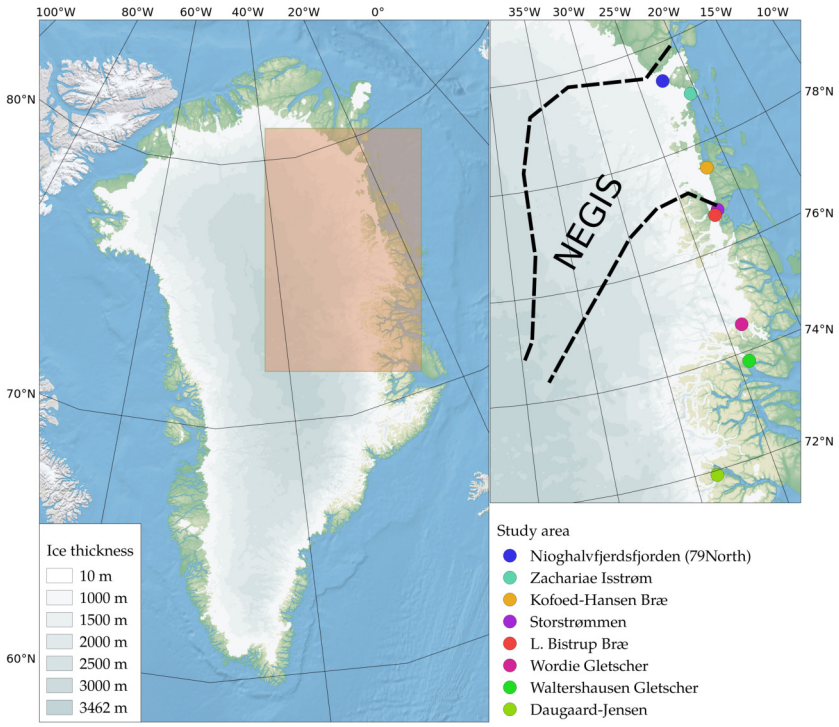

Figure 1.1: The area of Northeast Greenland with its 8 major outlet glaciers. The dominating ice flow feature in this sector is the Northeast Greenland Ice Stream (NEGIS). The ice thickness of the GrIS is taken from (Howat, Negrete, and Smith, 2014).

Due to regional climate warming the GrIS experiences enhanced surface melting and speed-up of its outlet glaciers (Broeke et al., 2009). Of scientific interest is therefore to accurately estimate discharge rates and glacier thinning from SAR and interferometric SAR (InSAR) in order to predict Greenland's mass loss and its contribution to global sea level rise (Meehl et al., 2007). At the same time, these

glaciological parameters benefit the improvement and validation of regional climate models (Tedesco et al., 2013).

With the continuous advance of satellite remote sensing missions it has become possible to observe vast, inaccessible regions like Northeast Greenland from space. The growing number of acquisitions and the large amount of data demands, however, to retrieve results with automatic or semi-automatic processing strategies. Also, the availability of new sensors requires that the current state of the art methods are replaced or adapted to make use of the higher resolutions, wider swaths and shorter repeat cycles.

1.2 RESEARCH OBJECTIVES

The research in this work is split into two parts. The first is to retrieve glaciological parameters for the Northeast Greenland region that are essential for modelling glacier mass balance. This will also be supported by the development of new or improved algorithms to retrieve those parameters. Secondly, the derived parameters are used for modelling glacier mass balance for individual glaciers in the Northeast Greenland region. To this end, a previously developed method for geodetic mass balance measurements of the Patagonian Ice Fields with TanDEM-X (TDM) is expanded to be applicable for large outlet glaciers of the ice sheet (Abdel Jaber, 2016). This allows to deliver volumetric glacier mass balance estimates for large ice sheet outlet glaciers with TDM InSAR measurements for the first time. The objectives of this thesis can be categorised as follows:

- **Objective 1: Derivation of ice velocity and surface elevation time-series**
  The surface elevation changes and velocity fields of the glaciers in the study area (see Figure 1.1) are key glaciological parameters which are derived from TerraSAR-X (TSX) and TDM data of the recent years (2010-2017). These parameters are essential for two different methods of mass balance estimation. In this work, focus is put on the largest major outlet glaciers in the Northeast Greenland region which are expected to experience dynamic changes in this time period. SAR data, in particular, is well suited for this purpose because the use of a microwave sensor enables reliable imaging of the glaciers throughout the year.

- **Objective 2: Determining the extent of individual glacier basins**
  The extent of the glacier basins and the short term changes of the calving front as well as the grounding line shall be updated. The frontal positions are needed in combination with terminus velocities for the retrieval of calving rates and fluxes. Calving represents an important component of ice mass loss. In the case of Nioghalvfjersfjorden (79North) the grounding line determines the line across which ice export is measured and it has to be examined separately with InSAR. Finally, the glacier drainage basins are needed to partition the results from Objective 1 to the individual glacier scale, because glacier reactions vary considerably depending on local glacier geometry or environmental forcing.

- **Objective 3: Mass balance modelling of individual glaciers in Northeast Greenland**
  By consolidating Objectives 1 and 2, the geodetic mass balance will be modelled for selected outlet glaciers in the study region and for the NEGIS. A

synergistic approach shall be developed that combines the capabilities of radar altimeters to measure subtle elevation change in the ice sheet interior with TDM measurements at the glacier terminus to provide complete volume change measurements for single glacier basins.

The research was conducted as part of the DFG project *Variations of ice sheet geometry, ice flow, and mass distribution in Northeast Greenland in the context of oceanic and atmospheric interactions (FL 848/1-1)* which aimed at investigating the geometric and dynamic variability of the ice sheet. The project partners at TU Dresden compiled the used altimetry products which have been combined with the SAR based results outlined in the following.

1.3 THESIS OUTLINE

Following the motivation and research objectives addressed in this introduction, the necessary fundamentals in glaciology and the concepts of modelling glacier mass balance are briefly introduced in Chapter 2. Chapter 3 focuses on state of the art methods that are used to derive essential glaciological parameters with a variety of sensors. Previous estimates of Greenland mass balance are presented here. Chapter 4 summarises the content of the scientific contributions which are compiled in this cumulative thesis. Eventually, future research directions and conclusions are presented in Chapter 5.

The cumulative dissertation summarises the content of two peer-reviewed journal papers:

- **Krieger, L.**, D. Floricioiu, and N. Neckel (2020). "Drainage Basin Delineation for Outlet Glaciers of Northeast Greenland Based on Sentinel-1 Ice Velocities and TanDEM-X Elevations." In: Remote Sensing of Environment (Krieger, Floricioiu, and Neckel, 2020), Appendix A

- **Krieger, L.**, U. Strößenreuther, V. Helm, D. Floricioiu, and M. Horwath (2020). "Synergistic Use of Single-Pass Interferometry and Radar Altimetry to Measure Mass Loss of NEGIS Outlet Glaciers between 2011 and 2014." In: Remote Sensing (Krieger et al., 2020), Appendix B

Two peer-reviewed journal papers are included in which the contributions as co-author have been relevant to the research objectives:

- Mayer, C., J. Schaffer, T. Hattermann, D. Floricioiu, **L. Krieger**, P. A. Dodd, T. Kanzow, C. Licciulli, and C. Schannwell (2018). "Large Ice Loss Variability at Nioghalvfjerdsfjorden Glacier, Northeast-Greenland." In: Nature Communications (Mayer et al., 2018), Appendix C

- Kehrl, L. M., I. R. Joughin, D. E. Shean, D. Floricioiu, and **L. Krieger** (2017). "Seasonal and Interannual Variabilities in Terminus Position, Glacier Velocity, and Surface Elevation at Helheim and Kangerlussuaq Glaciers from 2008 to 2016." In: Journal of Geophysical Research: Earth Surface (Kehrl et al., 2017), Appendix D

Two peer-reviewed conference papers are compiled within this cumulative thesis:

- **Krieger, L.** and D. Floricioiu (2017). "Automatic Glacier Calving Front Delineation on TerraSAR-X and Sentinel-1 SAR Imagery." In: 2017 IEEE International Geoscience and Remote Sensing Symposium (IGARSS) (Krieger and Floricioiu, 2017), Appendix E

- **Krieger, L.** and D. Floricioiu (2019). "Improved Delineation of Individual Outlet Glacier Drainage Basins From Tandem-X Elevations And Sentinel-1 Velocities." In: 2019 IEEE International Geoscience and Remote Sensing Symposium (IGARSS) (Krieger and Floricioiu, 2019), Appendix F

2

FUNDAMENTALS

This chapter provides an overview of glacier and ice sheet characteristics and outlines glacier mass exchange processes in Section 2.1.1. The study area of Northeast Greenland and its major outlet glaciers are introduced in Section 2.1.2 with a description of glacier zones in Section 2.1.3. The concept of glacier mass balance is introduced in Section 2.1.4 and the established remote sensing methods to derive glacier mass balance are presented Section 2.1.5. The limitations and specifics of synthetic aperture radar (SAR) and interferometric SAR (InSAR) for polar regions and ice sheets in particular are discussed in Section 2.2.

2.1 GLACIOLOGY FUNDAMENTALS

The fundamentals with regards to the glaciological background of the contributions include an introduction to the cryosphere as a whole with focus on the ice sheets and the Northeast Greenland study region in particular. The concept of glacier mass balance and the common remote sensing approaches for its derivation are outlined.

2.1.1 *The cryosphere, glaciers and ice sheets*

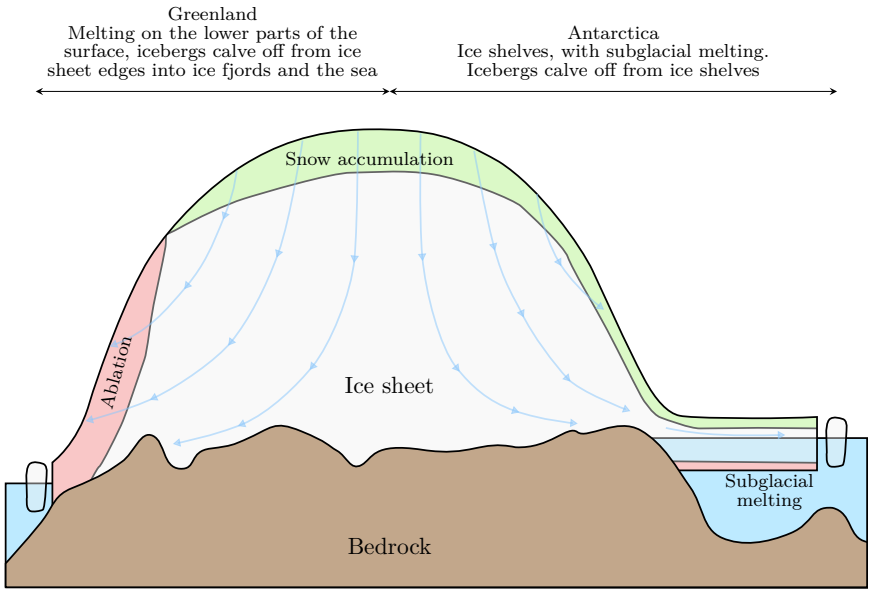

Figure 2.1: The gravity induced ice flow on ice sheets from regions of high accumulation to regions of ablation (Figure adapted from Ahlenius (2007))

The world's glaciated areas consist of accumulated snow that is transformed into firn and glacial ice. Continuous precipitation gradually increases the pressure to underlying layers of accumulated snow and these snow grains are slowly transformed into ice (Paterson, 2016, Chapter 2). The built-up ice then experiences a gravity

induced flow from regions of high accumulation to regions of ablation (Figure 2.1). The glaciated regions of the earth are classified into two ice sheets, Greenland and Antarctica, multiple ice fields (e.g. Patagonian Ice Fields), ice caps and smaller ice bodies like single glaciers. Other components of the cryosphere include terrestrial permafrost, sea ice and seasonal snow cover (Figure 2.2). Apart from the land ice in Greenland, this thesis only deals with one other form of freshwater ice: Ice shelves or ice tongues. Those are floating parts of water terminating glaciers which are still physically connected to the ice sheet and which are providing a buttressing effect to their tributary glaciers (Angelis and Skvarca, 2003; Rott et al., 2002). Large floating ice tongues exist predominantly in Antarctica and few in Greenland and Ellesmere Island.

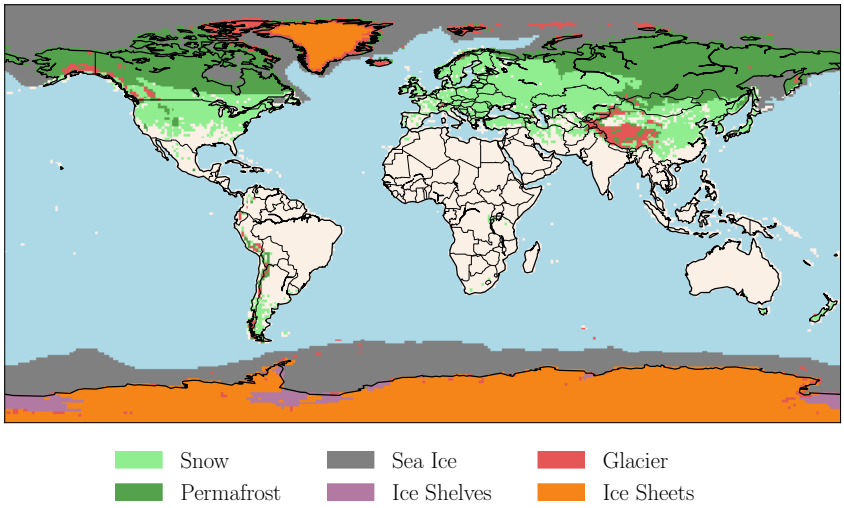

Figure 2.2: The global cryosphere characterised by type. Apart from the land ice in Greenland, this thesis only deals with one other form of ice in the ocean, which are ice shelves. Data from: (Cogley, 2003; Hall and Riggs, 2015)

The mass of the ice sheets far exceeds the mass of other land ice. To aid the understanding of the large ice quantities, their masses are sometimes expressed as sea level equivalent (SLE) representing the resulting rise of the global sea level if all ice would melt completely. All glaciers together hold a SLE of only 0.41 m while the Antarctic Ice Sheet alone holds a sea level potential of 58.3 m and the Greenland Ice Sheet (GrIS) of 7.36 m (Vaughan et al., 2013).

An obvious feature of an ice sheet are its outlet glaciers, that drain ice through peripheral mountains into the ocean. In Greenland, the outlet glaciers mainly drain into long narrow fjords and contrary to Antarctica there are relatively few floating ice tongues and most termini are grounded at the front (Khan et al., 2015; Moon et al., 2012). Through its outlet glaciers the ice sheet is in contact with the ocean which can lead to dynamic changes on the ice sheet caused by environmental forcing at its marine margins (Howat, Joughin, and Scambos, 2007; Joughin et al., 2019; Kehrl et al., 2017; Luckman et al., 2006; Sole et al., 2008).

This work focuses specifically on remote sensing methods for ice sheets and their marine terminating outlet glaciers. These differ in spatial scale to applications on smaller ice bodies and also deal with a different structural composition of ice and firn. Some glacier zones are unique to ice sheets and do not exist on smaller ice

bodies. Only ice sheets are characterised by large flow features like ice streams of converging and diverging glacier flow. Most of the large glaciers on the GrIS are marine terminating and exhibit substantial dynamic ice export due to calving of icebergs. The partitioning of the overall mass loss into surface mass balance and mass loss because of ice dynamics has changed over the last decades. For Greenland, increased ice export through calving has been estimated to account for approx. 50% of the total mass loss (Broeke et al., 2009; Mouginot et al., 2019). Calving therefore plays a more important role than it does for smaller ice bodies.

2.1.2 *Northeast Greenland*

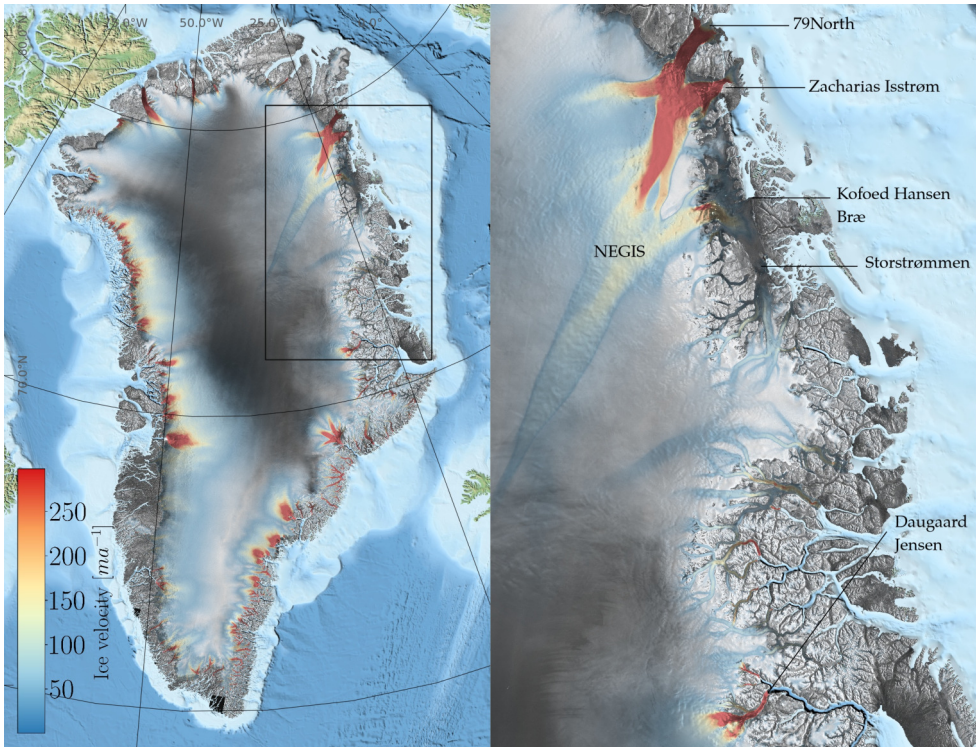

Figure 2.3: The major outlet glaciers in the Northeast Greenland region. The Northeast Greenland Ice Stream (NEGIS) is reaching deep in the interior of the Greenland Ice Sheet. Bathymetry data (GEBCO Compilation Group, 2019), Backscattering amplitude (Joughin, 2015), Ice velocity (Joughin, Smith, and Howat, 2018a).

The Northeast Greenland ice sector is drained in large parts by the NEGIS (Figure 1.1). This large scale flow feature reaches more than 600 km into the ice sheet interior to altitudes above 2900 m (Fahnestock et al., 1993; Joughin, Fahnestock, and Bamber, 2000). The ice stream diverges into the outlet glaciers Nioghalvfjersfjorden (79North), Zachariæ Isstrøm (ZI), Kofoed Hansen Bræ and Storstømmen. Those marine terminating outlet glaciers in particular are broader than the many smaller-sized, fast-moving counterparts in West and Southeast Greenland (Rignot and Mouginot, 2012). NEGIS is the largest ice stream in Greenland and its dynamic behaviour is of interest because it drains substantial parts (approx. 17%) of the GrIS. Its response to a warming climate has been extensively studied but large uncertainties of its mass balance remain (Choi et al., 2017; Mayer et al., 2018; Vallelonga et al., 2014).

79North has a 70 km long ice shelf that is still intact but has thinned by 30% between 1999 and 2014 (Mayer et al., 2018). Multiple other ice tongues in Greenland have recently disintegrated (Hill et al., 2018) and the floating termini at 79North, Petermann and Ryder Glacier are examples of the few remaining ice tongues in Greenland. Near the grounding line the ice velocity of 79North is approx. 1400 m a^{-1} and has shown a minor speed-up of 2% in the last decade (Mouginot et al., 2019). At the terminus, the floating ice tongue is grounded at small islands or ice rises which is thought to provide a stabilising effect (Choi et al., 2017).

The second dominant glacier in the Northeast Greenland region is ZI with a terminus width of approx. 25 km. The fast ice flow of up to 2300 m a^{-1} is subject to strong seasonal fluctuations, which makes it difficult to determine if the glacier front is currently floating or grounded (Mouginot et al., 2017). Previously, ZI terminated in an ice shelf that was stable until 2002 but steadily disintegrated until 2014 when 95% of the ice shelf has been lost (Mouginot et al., 2015). Contrary to 79North, the bed topography of ZI is characterised by a downward sloping bed towards the ice sheet interior (retrograde slope). Because of the possible penetration of warm water under the terminus and subsequent rapid retreat, this is considered an unstable bed configuration leading to high velocity speed-ups (Kehrl et al., 2017).

Other major outlet glaciers in the NE Greenland region include Storstrømmen, which experienced a surge from 1978 to 1984 (Mohr, Reeh, and Madsen, 1998; Reeh, Bøggild, and Oerter, 1994), and the southernmost glacier of the investigated area, Daugaard-Jensen (DJ). With a velocity magnitude of 3500 m a^{-1} close to the terminus it is the fastest flowing outlet glacier in the Northeast Greenland region.

2.1.3 *Glacier zones*

The different glacier zones are a direct result of the mass exchange processes taking place on the ice sheets. The zones feature different snow, firn and ice conditions which are of importance to active remote sensing because they exhibit varying scattering mechanisms. Therefore, the zones are also characterised by different properties concerning the penetration of the electromagnetic signal into ice and snow (Dall et al., 2001).

1. *Dry snow zone* The dry snow zone is located at high elevations on ice sheets where no melting occurs throughout the entire year. Electromagnetic signals penetrate the uppermost snow layers depending on the used wavelength and volume scattering characterises the returned signal.

2. *Percolation zone* Some melting occurs during the summer in this zone and meltwater percolates into the upper snow layers. In the colder snow the meltwater refreezes to larger structures like ice lenses and ice glands. These can act as strong scatterers which changes the backscattering characteristics for electromagnetic signals.

3. *Wet-snow zone* The snow in this zone which has accumulated during the current year is completely warmed above 0 °C at the end of ablation season and the entire year's snow layer is wet. The water content in the snowpack ensures that limited SAR signal penetration occurs during the melt period.

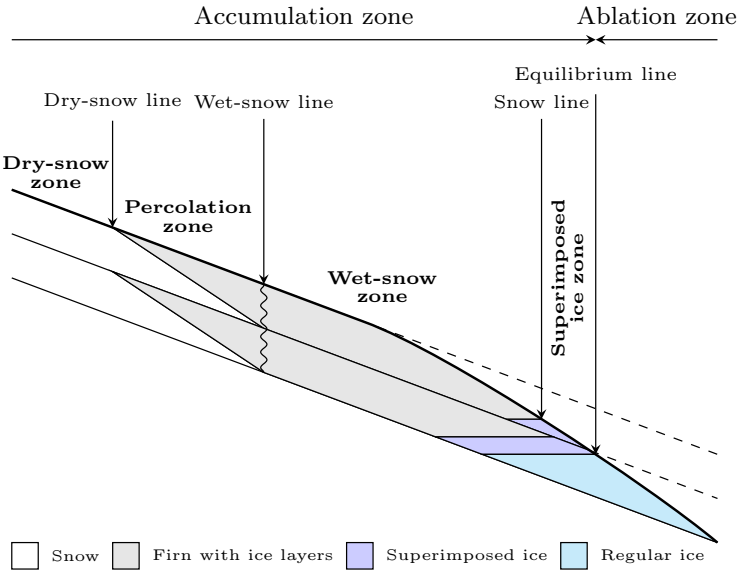

Figure 2.4: The glacier zones based on Benson (1962). The zones exhibit different backscattering characteristics for active electromagnetic sensors. Figure adapted from Paterson (2016).

4. *Superimposed-ice zone* Meltwater refreezes at the lower end of the wet-snow zone until a continuous ice layer is forming the superimposed-ice zone. At its upper limit, the snow line is identifiable on spectroradiometer images and marks the boundary between the two zones (Ryan et al., 2019).

5. *Ablation zone* The ablation zone extends from the equilibrium line down to the lowest elevations of the glacier. Here, the surface mass balance is negative. More melting than precipitation occurs and the glacier is losing mass. Bare ice is visible during most of the season and surface features determine the backscattering characteristics in this zone.

The glacier zones in Greenland were first introduced by Benson (1962) in a field campaign and have been refined by Paterson (2016, Chapter 2.3). Today, the extent of the zones is determined with satellites using passive remote sensing sensors (Nolin and Payne, 2007; Williams, Hall, and Benson, 1991).

On the ice sheets, all glacier zones cover substantial extents of the glaciated area although the dry snow zone is disappearing in Greenland (McGrath et al., 2013; Nghiem et al., 2012). However, on smaller ice bodies not all zones might be present.

2.1.4 *Glacier mass balance*

Each year a glacier is subject to seasonal variations and loses or gains mass depending on environmental conditions. After one hydrological year, the glacier has experienced all seasonal phases. If the glacier is in balance the glacier ice mass is unchanged. The deviation from the previous year's mass is termed the total net mass balance of a glacier. It is usually expressed in $\mathrm{Gt\,a^{-1}}$ and is negative if the glacier is losing mass and positive if enough ice and snow has accumulated to compensate for ice export and melting. All mass gains are termed *accumulation* while all mass losses are combined under the term *ablation*. The dynamic ice export due to *calving* is handled

separately (Figure 2.5). Ablation includes melt, sublimation and evaporation and is balanced by the accumulation processes precipitation, avalanching or refreezing. A mass exchange process that can contribute both positively and negatively to a glacier's mass budget is wind deposition.

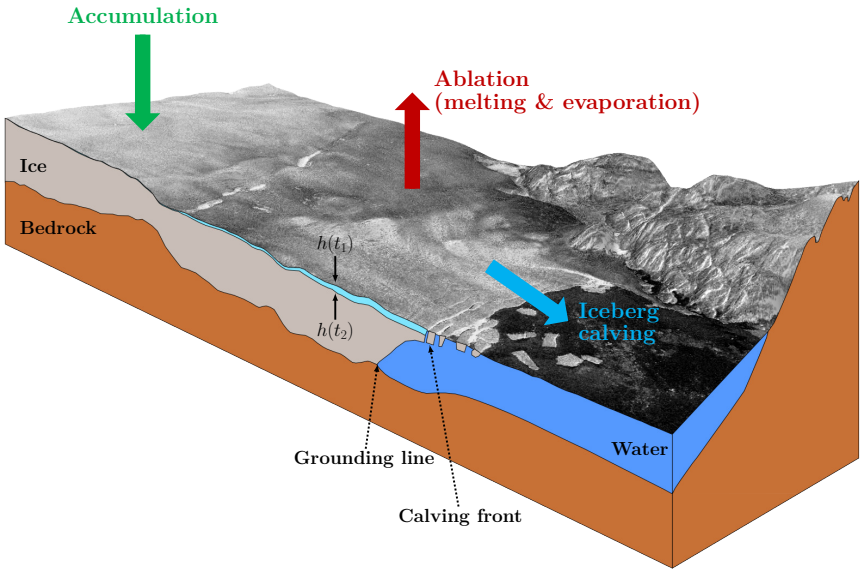

Figure 2.5: The mass balance components relating to mass gains (accumulation) and mass losses (ablation and calving). While the mass budget method estimates these components separately, volumetric methods calculate the lost ice volume (light blue) between two time points by measuring surface elevation change.

The specific mass balance rate of a glacier represents the change of mass per unit area and is denoted as $\dot{b}$. It is given in $\mathrm{kg\,m^{-2}\,a^{-1}}$ and Paterson (2016, Chapter 4.1.1.2) further specifies $\dot{b}_s$ as the mass balance at the ice surface, the basal mass balance $\dot{b}_b$ and the mass balance within the vertical column of ice $\dot{b}_e$ (englacial balance). $\dot{b}_s$ contains processes like melting, runoff and refreezing in the upper ice and firn layers. $\dot{b}_b$ is driven by the geothermal heat flux and frictional heat for fast flowing glaciers. $\dot{b}_e$ contains remaining mass exchange processes like refreezing of meltwater within the ice sheet. Then the rate of total mass change of a glacier with area $\mathcal{A}$ is given by

$$\frac{dM}{dt} = \int_{\mathcal{A}} \left(\dot{b}_s + \dot{b}_e + \dot{b}_b\right) d\mathcal{A} - \dot{B}_c = \int_{\mathcal{A}} \rho \frac{dh}{dt} d\mathcal{A} \tag{2.1}$$

For ice sheets the dominant components are the dynamic ice export lost by calving per unit time $\dot{B}_c$ in $\mathrm{kg\,m^{-2}\,a^{-1}}$ and the surface mass balance (SMB) $\dot{b}_s$. However, instead of partitioning mass changes in the specific mass balance rates and calving, another way to calculate the rate of total mass change is to multiply the surface elevation change rate (SECR) $\frac{dh}{dt}$ by a spatially distributed firn density ρ and integrate over the glacier area.

While the SMB is driven by atmospheric forcing the driving mechanisms for increased ice export and dynamic thinning are more complicated. Previously investigated reasons for increased dynamic ice loss include the retreat from stable front positions at bedrock ridges to an over-deepening in the glacier fjord (Kehrl et al., 2017), ice mélange rigidity (Joughin et al., 2019), the collapse of ice shelves and the

associated loss of its buttressing effect on its tributary glaciers (Angelis and Skvarca, 2003; Rott et al., 2002) and accelerating ice flow due to increased basal lubrication after strong melt events (Shannon et al., 2013). The oceanic warm water forcing at the marine margins can lead to ice shelf collapse or can trigger calving front and grounding line retreat initiating these dynamic changes (Holland et al., 2008; Shepherd, Wingham, and Rignot, 2004). Despite the importance of these dynamic processes, Enderlin et al. (2014) states that the contribution of dynamic mass loss to Greenland's total mass loss decreased from 58% before 2005 to 32% between 2009 and 2012 making melting and subsequent runoff the dominant factor in total mass loss.

2.1.5 *Mass balance estimation*

To measure the mass balance of ice sheets and glaciers there are several established methods. In particular, there are the following three common approaches in remote sensing applications (Alley, Spencer, and Anandakrishnan, 2007; Khan et al., 2015).

MASS-BUDGET METHOD In this approach, known also as input-output method, all sources contributing to mass gain and mass loss are added to form a mass budget. All ablation components are subtracted from the budget while accumulation contributes positively to the mass balance. Mass loss due to calving at the front is calculated separately from the terms related to the ablation on the glacier. This method therefore allows a separation of dynamically induced mass loss $\dot{B}_c$ and mass changes forced by the atmosphere $\dot{b}_s$ (Equation 2.1). The surface mass budget $\dot{b}_s$ includes the accumulation term which is dominated by precipitation but sublimation and refreezing should not be neglected for ice sheets (Paterson, 2016, Chapter 4.2). The ablation components are more diverse and include: surface melting, runoff and basal melting $\dot{b}_b$ (Equation 2.1). All mentioned processes can be retrieved from regional climate models to form the essential SMB (Noël et al., 2016), which is subsequently integrated over the entire observed area $\mathcal{A}$ of the glacier.

The separate calving term $\dot{B}_c$ is describing the dynamic ice loss. The ice export is estimated by calculating the mass flux across a line upstream, close to the glacier grounding line. Depth-averaged ice velocity measurements at this line are multiplied by the ice thickness cross section to retrieve the ice mass flux across the defined gate. To this end, ice surface velocities are retrieved from satellite measurements by SAR interferometry and offset tracking. The required ice thickness can be determined with various methods including ice-penetrating radar (Alley, Spencer, and Anandakrishnan, 2007), seismic bathymetry of the lake/fjord (Mayer et al., 2000) or mass-conservation approaches (Morlighem et al., 2017a).

GRAVIMETRIC METHOD Another way to obtain glacier mass balance is to measure the earth's gravity field and its time variability. The joint NASA/DLR mission Gravity Recovery and Climate Experiment (GRACE) was designed to achieve this goal (Tapley et al., 2004). Operating from March 2002 until October 2017 it has since been superseded by the follow on mission GRACE-Follow-On (GRACE-FO) launched in May 2018. In contrast to other mass balance estimation methods it represents a direct measurement of glacier mass change. Because the measured mass fields are inherently noisy, filtering and spatial integration has to be performed. The final

GRACE mass change solutions are provided by different processing centres from GRACE Level-1 observations (Sakumura, Bettadpur, and Bruinsma, 2014). These have a resolution of several 100 km and are typically distributed on relatively coarse grids of 1° spatial sampling. Moreover, the filtering introduces signal leakage from areas outside of the region of interest depending on the size and location of the investigated area. The main challenge in the gravimetric method for ice sheets is to model all contributing sources of mass change correctly to be able to distinguish between glacial isostatic adjustment (GIA), the tidal loading or other origins of mass change outside the region of interest (Wahr, Molenaar, and Bryan, 1998). Because of these constraints the gravimetric method is not applicable to the individual glacier scale.

VOLUMETRIC METHOD The volumetric method is also called the geodetic method. By measuring the volume change of ice and snow on a glacier the total net mass balance is inferred (Figure 2.5). A straightforward way to quantify changes in ice volume is to measure the ice sheet surface elevation at two time points t_1 and t_2. Integrating the elevation changes spatially over an area $\mathcal{A}$ of the glacier yields the volume change (Equation 2.1). Various sensors are used to retrieve the necessary elevation measurements including radar- and laser altimeters providing time-series of point wise elevation measurements. Other methods like airborne as well as spaceborne optical or SAR data are used to produce digital elevation models (DEMs) for specific time points which are subsequently subtracted to retrieve spatially detailed surface elevation change (SEC).

For the conversion of the volume changes to mass change, the density of the dynamically lost ice volume is usually assumed to be the density of ice equalling 917 kg/m^3 in Greenland (Paterson, 2016, Chapter 2.2.1). Volume change resulting from surface mass balance processes on the other hand has to be converted using modelled firn densities because the lost surface layers have a lower density than glacial ice (Hurkmans et al., 2014; Ligtenberg et al., 2018; McMillan et al., 2014). Mass-unrelated volume changes are also of importance and the measured volume change has to be corrected for these. Examples for such volume changes are GIA, firn compaction (FC) and elastic bed uplift (EBU) (Khan et al., 2014, 2015).

This method is discussed in detail in Chapter 4.

2.2 LIMITATIONS OF SAR AND INSAR IN POLAR REGIONS

SAR is an active sensor that transmits coherent electromagnetic signals which are scattered at the ground and received back by the antenna. The complex signals include phase information that measures the range to the scatterer down to fractions of the used wavelength and the amplitude which carries information about the energy of the backscattered signal. The phase of a single SAR acquisition cannot be utilised on its own. With InSAR however, the phase information of two single- or repeat-pass SAR acquisitions can be exploited to measure differences in signal travel time. Figure 2.6 shows exemplary a backscattering amplitude image and an interferogram of a glacier in Greenland. The phase differences seen in 2.6(b) are dependent on the baseline between the two SAR sensors and in the case of the visualised bistatic single-pass interferogram, the main component contributing to the fringe pattern is the topography.

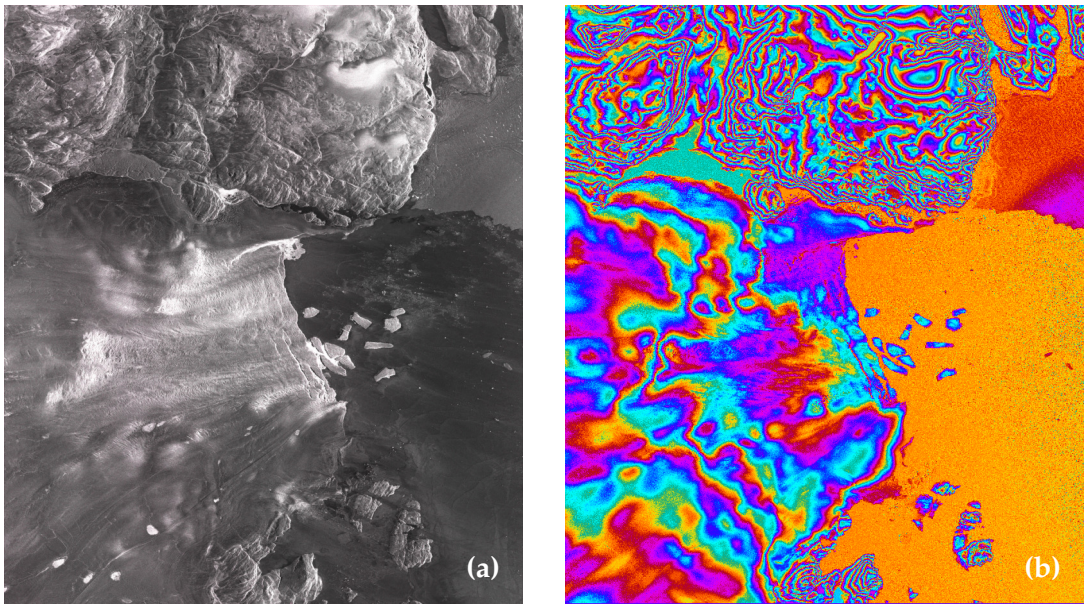

Figure 2.6: (a) TanDEM-X (TDM) backscattering amplitude image and (b) the corresponding single-pass bistatic interferogram of Zachariæ Isstrøm in Northeast Greenland acquired on 2013-12-26.

Spaceborne SAR sensors are a widely used tool in the remote sensing of the ice sheets. As an active sensor, SAR is not dependent on solar illumination and the earth's atmosphere is transparent at the microwave frequencies emitted by radars. Therefore, SAR can reliably image the earth's surface and it is operating independently of cloud cover and light conditions. During the several month long polar night in parts of Greenland and Antarctica, SAR acquisitions provide continuous observations of the glacier surface. The high-resolution phase and amplitude measurements allow to derive glaciological parameters like surface elevation, ice velocity, the grounding line or the calving front. Nevertheless, the physical properties of ice and also the atmospheric conditions at the poles create some challenges and limitations for the use of SAR and InSAR techniques in polar regions and for the observation of ice sheets.

2.2.1 *SAR signal penetration*

The dielectric properties of ice and snow cause a penetration of the electromagnetic SAR signal to a depth depending on the liquid water content of the snow layer as well as the used wavelength (Mätzler, 1987). Greater liquid water content leads to a stronger absorption of the signal which in turn causes a reduction of the penetration length. Moreover, not only the dielectric properties but also the structural properties of the snowpack affect the amount of penetration by controlling the extinction coefficient κ_e of the medium (Stiles and Ulaby, 1981). The penetration length l is the point after which the signal power has attenuated to $\frac{1}{e}$ (37%) of the signal power just beneath the ice surface and therefore the one-way-power penetration depth d_1 can be calculated with the help of the refraction angle θ_v. It is calculated by Snell's law

based on the incidence angle θ_i of the SAR acquisition and the refractive indices of air n_{air} and ice n_{ice} (Dall, 2007).

$$d_1 = l \cos \theta_v \qquad n_{air}\theta_i = n_{ice}\theta_v \tag{2.2}$$

The two-way penetration depth d_2 follows as the depth at which the power of the reflected signal measured at the ice surface reduces to $\frac{1}{e}$.

$$d_2 = \frac{1}{2}d_1 \tag{2.3}$$

There is an important distinction between the penetration depth and the resulting InSAR elevation bias due to the signal penetration. Dall (2007) showed that the two-way penetration depth d_2 is approximately equal to the InSAR elevation bias if d_2 does not exceed 10% of the height of ambiguity (HoA) h_a. Otherwise the elevation bias is smaller than the two-way penetration depth and reaches approximately 25% of h_a for $\frac{d_2}{h_a} \gg 1$.

On the ice sheets there are 3 notable scenarios of signal penetration according to the glacier zones described in 2.1.3. First is the dry snow zone where no substantial melting occurs. It contains fine snow grains and a low liquid water content which is resulting in high penetration depths. The elevation bias due to penetration at TDM X-band compared to ICESat measurements can be >8 m for the interior of the GrIS. A mean elevation bias of 5.4 m was measured for the dry snow zone (Rizzoli et al., 2017a). Second, some melting takes place in the percolation zone. Ice inclusions occur in the snow pack and reduce the two-way penetration depth given in Equation 2.3 (Abdullahi et al., 2018). Depending on the amount of melting dense ice layers may even be present at the previous summer surfaces. These layers act as strong scatterers. Dall et al. (2001) found elevation biases of up to 13 m for airborne C-band SAR over the percolation zone of Geikie ice cap. Lastly, in large parts of the ablation zone there are enough surface features to make surface scattering the dominant scattering mechanism resulting in a negligible penetration depth at X-band.

There exist several approaches to tackle the problem of InSAR elevation bias due to signal penetration. Because of the attenuation of the signal, the backscattering coefficient σ^0 is an indicator of the dielectric properties of the snowpack and can be utilised to identify areas that are subject to signal penetration (Abdel Jaber, 2016). A possible correction approach is to use the interferometric coherence to model penetration depth by assuming a homogeneous snow layer with exponential loss (Weber Hoen and Zebker, 2000). The assumption of a constant signal extinction which results in the exponential loss, cannot account for more complex scattering scenarios and was shown to underestimate InSAR phase centre depths (Dall, Papathanassiou, and Skriver, 2004). Few studies have shown the potential of Polarimetric SAR Interferometry to account for scattering scenarios with additional scattering from the surface (Sharma et al., 2013) or subsurface layers (Fischer, Papathanassiou, and Hajnsek, 2019) but penetration bias retrieval techniques which go beyond the constant extinction assumption are not yet established.

2.2.2 *Temporal decorrelation*

A general limitation using standard repeat-pass InSAR techniques for remote sensing of the ice sheets is the relatively fast temporal decorrelation of the observed ice surface. Precipitation, melting, snow drift and ice flow distortions cause the scatterers within one resolution cell to change in a way that leads to phase instabilities. This in turn leads to a degradation of the phase measurement using InSAR.

The length of the temporal correlation varies over the ice sheet and is dependent on weather conditions and ice flow. Especially the fastest flowing outlet glacier often decorrelate in less than a week for the X- and C-band instruments and a combination of SAR satellite constellations has to be used to shorten the revisit time (Milillo et al., 2016). In the case of distortions because of ice movement a higher resolution sensor also maintains correlation for a longer time period. In Greenland, the revisit time of 11 days of TerraSAR-X (TSX) is sufficient to capture ice velocities with offset tracking techniques for all outlet glaciers, while a 6 day revisit is needed for the lower resolution of Sentinel-1 (Nagler et al., 2015b). More stable surfaces in terms of measured phase can be imaged with longer wavelengths which penetrate tens of meters into the snow and ice layer. A longer temporal correlation can be achieved with high resolution L-band sensors at these lower layers.

In addition to the temporal decorrelation of the ice surface in general, there is also lack of persistent scatterers on glacial ice. This limits the use of state of the art interferometric techniques requiring long temporal baselines. Methods like persistent scatterer interferometry (PSI) are therefore not applicable in the context of ice sheets.

If coherent acquisitions are available, InSAR is however an important tool to measure ice velocities in the ice sheet interior with accuracies of $<2\,\mathrm{m\,a^{-1}}$ (Joughin, Kwok, and Fahnestock, 1998) or to detect the location of the grounding zone (Rignot, Mouginot, and Scheuchl, 2011b).

2.2.3 *Ionospheric phase shift*

The ionosphere is an atmospheric layer which peaks at heights between 300 and 400 km. Its activity is dependent on the incoming solar radiation and strongest activities are therefore found at the equator (Kelley, 2009). At the poles, the earth's magnetic field attracts charged particles leading to auroras and turbulent effects in the ionosphere (Meyer, Nicoll, and Bristow, 2009). The charged particles contained in the ionosphere effect the propagation of radio waves by dispersion and exert a frequency dependent range delay and phase advance of electromagnetic waves depending on the total electron content (TEC) along the travel path (Gomba, 2016). For SAR this effect is of particular importance for longer wavelength C- and L-band systems resulting in range and azimuth blurring. In image pairs used for InSAR or offset tracking, the differential TEC along the synthetic aperture leads to azimuth shifts and an ionospheric phase screen in the interferograms (Gray, Mattar, and Sofko, 2000). For polar remote sensing, this results in so called *azimuth streaking* during ice velocity mapping with SAR (Nagler et al., 2015a).

In RADARSAT C-band data of Greenland, ionospheric conditions have been observed which introduce shifts corresponding to several tens of $\mathrm{m\,a^{-1}}$ of ice velocity (Joughin et al., 2010) while in Antarctica absolute shifts of 1 m have been measured with RADARSAT-1 (Gray, Mattar, and Sofko, 2000). Mouginot, Scheuchl, and Rig-

not (2012) find ionospheric noise for ALOS PALSAR of $\pm 17\,\mathrm{m\,a^{-1}}$ at the poles and $\pm 8\,\mathrm{m\,a^{-1}}$ for the West Antarctic Ice Sheet. At C-band, maximum ionospheric errors reduce to $\pm 6\,\mathrm{m\,a^{-1}}$ for RADARSAT and $\pm 4\,\mathrm{m\,a^{-1}}$ for ENVISAT. Nagler et al. (2015b) report ionospheric errors of $\pm 29\,\mathrm{m\,a^{-1}}$ in their 12-day repeat pass velocity measurements because of the shorter repeat cycle of Sentinel-1 which increases the ice velocity errors induced by the ionosphere. By averaging multiple scenes, this error has been reduced to $\pm 7\,\mathrm{m\,a^{-1}}$.

If time-series of ice velocities are available, one way to reduce ionospheric effects in ice velocity maps is to average measurements within a stack of velocity products or across tracks. For InSAR, a split-spectrum method has been proposed to correct for the ionospheric effects (Gomba et al., 2016). It estimates a ionospheric phase screen resulting from gradients in TEC along the azimuth flight direction which is subsequently removed from the interferograms. The correction is of importance in regions with strong ionospheric activity but also for other ionospheric phenomena at the poles. Nevertheless, small scale perturbations of the ionosphere caused by auroral effects may still remain after the correction.

3 STATE OF THE ART

In the last century, a variety of satellite based remote sensing techniques have opened up new possibilities for ice sheet monitoring (Bindschadler, 1998). The longest active sensor record for ice sheet measurements is provided by radar altimeters which started monitoring the ice sheet topography in the 1970s (Brooks et al., 1978) and have since become more accurate over the rough ice sheet surface with the European Remote Sensing Satellite (ERS) mission (Bamber, 1994). In the visible spectrum, the Landsat mission has produced glaciological results since 1980 (Williams et al., 1982). Later, with the advent of synthetic aperture radar (SAR) missions in the 1990s the acquisitions were used to produce first backscattering mosaics of the ice sheets (Bindschadler, Jezek, and Crawford, 1987) and the earliest large-scale velocity maps (Fahnestock et al., 1993). Further developed methods for SAR interferometry allowed more detailed ice flow measurements of glaciers (Joughin, Kwok, and Fahnestock, 1998) and the delineation of glacier grounding lines (Goldstein et al., 1993). The latest fundamentally different technique to measure ice sheet parameters from space was the Gravity Recovery and Climate Experiment (GRACE) launched in 2002 which produces direct measurements of ice sheet mass change (Velicogna and Wahr, 2005).

The present chapter outlines state of the art methods to derive glaciological parameters with satellite remote sensing techniques. Special focus is put on research that observes the earth's ice sheets with SAR-based techniques. Some methods are similar to those used for remote sensing of smaller ice bodies. Others however are unique to ice sheets because of the difference in scale and physical properties. The chapter has been ordered by the glaciological parameters of interest, describing previously published techniques to derive the glacier extent in Section 3.1, the ice velocity in Section 3.2, the surface elevation change in Section 3.3 and finally the glacier mass balance in Section 3.4.

3.1 GLACIER EXTENT

The spatial extent of single glaciers, entire regions or the complete ice sheet has to be defined in order to partition mass balance measurements to the desired level. A widely used data set defining the Greenland Ice Sheet (GrIS) extent is published within the Greenland Ice Mapping Project (GIMP) (Howat, Negrete, and Smith, 2014). It includes classifications for the surface types: grounded ice, floating ice, non-glaciated area and ocean. The classification was performed manually on panchromatic and pan-sharpened multispectral image mosaics of Landsat 7 Enhanced Thematic Mapper (ETM+). The GIMP ice mask has a resolution of 15 m which adequately defines the land-ice interface for most applications. The ice-ocean interface represented by the calving front or grounding line/zone is subject to stronger fluctuations and needs to be detected separately for the desired time interval. Also the drainage divide that separates the individual glacier catchments on the ice sheet is not included in the GIMP ice mask and needs to be retrieved from different sources.

3.1.1 *Drainage basins*

The *drainage basin* of a glacier specifies the entire area of ice that flows towards a single glacier terminus. The term *glacier catchment* is often used interchangeably and also references the glaciated area that is attributed to a single glacier. The terms *drainage sector* and *drainage region* apply to larger areas of ice that contain multiple glaciers. The exact difference is loosely defined, but drainage sectors contain several glaciers that belong to a common flow system (e.g. Northeast Greenland Ice Stream (NEGIS) sector, Figure 1.1) while drainage regions are parts of the ice sheet that are separated by major ice divides that are clearly identifiable even in low resolution digital elevation models (DEMs). One example of a major drainage region which is subject to this thesis is Northeast Greenland.

The delineations of individual drainage basins and glacier outlines are essential to produce statistics for glaciological parameters for single glaciers. They allow the integration of measurements across individual basins for which previous research has shown that glacier reactions vary considerably depending on local glacier geometry or environmental forcing (Felikson et al., 2017; Motyka et al., 2017; Mouginot et al., 2019; Rignot et al., 2016). Therefore, a finer separation into individual glacier drainage basins is desirable.

For nearly all mountain glaciers and glaciers on ice caps and ice fields the catchments are delineated semi-automatically and published in the Randolph Glacier Inventory (RGI) that is part of the Global Land Ice Measurements from Space (GLIMS) glacier database (GLIMS and NSIDC, 2005, updated 2018; RGI Consortium, 2017). For ice sheets however, these data are not available.

Until now the ice sheets' drainage sectors have been mostly separated along the major ice divides. Due to the gentle slopes for large parts of the ice sheets, they have only been processed at coarse resolutions, sometimes with additional modelled data (Hardy, Bamber, and Orford, 2000; Lewis and Smith, 2009). A widely used dataset for drainage sectors has been published by the NASA Goddard Space Flight Center (Zwally et al., 2012, Figure 4.2). It utilises data from the Ice, Cloud and land Elevation Satellite (ICESat) Geoscience Laser Altimeter System (GLAS) and is available for both Greenland and Antarctica. Many ice sheet wide campaigns report mass balance estimates according to this delineation including the ESA/NASA Ice sheet Mass Balance Inter-comparison Exercise (IMBIE) (Shepherd et al., 2012). The second assessment IMBIE-2 (Shepherd et al., 2018) included another published dataset of drainage sectors which was made available by Rignot and Mouginot (2012) and relies on an ERS/ICESat DEM in the interior of the ice sheet with additional velocity information near the coast. While these sources provide excellent basin information for mass balance investigations on a large scale, geodetic mass balance estimates from high resolution datasets with narrow swath widths such as from the TanDEM-X (TDM), Pléiades and WorldView satellite missions (Gleyzes, Perret, and Kubik, 2012; Krieger et al., 2007; Shean et al., 2016) would benefit from individual glacier basins that allow a more focused data collection.

Previously, Mouginot et al. (2015) delineated basins for Nioghalvfjersfjorden (79North) and Zachariæ Isstrøm (ZI) by combining ice velocity and DEM information and Mouginot et al. (2019) applied a similar methodology to delineate the entire GrIS into 260 individual drainage basins. Other authors report findings based on self-assessed drainage basins in Greenland that were derived from watershed analysis assuming ice flow in the direction of the steepest surface slope (Felikson et

al., 2017; Marzeion, Jarosch, and Hofer, 2012). However, the description of a detailed and fully traceable methodology for deriving basin inventories of individual outlet glaciers was still missing and is part of the contributions of this thesis (Appendix A).

3.1.2 *Calving front*

The location of the calving front at water terminating glaciers marks the seaward extent of the glaciated area. Here, the glacial ice breaks off into the ocean and is no longer physically connected to the ice sheet. Especially for tidewater glaciers, the calving front is subject to strong fluctuations, both seasonally and long term (Mouginot et al., 2015). Depending on the bed topography, the front can migrate on and off stable frontal positions, where the glacier is grounded below sea level (Joughin et al., 2008; Kehrl et al., 2017). A retreat from such a stable position into an over-deepening of the fjord can lead to a detachment of the glacier from the bed followed by rapid retreat (Schoof, 2007). Therefore, changes in the calving front position are seen as early indicators for a glaciers' dynamic behaviour (Moon and Joughin, 2008).

The calving front has long been delineated on satellite imagery (Dwyer, 1995; Moon, Joughin, and Smith, 2015; Schild and Hamilton, 2013), however most research still digitises the line by hand on optical or SAR images. A reason for this is the difficult algorithmic detection of the frontal line close to the crevassed glacier termini where the ocean is often covered with ice mélange (Baumhoer et al., 2018). In the frame of this thesis, a method is proposed to delineate the calving front on SAR imagery based on a Canny edge detection and path optimization leading to promising results for some glacier conditions (Appendix E) (Krieger and Floricioiu, 2017). Mohajerani et al. (2019) introduced an approach that relies on convolutional neural networks to detect better edge candidates for the frontal line on Landsat images but still applies an energy minimisation that is prone to identify erroneous fronts in difficult conditions. These include large icebergs located close to the front, a heavily crevassed glacier terminus or thick ice mélange present in the fjord. All of which make it more difficult to identify the actual calving front on either optical or SAR images. To tackle the problem of spurious edge detections, Baumhoer et al. (2019) applied a modified U-Net to perform image segmentation on dual-pol Sentinel-1 amplitude images in order to identify ice shelf fronts in Antarctica. Also for ice shelves in Antarctica, Wuite et al. (2019) developed an automatic edge detection technique on DEMs from CryoSat-2 (CS-2) swath processing which is delineating the steep calving face. Note that the latter two techniques target ice shelves exclusively. These are larger and have a different calving behaviour than the smaller outlet glaciers for example in Greenland. Therefore, the methods are not directly applicable in such cases and the calving front delineation remains a problem exactly for the dynamic, fast flowing outlet glaciers characterised by high retreat rates and large ice export.

With sensors other than SAR, Seale et al. (2011) developed an automatic approach to detect the calving front from Moderate Resolution Imaging Spectroradiometer (MODIS) data for outlet glaciers in East Greenland utilising a Soebel filter for edge detection. Liu and Jezek (2004) published a method to map ice sheet margins from ERS-1 data and Satellite Pour l'Observation de la Terre (SPOT) imagery. Both of which are not applicable to map high resolution calving fronts across the entire

terminus width of fast flowing outlet glaciers as they also suffer from spurious edge detections crevasses and icebergs.

3.1.3 *Grounding line*

At marine- and the rare occasion of lake-terminating glaciers, the grounding line is located where the glacier ice detaches from the bed and begins to float (Figure 3.1). Grounding lines only exist for glaciers which developed floating ice tongues or that feed larger ice shelves. In Antarctica, which is surrounded by ice shelves, the grounding line defines the margins of the continent. The location of the grounding line coincides with the calving front for glaciers that remain grounded at the front. Since it marks the seaward extent of glacier volume changes that contribute to sea level rise, the grounding line is an important parameter for mass balance estimates. It also represents the gate across which ice export to the ocean is calculated. Moreover, grounding line migration is directly coupled to glacier dynamics and instabilities because the grounding line can migrate on and off stable positions at so called pinning points at high rises in the bed elevation (Rignot et al., 2014; Schoof, 2007).

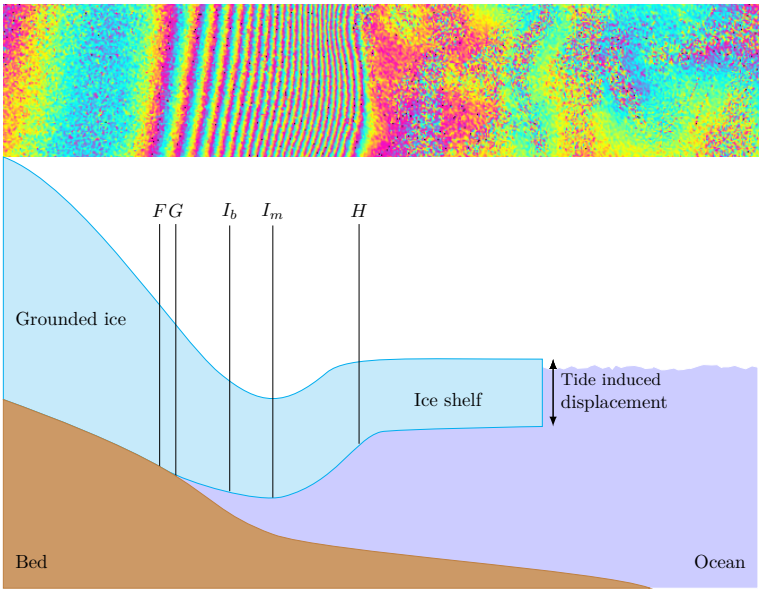

Figure 3.1: The grounding zone of a glacier lies between the most landward F and most seaward point H on which the floating ice tongue experiences flexure because of the vertical displacement induced by the tidal motion. The actual grounding line G where the ice starts to lift of the bed is located close to F which is considered a good proxy to detect G. I_b is the most landward break in slope in the grounding zone while I_m marks a local minimal surface elevation. Displayed above is a typical fringe belt in a differential interferometric SAR (InSAR) (DInSAR) interferogram which is the result of different ice shelf flexures induced by different tide levels. (Figure adapted from Brunt et al. (2010) and Rignot, Mouginot, and Scheuchl (2011b))

Due to the fact that there is no obvious surface feature to separate grounded from floating ice, different proxies can be defined with the term *grounding line*. They result when methodologies sensitive to various topographic or dynamic features are applied to different datasets to obtain the grounding line. The upper limit of

tidal flexure (F in Figure 3.1) can be mapped with conventional InSAR or differential interferograms (DInSAR) by exploiting the vertical displacement of the ice shelf induced by the ocean tides. Given the interferometric phase contributions

$$\phi_{int} = \phi_{vel} + \phi_{tidal} + \phi_{dem} + \phi_{atmo} + \phi_{noise} \tag{3.1}$$

two independent interferograms with different tide levels are differenced in the DInSAR technique. Assuming stable phase contributions of horizontal ice velocity ϕ_{vel}, glacier surface elevation ϕ_{dem} and atmosphere ϕ_{atmo} in both interferograms, the only phase difference component is resulting from the displacement of the ice shelf due to the ocean tides ϕ_{tidal}. A dense fringe belt can be retrieved in the double difference interferogram at the grounding zone of the observed glacier in case the interferometric noise contributions ϕ_{noise} are small. The landward extent of this belt marks the hinge line and is delineated as the grounding line in the double difference interferogram (F in Figure 3.1). For details of how to separate the interferometric phase contributions of glacier topography, ice motion along the radar line of sight and the vertical displacement due to ocean tides the reader is referred to Rignot (1996).

A problem of the DInSAR method is the fast decorrelation of the interferometric phase between the SAR overflights because of the changing natural conditions at the ice surface and fast ice flow at many grounding line locations. This can be overcome by increasing the temporal resolution of the repeat pass SAR acquisitions or by increasing the wavelength of the SAR signal. At fast flowing glaciers like the Thwaites Glacier in Antarctica ($> 2.5\,\mathrm{km\,a^{-1}}$), the COSMO-SkyMed constellation was utilised to reduce the temporal baseline between interferograms to 1 day which limits the impact of temporal decorrelation (Milillo et al., 2019).

During two mission phases specifically designed for ice sheet monitoring, ERS-1 was put in a 3-day repeat cycle in 1991 and 1993 (Goldstein et al., 1993). Additionally, a tandem phase with a 1-day repeat pass configuration was carried out together with ERS-2 in 1995 which was valuable to generate coherent interferograms over the tidal cycle of many Antarctic ice shelves and Greenland outlet glaciers with floating ice tongues. Since 1992 the grounding zone has been delineated with a multitude of SAR sensors and grounding lines in Antarctica have been extensively mapped with the DInSAR technique within the MEaSUREs project (Rignot, Mouginot, and Scheuchl, 2011b). With the launch of the Sentinel-1 constellation in 2014 and 2016 the grounding line is continuously monitored by European Space Agency (ESA)'s Climate Change Initiative (CCI). Still, approx. 20% of the Antarctic grounding line lies at latitudes higher than 78°S (within Sentinel-1's polar data gap) and have to be derived from additional acquisitions of sensors with left-looking capability like TerraSAR-X (TSX), COSMO-SkyMed or RADARSAT.

Apart from DInSAR there are also other remote sensing techniques which are utilised to detect features in the grounding zone. Scambos et al. (2007) applied photoclinometry on MODIS images for the entire Antarctic continent to detect the break in slope (I_b in Figure 3.1). Because the break in slope is at a different position than the hinge line, MODIS and DInSAR grounding lines are not directly comparable. Bindschadler et al. (2011) mapped two ice-dynamic features: the seaward boundary of surface morphology associated with grounded ice (I_b in Figure 3.1) and the landward boundary of freely floating ice shelves or hydrostatic equilibrium line (H in Figure

3.1). With a similar method, Brunt et al. (2010) mapped the grounding zone of the Ross Ice Shelf, Antarctica based on ICESat laser altimetry and Dawson and Bamber (2017) showed that grounding lines from CS-2 radar altimetry are in good agreement (σ: 1.1 km and 1.0 km) with the DInSAR and ICESat grounding lines.

3.1.4 *Calving front and grounding line migration*

Section 3.1.2 and 3.1.3 highlight that changes in the position of the calving front and grounding line affect ice dynamics. Their spatial variation is an immediate and sensitive response to environmental perturbation (Seale et al., 2011). In order to express the changes quantitatively, their migration is usually reported in statistics of retreat and advance. A straightforward way is to report the advance/retreat distance along the central flowline of a glacier (Joughin et al., 2019). Average retreat μ_r can be calculated by the box method (Howat et al., 2010; Moon and Joughin, 2008), which measures the area difference A_{t_1,t_2} between two fronts at time t_1 and t_2 and divides by the average front length. $\mid l_1 \mid$ and $\mid l_2 \mid$ denote the respective lengths of the calving fronts.

$$\mu_r = \frac{A_{t_1,t_2}}{\frac{|l_1|+|l_2|}{2}} \tag{3.2}$$

As these methods do not provide a way to calculate the variation in frontal change across the width of the glacier, Heo, Kim, and Kim (2009) introduced an approach growing a buffer around a reference line. The histogram of overlap percentages to the second line is reported for various buffer sizes resulting in a discrete probability density function (PDF) for the frontal retreat/advance assuming migration along the shortest distance between the two lines. More complicated methods have been proposed which infer the migration direction from the fjord geometry (Lea, Mair, and Rea, 2014). If ice velocities are available, flowlines can be used directly to track advance/retreat along the ice flow direction.

Calving front locations for outlet glaciers in Greenland have been extensively observed and are published in many studies as additional means for interpretation of glaciological processes (Howat et al., 2005; Joughin et al., 2019; Kehrl et al., 2017; Moon and Joughin, 2008). Between 2000 and 2010 91% of glaciers in Greenland have retreated with an average retreat rate of $110\,\mathrm{m\,a^{-1}}$ (Howat et al., 2010).

With the repeated observation strategies of current SAR sensors and the historic acquisitions by ERS, grounding line migration can be observed over time. Contrary to calving fronts, efforts have been restricted locally to regions of interest because of the large data requirement. At Peterman Glacier in Greenland, Hogg et al. (2016) observed grounding line migration from 1992 to 2011. Within the Antarctic Ice Sheet (AIS) CCI project widespread grounding line retreat was detected at the Getz Ice Shelf (Figure 3.2).

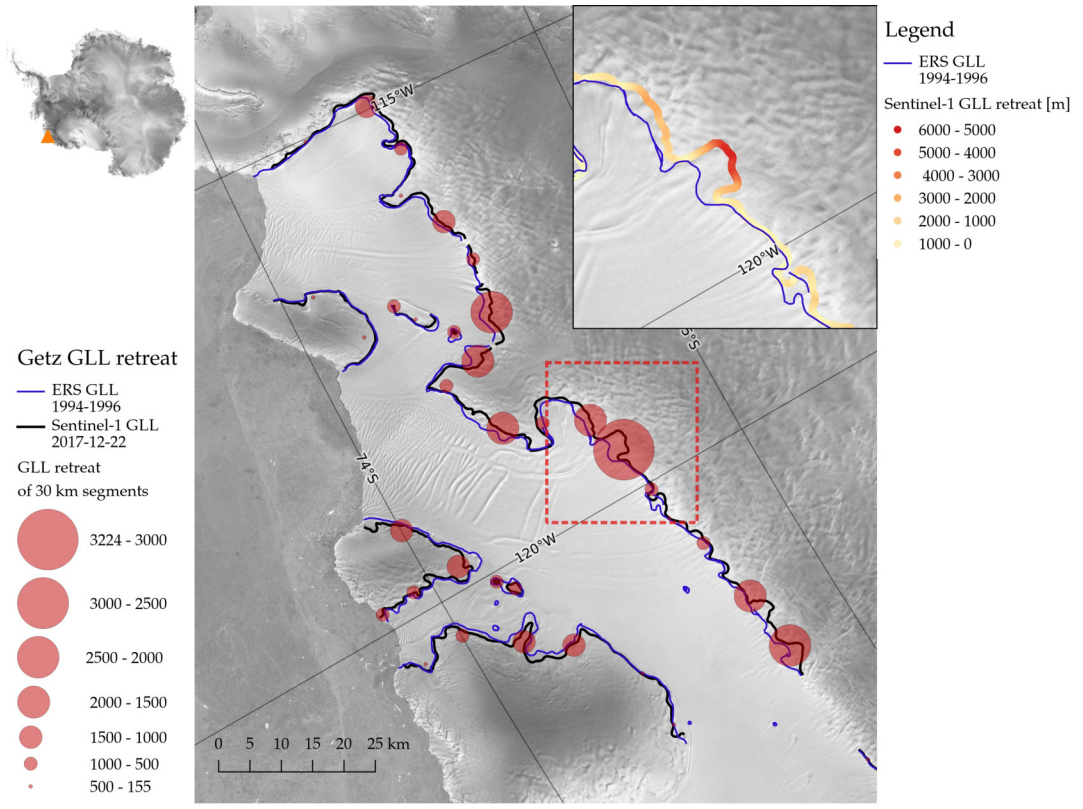

Figure 3.2: Widespread grounding line retreat detected in interferograms from the ERS mission (1994-1996) and from a DInSAR Sentinel-1 triplet (2017-12-16, 2017-12-22, 2017-12-28). Retreat was calculated as the shortest distance between points on the two grounding lines (Heo, Kim, and Kim, 2009).

3.2 ICE VELOCITY

The ice velocity is a key parameter in many glaciological applications involving mass transport. In the mass-budget method specifically, it is needed to calculate the dynamic ice export across a flux gate for estimating glacier mass balance (Section 2.1.5). Ice velocity fields can be derived with SAR and InSAR but also using optical image pairs. A good review of the main spaceborne ice velocity measurement techniques can be found in Dirscherl et al. (2020) and is elaborated on in the following.

Measuring ice velocity with optical techniques relies on the persistence of glacier surface features. Historically, individual visible features like crevasses were tracked manually on satellite images (Lucchitta and Ferguson, 1986) but with the advances in digital image processing the signature of entire image patches can be compared in successive images. There are two methods to perform patch based image matching that have been applied to detect ice motion. The commonly used technique to match intensity values in image pairs is normalised cross-correlation (Lewis, 1995), which identifies the peak of the correlation function between overlapping image patches in the spatial or frequency domain. The method was first applied to ice stream movement in West Antarctica on Landsat images by Scambos et al. (1992). As an alternative to normalised cross-correlation, least-squares matching has also been applied (Debella-Gilo and Kääb, 2012).

The same techniques as for optical image matching can be directly applied to SAR images. Here the term *offset tracking* is more commonly used. It can be performed in the radar coordinate system or on georeferenced data. Because geocoding errors manifest themselves as erroneous velocity measurements during image matching, it is preferable to perform offset tracking in the SAR domain if acquisitions with the same orbit parameters are available. The displacements of the image patches are then tracked in range and azimuth direction and the resulting velocity vectors are projected on a supplied DEM. Normalised cross-correlation can be performed on amplitude or intensity images identifying visible surface features in the same way as in optical image matching (*feature tracking*). Additionally, SAR scenes are characterised by the presence of speckle which can be exploited for offset tracking. Coherence is required to be able to identify stable speckle patterns between image patches but *speckle tracking* is advantageous to measure displacements in smooth glacier areas where no distinct surface features are available. Speckle tracking can be performed directly on the detected amplitude image or on the complex image data. The accuracy of speckle tracking is discussed by Bamler and Eineder (2005). A good overview of SAR-based offset tracking techniques is found in Strozzi et al. (2002).

Apart from offset tracking methods, ice velocity can also be measured by InSAR (Goldstein et al., 1993). As repeat pass interferometry is only sensitive to surface displacements along the line of sight (LOS), the ice velocity vector has to be projected on a DEM, where a surface parallel flow in the direction of the steepest slope is assumed. Joughin, Kwok, and Fahnestock (1998) proposed an InSAR method to derive 2D velocity fields and applied it to Ryder Glacier in Greenland. Still a complete 3-dimensional velocity field that includes submergence/emergence velocities can only be produced with at least 3 interferograms with 3 sufficiently different geometries (Wright, Parsons, and Lu, 2004). Ideally these interferograms are supplied by sensors with right- and left-looking capabilities. A three-dimensional solution for glacial ice movement has been carried out by Gray (2011) using RADARSAT data from 4 different geometries over Ellesmere Island in Canada. Strain and rotation of Darwin Glacier in Antarctica has been measured in 3 interferograms of various combinations of ascending, descending and left or right looking geometries (Parizzi and Abdel Jaber, 2018).

The disadvantage of conventional InSAR which measures displacements only in the direction of the LOS can be overcome by employing multiple-aperture InSAR (MAI) (Bechor and Zebker, 2006; Jung, Yun, and Jo, 2015). In this technique, a forward- and a backward-looking interferogram are formed within the same synthetic aperture in order to separate displacements in the azimuth direction and solve for a 2D velocity field. The technique was first applied to track ice movement by Gourmelen et al. (2011). Still, over many of the fast-flowing and therefore fast-decorrelating glacier termini, SAR offset tracking remains the main source for ice velocity measurements.

The first ice sheet wide velocity mosaic has been produced from ERS data by Fahnestock et al. (1993). Since then, velocity fields have been published from a multitude of sensors, including SAR sensors (ERS, Advanced Synthetic Aperture Radar (ASAR), RADARSAT, TSX, Sentinel-1) and optical sensors (Landsat, SPOT, Advanced Spaceborne Thermal Emission and Reflection Radiometer (ASTER)) with applications on ice sheets, smaller ice bodies and individual mountain glaciers (Berthier et al., 2005; Kääb, 2002; Rignot, 2008; Rott, Rack, and Nagler, 2007). Repeated mappings of the ice sheets allowed for the first time to observe ice flow variability of outlet glaciers in Greenland over several years (Joughin et al., 2010; Rignot and

Kanagaratnam, 2006). Moreover, some individual outlet glaciers (e.g. Jakobshavn Isbræ and Helheim glacier) have been observed with special focus (Joughin et al., 2012, 2014). Whereas in 2008-2009 dedicated satellite campaigns were necessary to acquire complete velocity fields (Rignot, Mouginot, and Scheuchl, 2011a; Rignot and Mouginot, 2012), today Sentinel-1 allows a constant monitoring of the ice velocity in Greenland and Antarctica which is necessary to produce dense, seasonal time-series of velocity measurements (Lemos et al., 2018; Nagler et al., 2015b). Still, the longest time-series for ice velocities is provided by the Landsat satellites covering all years scince 1972 (Rosenau, Scheinert, and Dietrich, 2015). Joughin, Smith, and Howat (2018a) delivered a highly accurate velocity map with errors of approx. $2\,\mathrm{m\,a^{-1}}$ by combining InSAR and speckle tracked ice velocities providing a reference of ice flow in Greenland for the past 20 years. As ice sheet wide flow mosaics are now operationally produced, and deliver consistent measurements with estimated errors (Mouginot et al., 2017), special attention is put on improving the velocity estimates and flow direction errors. Therefore, Mouginot, Rignot, and Scheuchl (2019) published a phase-based velocity map that reduces the error in flow direction to 5° over 80% of Antarctica. Another important task is to acquire higher resolution velocity maps that are able to resolve processes at the glacier shear margins (Jezek et al., 2009). Currently this is only possible with the higher-resolution velocity fields (approx. 50 m) of TSX.

3.3 SURFACE ELEVATION CHANGE

Another key parameter regularly observed for glaciers and ice sheets is the surface elevation change (SEC) which is necessary to calculate glacier volume change. Generally all sensors measuring surface elevation can be utilised to derive SEC over ice covered terrain. They can be broadly separated into two categories. First are altimeters which repeatedly sample pointwise elevation measurements throughout the year along the satellite ground tracks. With repeat altimetry analysis (RAA), a surface elevation change trend is fitted to the time-series of surface elevation measurements at the crossover locations of these tracks. As this is performed for the entire observation epoch the seasonal variation in surface elevation over ice has to be taken into account. Second are sensors capable to generate DEMs which are differenced from each other to generate spatially detailed maps of SEC. Here it is recommended that the DEMs are acquired such as to include full glaciological years. Otherwise a seasonal correction of the elevation change has to be considered.

Radar-altimeters have long been essential tools in earth observation with continuous missions since ERS-1 (Wingham et al., 1998) and even earlier SEASAT acquisitions from 1978 (Zwally et al., 1983). With this long time-series, SEC trends have been estimated by many independent groups (Helm, Humbert, and Miller, 2014; Pritchard et al., 2012; Schröder et al., 2019; Shepherd and Wingham, 2007; Shepherd et al., 2012). A currently operating radar altimeter mission that was specifically designed for cryospheric applications is CS-2. The Synthetic Aperture Interferometric Radar Altimeter (SIRAL) instrument on board of CS-2 features measurement modes exploiting the Doppler shift in azimuth direction similar to SAR. In regions with sufficiently large surface slopes, the 2 antennas estimate the echo return direction with across track interferometry (Wingham et al., 2006). With proper retracking (Martin et al.,

1983) the inherent penetration of the CS-2 Ku-band signal can be kept to a slight bias of 0.2 ± 0.2 m (Helm, Humbert, and Miller, 2014; Schröder et al., 2017).

Laser-altimetry represents another technique that has been used both on airborne platforms like the IceBridge Airborne Topographic Mapper (ATM) (Kurtz et al., 2013) or on spaceborne missions ICESat (Schutz et al., 2005) and the recently launched follow on ICESat-2 (Abdalati et al., 2010). Contrary to radar-altimeters the laser signal reflection originates directly at the ice surface and no penetration occurs.

SEC measurements from DEM-based methods are generated by acquiring temporally separated DEMs which are subsequently differenced. The method can be applied to single DEMs from different sources (e.g. cartographic maps from aerial photography and spaceborne acquisitions). These can have temporal separations of multiple decades but for shorter time-spans repeated acquisitions from the same sensor are commonly used to avoid differences in wavelength or look angle. Using the commercial WorldView satellite constellation, Shean et al. (2016) described operational procedures to generate very high resolution (VHR) DEMs that allow subsequent DEM differencing of repeated acquisitions. Pléiades as well as SPOT provide two other optical stereo DEM alternatives to produce SEC for cryospheric applications (Berthier et al., 2014; Dussaillant, Berthier, and Brun, 2018). Stereo-DEMs have also been generated from ASTER which revealed ice volume loss for the Southern (Willis et al., 2012) and Northern Patagonian Ice Field (Dussaillant, Berthier, and Brun, 2018). Rolstad, Haug, and Denby (2009) developed the theory for SEC error assessment carried out over glaciated regions which is applicable to DEMs originating from various sensors.

Focusing on SAR-based DEM differencing, TDM is the only currently operating spaceborne sensor which is able to generate DEMs from bistatic InSAR with global coverage. In the past, the Shuttle Radar Topography Mission (SRTM) mission provided additional coverage for regions between 60°N and 54°S. In order to generate volumetric measurements from these sensors, two DEMs are produced from repeating bistatic acquisitions of the same region. After a vertical co-registration to a common reference, all vertical biases between the DEMs over stable terrain are removed. The DEMs are finally differenced to reveal spatially distributed SEC (Abdel Jaber, 2016; Abdel Jaber et al., 2019; Malz et al., 2018; Milillo et al., 2019; Rott et al., 2018). For the application on ice sheets this method is discussed in detail in Chapter 4.

In Greenland, the focus of DEM differencing has been put on the termini of large, fast changing outlet glaciers. At Helheim-Gletscher (HG) and Kangerlussuaq, SEC from TDM, Worldview-1/2/3, GeoEye-1 and SPOT 5 stereoscopic survey of Polar Ice: Reference Images and Topographies (SPIRIT) (Korona et al., 2009) has been analysed together with ice velocity, height above floatation, iceberg production or sea ice fraction (Kehrl et al., 2017). On Jakobshavn Isbræ (JI) Joughin et al. (2019) have linked occurrences of rigid ice mélange in front of the terminus during winter to a decrease in SEC, glacier slowdown and increased terminus stability during the following summer. SEC from a total of 84 DEMs spanning the period from 2010 to 2019 has contributed to identify a driver for speed-up and dynamic thinning at the ice-ocean interface. Moreover, SEC from DEM differencing was used to map changes of the Antarctic grounding line at Thwaites Glacier by calculating the height above floatation and identifying a sub-glacial cavity. The cavity facilitates the penetration of warm ocean water under the glacier and leads to increased sub-glacial melting and grounding line retreat (Milillo et al., 2019). However, because of the sparse data

availability of timely, high resolution DEM acquisitions, it has been challenging to cover entire glacier catchments of larger ice sheet outlet glaciers in Greenland with timely, spatially distributed surface elevation measurements. This is why SEC over the termini of large outlet glaciers has been predominantly used to identify causes of dynamic thinning and has not yet contributed to volumetric mass balance estimates of such glaciers. In Chapter 4 an approach is presented that allows using a limited number of high-resolution InSAR DEMs in the context of calculating the geodetic mass balance of individual ice sheet outlet glaciers.

3.3.1 *Signal penetration into ice and snow*

As discussed in Section 2.2.1, the SAR signal penetration into ice and snow plays an important role for the interpretation of InSAR DEMs (Rignot, Echelmeyer, and Krabill, 2001). Specifically, the two way penetration depth offsets the real ice surface from the detected InSAR phase centres on temperate and subpolar glaciers. One solution is therefore to acquire data in summer when it can be assumed that the smooth glaciated surfaces are wet and therefore no penetration occurs (Dall et al., 2001). Because the penetrating signal is attenuated through volume decorrelation or liquid water content, Abdel Jaber et al. (2019) uses the σ^0 backscattering as a proxy to define areas on temperate glaciers where signal penetration likely occurred and might affect the derived SEC. With the same lossy signal assumption, there have been efforts to estimate penetration depth from polarimetric InSAR (PolInSAR), with the help of the polarimetric coherence (Fischer, Papathanassiou, and Hajnsek, 2019; Sharma et al., 2013). These studies show a potential of correcting the signal penetration bias in InSAR derived DEMs but they have been restricted to limited study regions and have not been performed at the ice sheet wide scale. Until now a correction of the signal penetration bias is not a standard procedure during InSAR DEM generation. The penetration bias is also dependent on the observed glacier zone. While over the heavily crevassed glacier termini and in most of the ablation zone surface scattering mechanisms can be expected, SAR tomography transects in the percolation zone confirm a clear layering and strong backscattering at the previous summer surface (Fischer et al., 2017).

3.4 MASS BALANCE

The state of the art retrieval of the glaciological parameters presented in the previous sections provides the basis for ice sheet mass balance estimation as outlined in Section 2.1.5. For the volumetric mass balance method the main input is SEC, whereas ice velocities are used in the mass-budget method. The measurements are aggregated over the glacier extent to form the total net mass balance of an individual glacier or ice sheet sector. These mass balance records serve as input for sea level rise projections and climate analysis (Stocker et al., 2013).

Many studies of ice sheet wide mass balance have been performed in Greenland and a review of these can be found in Khan et al. (2015). Figure 3.3 visualises a time-series of the results derived with various sensors in the respective studies and highlights the mass loss trend of Greenland since the 1990s. Large uncertainties (3–65 $\mathrm{Gt\,a^{-1}}$) are reported for the different estimates and discrepancies between the methods can also be found for similar time periods. Reasons for this are the large

interannual variability of surface mass balance (SMB) of 400 Gt a^{-1} and the varying error sources for the different methodologies which emphasises the need of long and multidisciplinary time-series of ice sheet mass balance (Broeke et al., 2009).

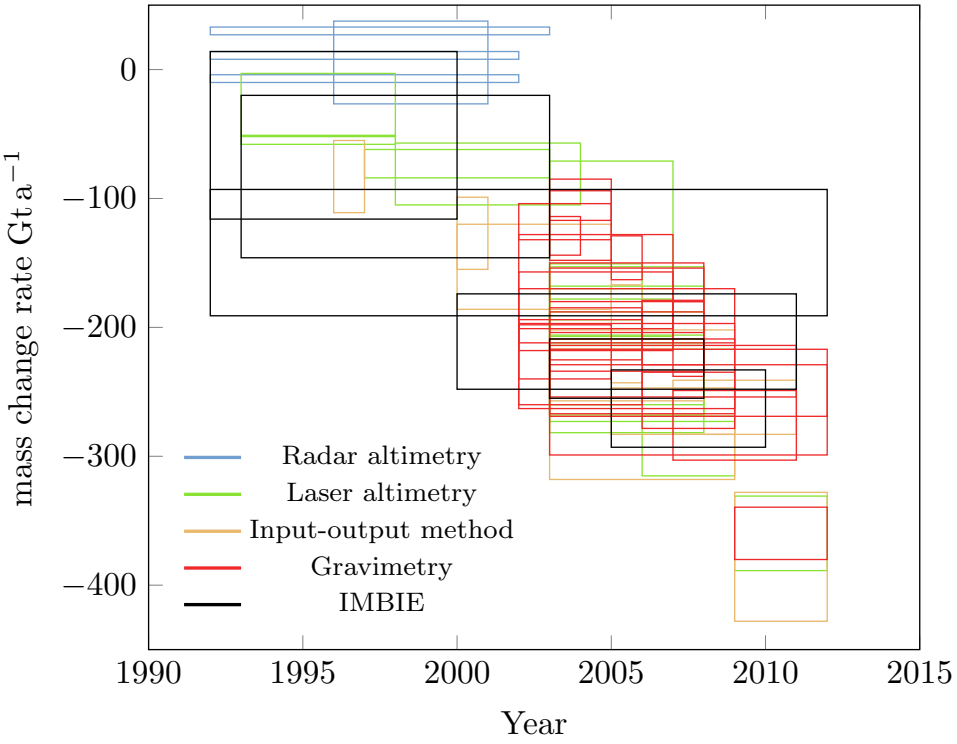

Figure 3.3: Ice sheet wide mass changes in Greenland from 1992–2012. Estimates are colour coded by the used methodology. The square extents denote time intervals and uncertainties of the mass loss rate. The plot is adopted from Khan et al. (2015) in which the corresponding references can be found.

The IMBIE projects aims to increase confidence in the mass balance trends by combining 26 studies derived from 3 different remote sensing techniques (gravimetry, altimetry, mass-budget method)(Shepherd et al., 2012, 2019). An accelerating mass loss trend for Greenland was found within IMBIE that reached 263 ± 30 Gt a^{-1} for the 2005-2010 time period. The mass loss peaked at 336 ± 62 Gt a^{-1} in 2011. The Gravity Recovery and Climate Experiment (GRACE) gravimetric measurements deliver monthly sampled time-series of mass change in Greenland. From 2003-2013 Velicogna, Sutterley, and Broeke (2014) reported Greenland's mass balance as -280 ± 58 Gt a^{-1} that is accelerating by -25.4 ± 1.2 Gt a^{-2}. However, the coarse resolution of about 300 km in the polar regions is causing signal leakage when smaller ice sheet sectors are observed independently (Shepherd et al., 2012). Radar altimetry derived mass loss of 269 ± 51 Gt a^{-1} between 2011-2014 and laser altimetry (243 ± 18 Gt a^{-1}, 2003-2009) show consistent values but suffer from the coarse resolution specifically at the ice sheet margins (Csatho et al., 2014; McMillan et al., 2016). Therefore, the volumetric mass loss estimates from altimeters are lower than the ones derived with other methods during the same time period (Mouginot et al., 2019).

Apart from ice sheet wide mass balance estimates, Mouginot et al. (2019) report the GrIS mass balance from 1972 to 2018 for individual glacier catchments. The estimates are derived by the mass-budget method combining ice velocities from

various sensors and the 1 km SMB model RACMO 2.3p2 (Noël et al., 2018). In the entire observed time period the authors find a cumulative mass balance of Greenland of -4976 ± 400 Gt which translates to a sea level rise of 13.7 ± 1.1 mm. Reported are also the individual mass balances for 260 glaciers in Greenland. An example of time-evolving mass loss of individual glaciers that was calculated with the volumetric method is found in Hurkmans et al. (2014). $\frac{dM}{dt}$ was derived with ERS and ICESat for two 5 year periods including 38 drainage basins. A detailed comparison of individual glacier mass loss in the NEGIS sector can be found in Section 4.6.1.

4 SUMMARY OF THE CONTRIBUTIONS

This chapter summarises the contributions found in the appendix and relates the findings to the research objectives set in Section 1.2. The thesis works towards providing a framework to utilise TanDEM-X (TDM) for geodetic mass calculations for large individual glaciers of the ice sheets. The methods are developed in the study region in Northeast Greenland and the final results is the geodetic mass balance for two major outlets of Northeast Greenland Ice Stream (NEGIS): Nioghalvfjersfjorden (79North) and Zachariæ Isstrøm (ZI). This chapter is split into discussions of the following glaciological parameters.

- **Drainage basin 4.1:** The drainage basin of a glacier specifies the entire area of ice that flows towards a single glacier terminus (Appendix A and F)
- **Calving front 4.2:** The calving front is needed to describe the seaward extent of a glacier basin and to calculate dynamic ice export (Appendix E)
- **Grounding line 4.3:** The grounding line marks the seaward extent of glacier mass changes that contribute to sea level rise
- **Ice velocities 4.4:** The ice velocity and flow directions are used to calculate dynamic ice export
- **Surface elevation change 4.5:** Integrated as volume change over the entire basin it represents the main input for the geodetic mass balance calculation (Appendix B, Appendix D)
- **Volumetric mass balance 4.6:** The combination of the aforementioned parameters is applied for calculating the mass balance for individual outlet glaciers in 4.6 (Appendix B)

A detailed look on detecting the thinning of the floating ice tongue of 79North is given in 4.7 (Appendix C).

4.1 DRAINAGE BASIN DELINEATION

Drainage basins are essential for partitioning mass changes of the ice sheet to the individual glacier level, as they specify the area over which basin specific measurements are integrated. The delineation of drainage basins on ice sheets is challenging due to their gentle slopes accompanied by the local terrain disturbances and complex patterns of ice movement. Until now, the basins have been mostly delineated along the major ice divides in Greenland, which results in large drainage sectors containing multiple outlet glaciers. However, when focusing on measuring glaciological parameters of individual outlet glaciers, more detailed drainage basin delineations are needed.

In order to delineate basins for the Northeast Greenland region, two independent types of data were used to infer the flow direction of ice. The first data source is

elevation information in the form of a rasterised digital elevation model (DEM), which was employed with the assumption that ice flows in the direction of the steepest downhill slope. Ice velocity measurements were utilised as a second type of data to account for locations where the ice flow diverts from the direction given by the steepest slope. This can happen where the downhill flow is obstructed by large bedrock features or through interaction with other ice masses at glacier junctions (Veen, 2013, Chapter 4.6).

For the delineation of individual glacier catchment areas, a classical flood-filling watershed algorithm was adapted to use both elevation and ice velocity data (Beucher, 1992). When operating on a DEM and associated seed points, the watershed algorithm finds the lines separating adjacent drainage basins (Vincent and Soille, 1991). An implementation of the watershed algorithm was utilised which applies a priority queue that is sorted by minimum elevation (Barnes, Lehman, and Mulla, 2014). During the algorithm run, pixels adjacent to each seed point are entered into the queue and are processed in the order of increasing elevation. This ensures a pixel-wise processing, with regions evolving from given seed points to form a partitioning of the area of interest. After all pixels have been processed, the drainage divides of the DEM have been generated by the watershed algorithm.

In order to accommodate velocity information in the traditional watershed algorithm, streamlines were calculated from the x- and y- velocity components. They describe the trajectory that imaginary particles would take in the given velocity field. Discrete streamlines were produced with the procedure described by Cabral and Leedom (1993) but the calculation was restricted to areas moving faster than a given absolute velocity threshold (slower areas were discarded, Figure 4.1). This threshold was found in a correlation analysis of ice flow directions from synthetic aperture radar (SAR) offset tracking with slope aspect angles of a smoothed DEM of the region. Details for this procedure can be found in Appendix A.

The streamline computation itself is included in the modified watershed algorithm starting from a given pixel and ending once the streamline extends beyond the coverage of the velocity field or if the streamline merges with an already existing one (Algorithm 1).

To combine the directional information from ice velocity measurements with the slope information from a DEM smoothed over distances of 20-times the local ice thickness, the traditional watershed algorithm was modified to disregard slope information in areas of fast moving ice where the velocity magnitude exceeds the pre-defined threshold. Instead, every time such an area is encountered, the entire labelled flow line is included in the currently processed drainage area and its entire neighbourhood is entered in the priority queue of the watershed algorithm.

Seed locations are required for each catchment in order to start the partitioning of the ice sheet into drainage basins. The seed regions are defined on the ice of the termini marking areas upstream from the glacier front. Thus the seed regions belong to the part of the tongue where ice is discharged into the ocean or where the glacier is terminating on land. The seed regions for the study site are visualised in Figure 4.2. Three types of seed regions were defined to support the processing: (1) on each terminus of the 31 marine terminating glaciers considered for catchment delineation (2) several seed regions of small unnamed glaciers that flow also to the ice sheet margin and (3) a large one located along the ice divides outside the rough outline of the complete Northeast Greenland drainage region. Regions of type (1) and (2) act as

Algorithm 1 The combined watershed algorithm is an adaptation of an implementation by Barnes, Lehman, and Mulla (2014) utilising a priority queue that returns its elements based on a priority level. In this case elements with lowest elevation are returned first. Additional to the element's elevation information each queue entry also has a seed label attached that is equal to the seed label that was processed at the time of the element's insertion.

Require: *dem*, *iceVelocity*, *seedPoints*, *velocityThreshold*

Let Q be a priorityQueue
Let *labels* have the same dimensions as *dem*
Let *labels* be initialised to 0
for all $s \in seedPoints$ **do**
    Push s onto Q with priority $dem(s)$ and seed label $seedLabel(s)$
    $labels(s) \leftarrow seedLabel(s)$
while $Q \neq \varnothing$ **do**
    $p \leftarrow POP(Q)$
    if $labels(p) > 0$ **then**
        continue
    else if $iceVelocity(p) > velocityThreshold$ **then**
        Calculate upstream streamline *line* for starting pixel p
        $labels(line) \leftarrow p.seedLabel$
        for all neighbours n of *line* **do**
            if $labels(n) > 0$ **then**
                continue
            Push n onto Q with priority $dem(n)$ and seed label $p.seedLabel$
    else
        $labels(p) \leftarrow p.seedLabel$
        for all neighbours n of p **do**
            if $labels(n) > 0$ **then**
                continue
            Push n onto Q with priority $dem(n)$ and seed label $p.seedLabel$

sinks in the ice sheet's flow system, while region (3) simulates the glaciers draining into the adjacent West and Southeast Greenland regions.

In order to mitigate the propagation of local errors in the datasets to global errors in the drainage delineation a Monte-Carlo method adding Gaussian noise with zero mean was applied to the DEM and the ice velocity components as well as the used ice velocity threshold. In this setting $N = 10000$ runs of the algorithm were performed using the pixel-wise uncertainties for the x and y ice velocity components. The standard deviation for the DEM and ice velocity threshold were set to $\sigma_{DEM} = 10\,\mathrm{m}$ and $\sigma_t = 2\,\mathrm{m\,a^{-1}}$, respectively. Subsequently, each pixel was assigned the basin label of maximal occurrence in all runs and a probability measurement was calculated based on the percentage of total Monte-Carlo runs for which that pixel was included in that particular basin. Noisy delineations at the basin boundaries were cleaned by restricting the number of connected clusters per label to 1.

Resulting are 31 individual glacier drainage basins for the Northeast Greenland region. Their corresponding probability maps are shown in Figure 4.3. The drainage basin statistics for each of the outlet glaciers can be found in Table 4.1 and the full

dataset of all generated drainage basins is published online (Krieger, Floricioiu, and Neckel, 2019).

The importance of using additional velocity information for watershed delineation is illustrated at the boundary between 79North and ZI (Figure 4.4). The classical approach of deriving the drainage divide based solely on the TDM global DEM was compared with the border obtained when additional ice flow directions are used. While in agreement at low altitudes, the watershed lines resulting from the two methods start to deviate from each other with increasing elevation. In this area the ice speed is $>300\,\mathrm{m\,a^{-1}}$ and the assumption that velocity vectors point down-slope does not hold. This can be a result of an interaction of the two branches of NEGIS, the disturbance of ice flow by a large subglacial bedrock feature or an ice sheet imbalance. The iterative nature of the watershed algorithm causes preceding errors during processing to propagate to areas of higher elevations and thus the resulting watershed lines can deviate significantly from each other. As revealed by the flow lines in Figure 4.4, an approx. 20 km wide part of NEGIS is incorrectly attributed to ZI. As a result, the ice area which feeds that part of the ice stream is misclassified if ice velocities are not included during the catchment delineation.

There is only one set of individual outlet glacier catchments for ice sheets, that is comparable to the reported findings presented here. This dataset is published by Mouginot and Rignot (2019) and also uses ice velocities as additional means to investigate ice flow direction. Previously delineated basins by Zwally et al. (2012, Figure 4.2) are not usable for mass balance reporting on the individual glacier level because many glaciers were aggregated in one common ice sheet sector.

Although the basins by Mouginot and Rignot (2019) show overall similarity to the catchments presented here, they lack a description of the methodology used for their generation and they have not been publicly available at the time of investigation. I establish for the first time a fully traceable methodology that has the potential to produce outlines of drainage basins for entire Greenland and Antarctica. Moreover, the quality of the presented results was further assessed by a probability measure from additional Monte-Carlo experiments that allows to identify locations on the ice sheet that are critical for the delineations of glacier catchments or that are likely to change in the future. The delineated catchment areas were compared to the previously published basins by Mouginot and Rignot (2019) in Table 4.1. According to my findings, the glacier catchments of 79North and ZI are 2559 $\mathrm{km^2}$ and 6864 $\mathrm{km^2}$ smaller compared to the corresponding basins in Mouginot and Rignot (2019) after correcting for the different seaward basin extent in the two datasets. Relative to the total basin area, larger discrepancies are found for Wordie Gletscher (32%) or Adolf Hoel Gletscher (110%). Two large basins of the surge-type Storstrømmen and Kofoed-Hansen Bræ are not included in the comparison because their catchments are combined in Mouginot and Rignot (2019). The discrepancies can arise for various reasons, including the choice of the DEM, the velocity dataset or the used methodology. Moreover, a clear definition is needed for the points of drainage to land and ocean (seed regions). Mouginot and Rignot (2019) neither describe the methodology nor the seed point selection in detail.

In the future, the delineation will be carried out to generate catchments for entire Greenland and Antarctica. Additionally, repeated investigations should be performed for the same area to detect changes in the ice sheet flow regimes that can be the result of seasonal or multiyear variations (Section 5.2.1).

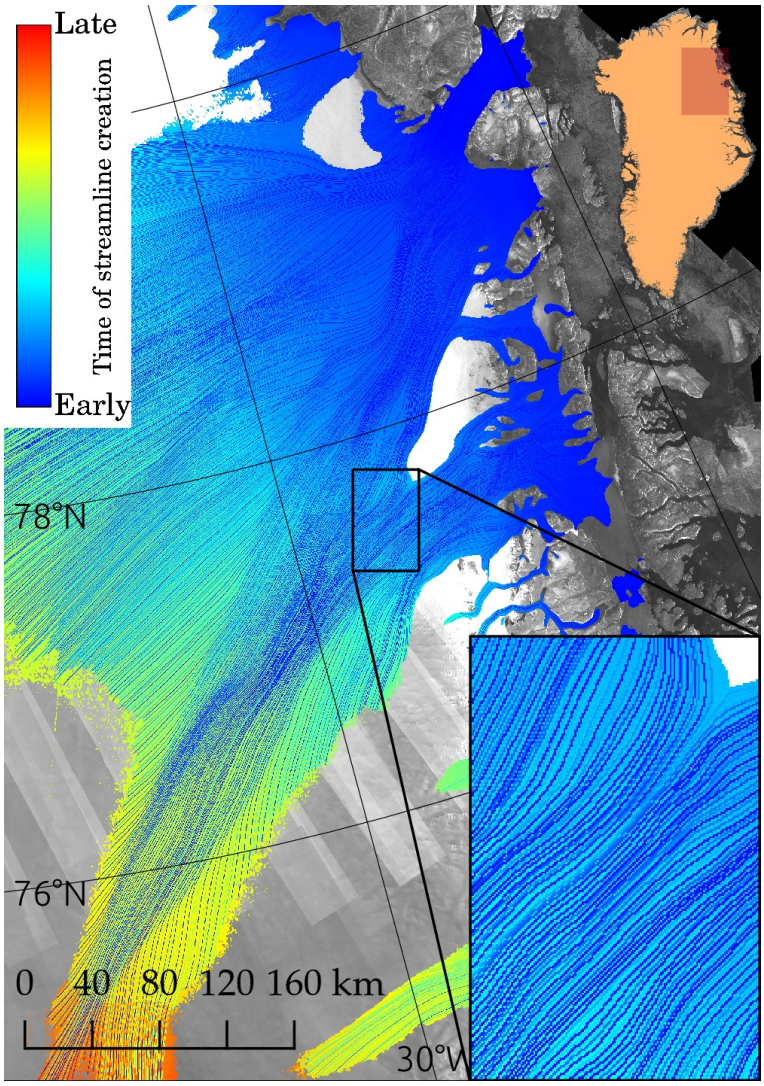

Figure 4.1: The streamlines for the NEGIS drainage sector colour coded by the time of creation during the modified watershed algorithm. The streamlines have been calculated for ice speeds exceeding 13.67 m a^{-1}. Dark-blue refers to streamlines originating from low altitudes close to the coast propagating to the upper part of NEGIS. Light-blue to red colours are associated to streamlines starting at higher elevations. The inset shows streamlines clearly separating NEGIS into two arms. In the background, the TDM SAR backscattering amplitude mosaic is displayed.

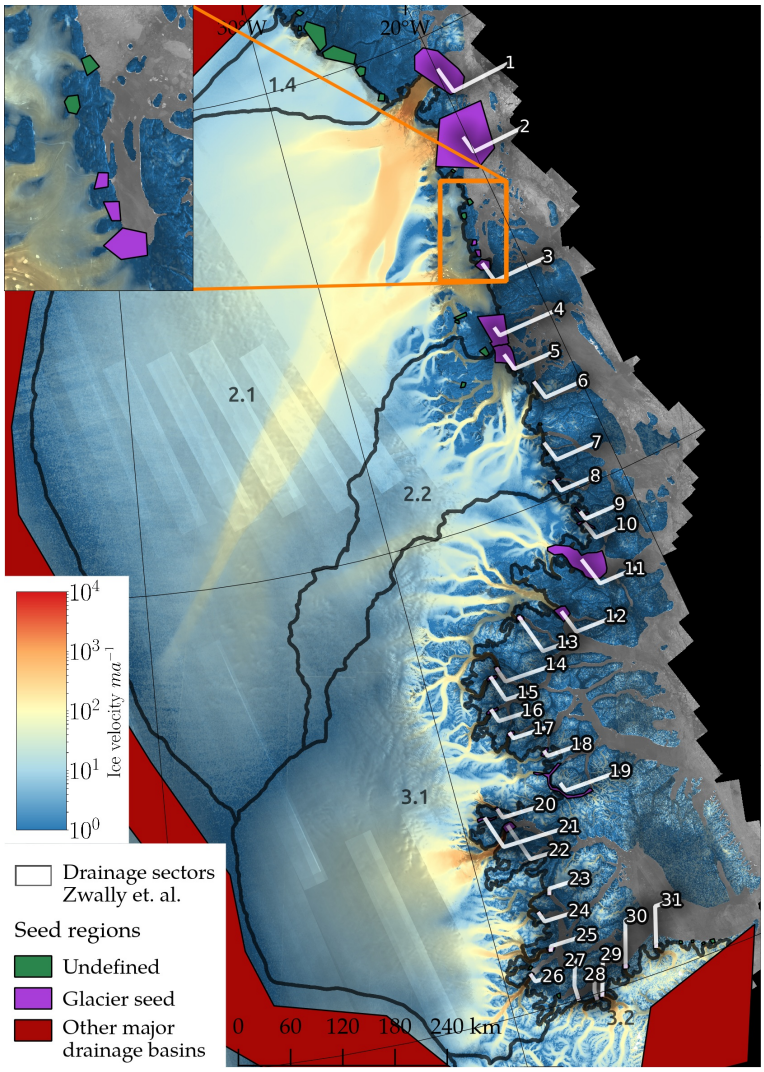

Figure 4.2: The study site with 31 outlet glacier seed regions (magenta) of the basins listed in Table 4.1. Additional termini of small outlet glaciers or land terminating glaciers are marked as *undefined* seeds (green). Drainage to other major regions of Greenland is simulated by a rough outline around the Northeast Greenland sector (red). In the background, the ice surface velocity map from Sentinel-1 (Nagler et al., 2015a) is superimposed on the TDM global DEM backscattering mosaic. Black lines delineate the basins after Zwally et al. (2012).

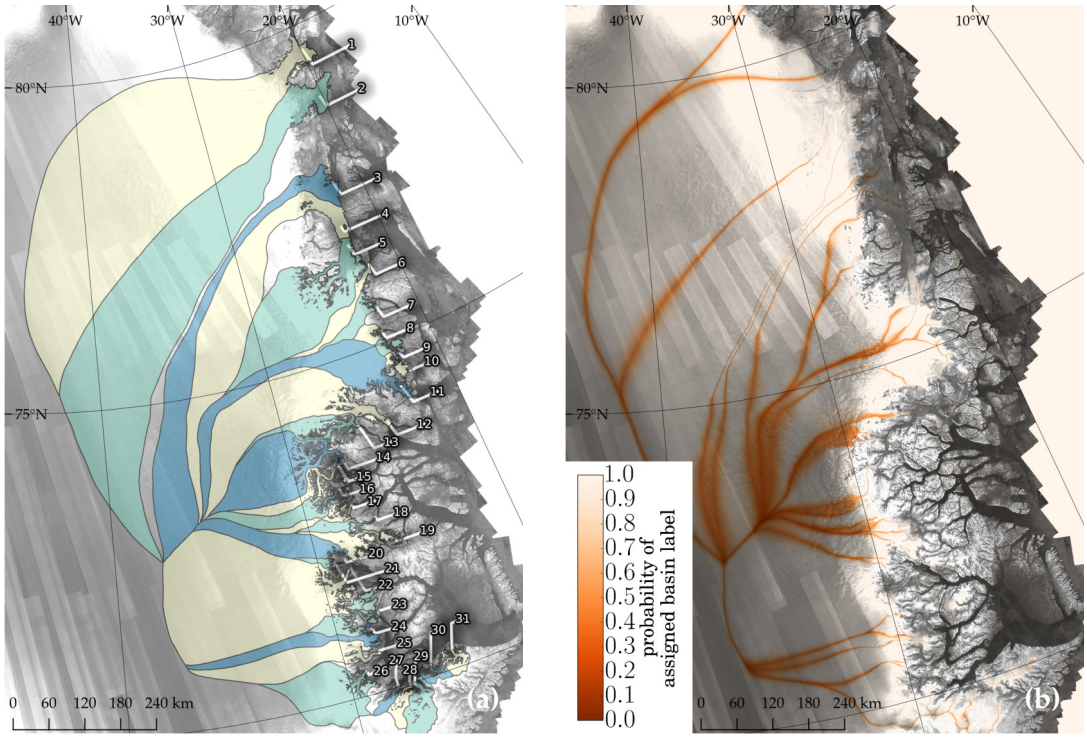

Figure 4.3: (a) Northeast Greenland Ice Sheet region divided into drainage basins of the 31 outlet glaciers in Table 4.1. (b) The pixel-wise probability of the assigned basin label for each basin. In the background, the SAR backscattering amplitude layer of the TDM global DEM is displayed.

Table 4.1: Drainage basin areas $\mathcal{A}$ for each numbered glacier as in Figure 4.2. The ice volume $\mathcal{V}$ is calculated with the Bedmachine dataset (Morlighem et al., 2017a,b). Area fractions $\mathcal{A}_{frac}$ are given with respect to the total Greenland Ice Sheet area (Howat, Negrete, and Smith, 2014). Area differences $\Delta\mathcal{A}$ are reported for corresponding catchments in Mouginot and Rignot (2019) and sea level equivalents (SLEs) were calculated.

#	Glacier name	$\mathcal{A}$ [km^2]	$\mathcal{A}_{frac}$ [%]	$\mathcal{V}$ [km^3]	$\Delta\mathcal{A}$ [km^2]	SLE [m]
1	Nioghalvfjerdsfjorden (79North)	107791	6.28	227424	-2559	0.58
2	Zachariæ Isstrøm	84398	4.92	200199	-6864	0.51
3	Kofoed-Hansen Bræ	74686	4.35	173136	-	0.44
22	Daugaard-Jensen	48369	2.82	110810	-1557	0.28
4	Storstrømmen	28859	1.68	53872	-	0.14
12	Waltershausen Gletscher	23141	1.35	34821	-990	0.09
5	L. Bistrup Bræ	21868	1.27	24648	233	0.06
14	Gerard de Geer Gletscher	15735	0.92	19932	2267	0.05
11	Wordie Gletscher	14995	0.87	21686	4771	0.05
26	Vestfjord Gletscher	11806	0.69	11506	590	0.03
25	Rolige Gletscher	9917	0.58	18003	-	0.05
20	F. Graae Gletscher	7288	0.42	12754	1781	0.03
16	Nordenskiöld Gletscher	5209	0.30	6967	1132	0.02
24	Unnamed Hare Fjord	5170	0.30	9683	-	0.02
13	Adolf Hoel Gletscher	4323	0.25	1845	-4773	0.00
15	Jættegletscher	3819	0.22	3154	-1710	0.01
29	Magga Dan Gletscher	3768	0.22	2120	-672	0.01
23	Eielson Gletscher	3700	0.22	1404	-	0.00
19	Violingletscher	3432	0.20	1162	-	0.00
6	Soranerbræen Gletscher	2956	0.17	2655	-	0.01
7	Einar Mikkelsen Gletscher	2263	0.13	1597	-	0.00
17	Hisinger Gletscher	1939	0.11	1568	-932	0.00
18	Wahlenberg Gletscher	1559	0.09	988	-	0.00
31	Bredegletscher	1546	0.09	254	276	0.00
28	Kista Dan Gletscher	1524	0.09	934	-	0.00
8	Heinkel Gletscher	1093	0.06	417	-	0.00
30	Sydbræ	1072	0.06	148	-93	0.00
27	Unnamed Vestfjord S	931	0.05	250	-	0.00
9	Tvegegletscher	924	0.05	130	-	0.00
10	Pasterze	743	0.04	16	-	0.00
21	Charcot Gletscher	580	0.03	360	-572	0.00

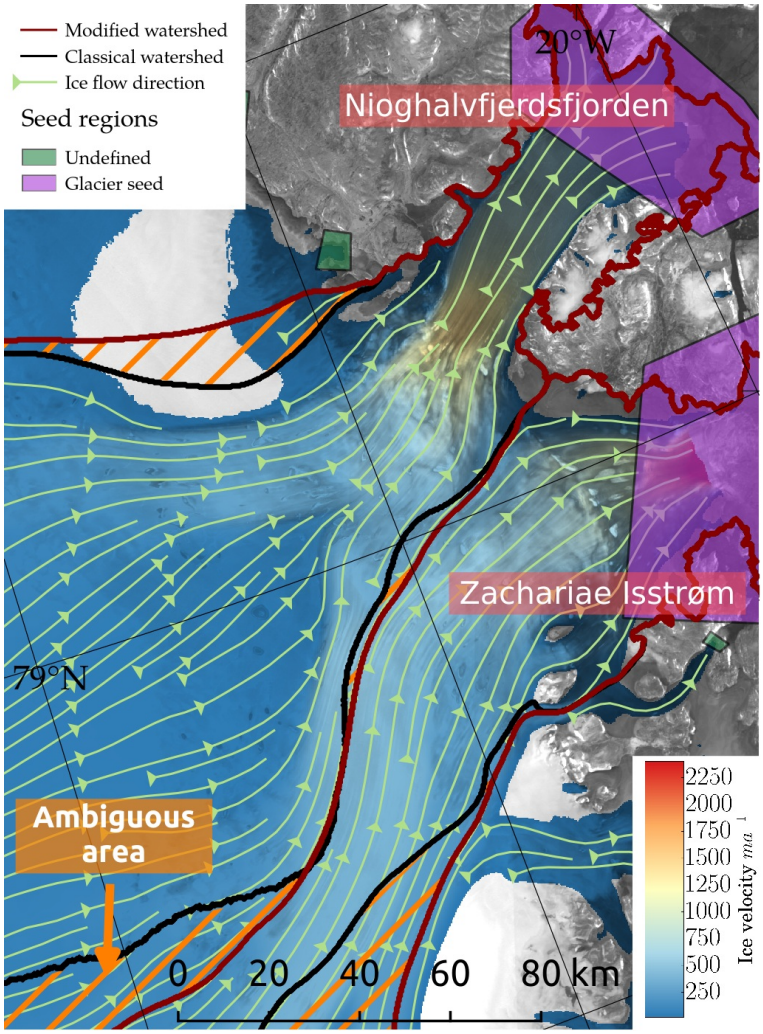

Figure 4.4: Watershed lines separating the two glaciers 79North and ZI derived by the classical watershed algorithm based solely on DEM information (black line) compared to the basin boundary when additional ice velocity is used (red line). The disagreement between the drainage divides leads to an ambiguous area which according to the ice flow direction (green arrows) is misclassified by the classical watershed procedure. In the background, the TDM SAR backscattering amplitude mosaic is displayed.

4.2 CALVING FRONT

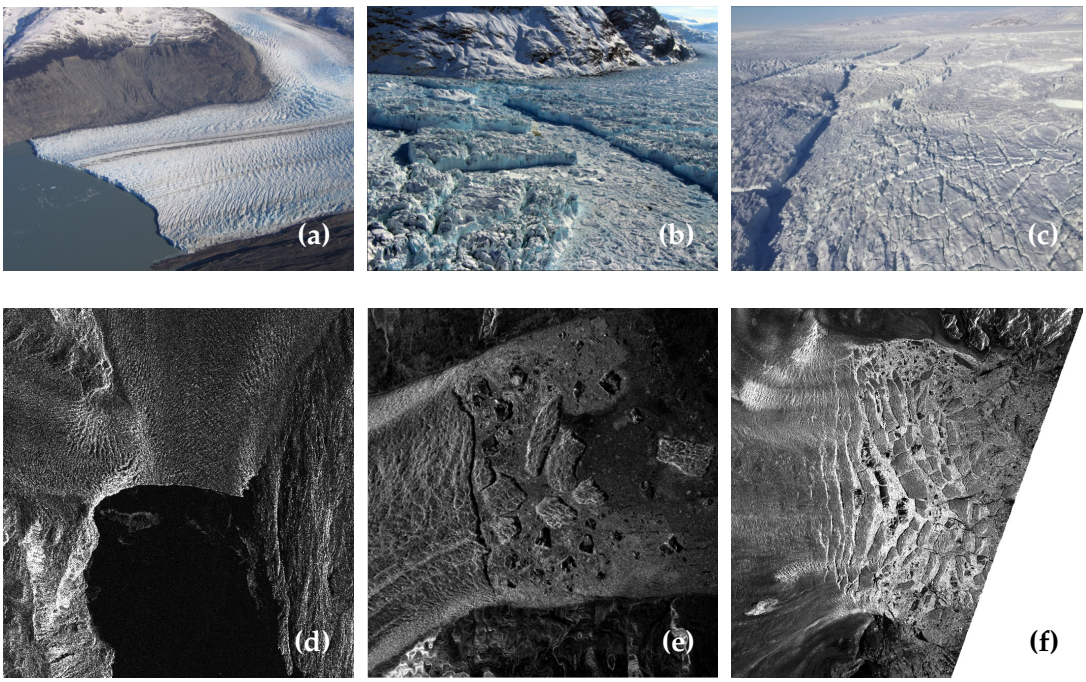

Figure 4.5: Calving front examples for (a) Upsala glacier (Calafate Extremo, panoramino.com) (b) Daugaard-Jensen (DJ) (Operation IceBridge 2017) and (c) ZI (Operation IceBridge 2017). Exemplary SAR images for similar conditions show (d) dark calm water, (e) iceberg presence and (f) a strongly crevassed terminus with the presence of ice mélange.

The calving front is an important parameter to calculate dynamic mass loss for glaciers that are grounded at the front. This is the location where the glacial ice breaks off into the ocean and is no longer physically connected to the ice sheet. The mass flux across this line therefore equals the mass lost due to calving.

The conditions at the calving front differ depending on the glacier location, the season or the dynamic behaviour of the glacier. In general, high ice export rates lead to more iceberg presence in the fjord as well as the formation of ice mélange which both show similar backscattering characteristics as glacial ice. A strongly crevassed terminus which is also often found at these types of glaciers also impedes the delineation of the calving front. In contrast, calm water is easily distinguishable from the glacier ice (Figure 4.5).

Time-series of calving fronts have been delineated for ZI and DJ. To this end, an algorithm has been developed that is able to delineate calving front locations of outlet glaciers on SAR amplitude backscattering images. Calving fronts were produced from Sentinel-1 and TerraSAR-X (TSX) data by first enhancing edges and then using path optimisation to find the best calving front candidate line between the adjacent fjord walls. It is shown that results can even be obtained in conditions where the glacier front is crevassed and large icebergs are present in the fjord. Nevertheless, the algorithm is not stable enough to be used without supervision and therefore the

required frontal line for mass balance modelling in Section 4.6 have been delineated by hand.

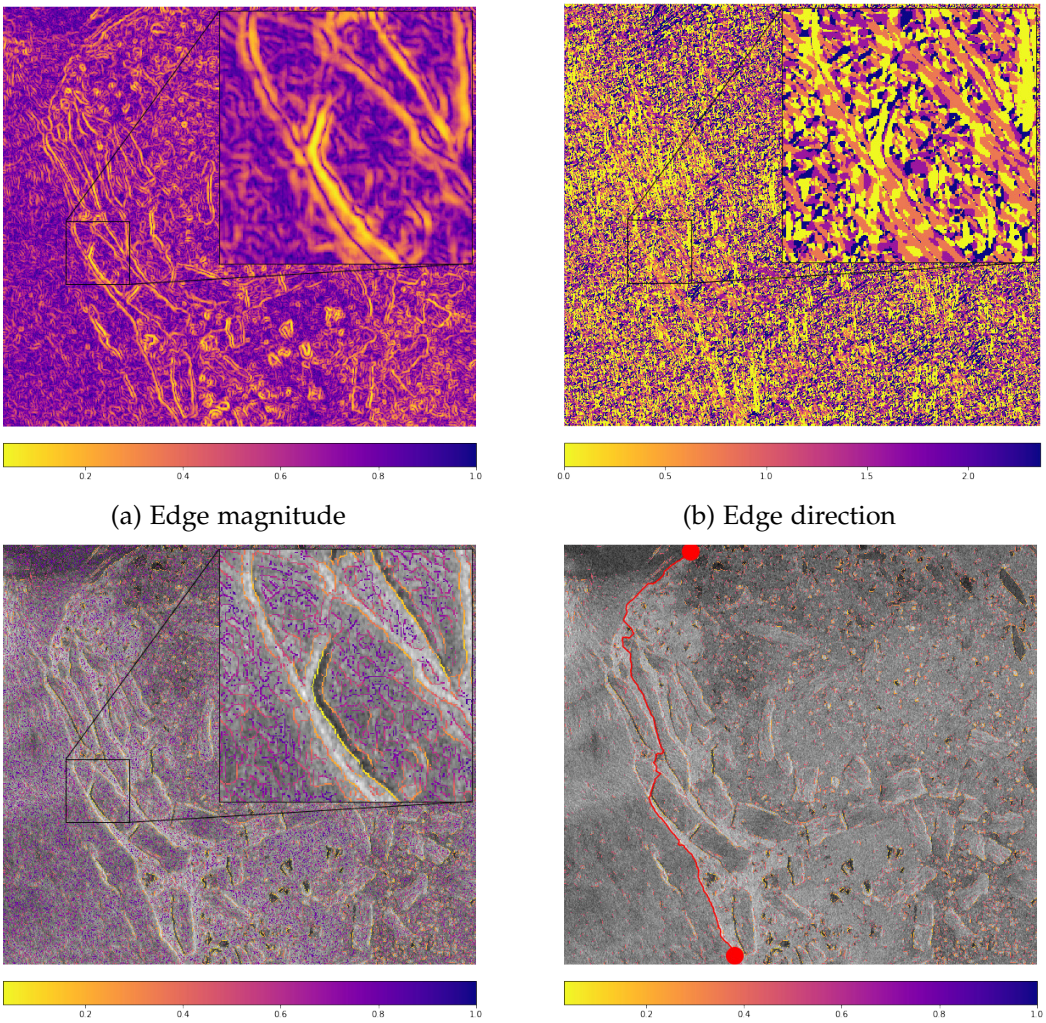

(a) Edge magnitude

(b) Edge direction

(c) Non-maximum suppression

(d) Optimal path

Figure 4.6: The ratio of averages (ROA) estimates edge magnitude and direction to be able to find exact edge locations in SAR images through a non-maximum suppression step (Fjortoft et al., 1998). The problem of finding optimal paths for the front across a crevassed terminus with icebergs and ice mélange remains.

An early version of this algorithm can be found in Appendix E but has since been expanded by a different scheme for edge detection and improved filtering when time-series of SAR images are available. As an alternative to the Canny edge detector presented in Appendix E, the ROA as described in Fjortoft et al. (1998) is used for the results shown in Figure 4.6 and 4.7. A previously detected front can also be used to define a search corridor for the current delineation by assuming typical advance and retreat rates for a glacier, lowering the number of possible erroneous detections due to icebergs and mélange. This has led to a time-series of calving fronts of ZI between 2016-11-11 and 2017-05-22 (Figure 4.8).

With Mohajerani et al. (2019) and Baumhoer et al. (2019), two deep learning based methods have been proposed to track the calving front on satellite imagery. The

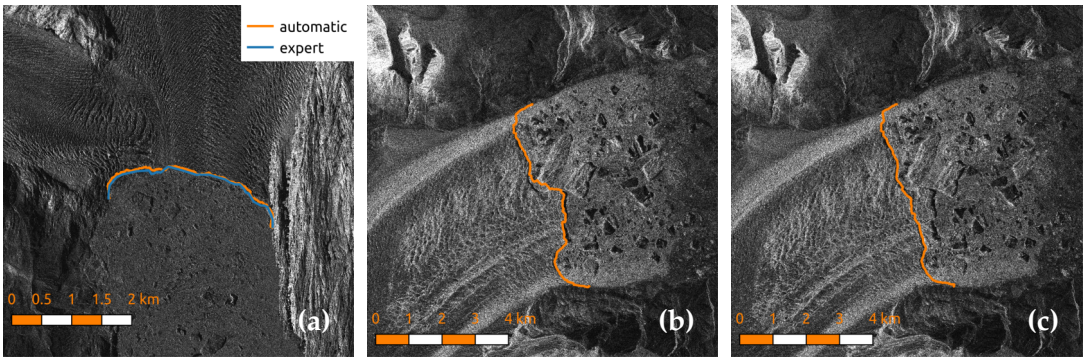

Figure 4.7: Delineations of calving fronts with the ROA edge detector. (a) the algorithmic detection and manual digitisation of the front line at Upsala glacier in Patagonia at 2011-02-26. (b) and (c) are consecutive images from 2015-02-20 and 2015-03-03 of DJ that highlight the calving of a large iceberg in the middle of the calving front.

approach of Mohajerani et al. (2019) is similar to the method proposed here but features an improved edge detection on Landsat images based on a convolutional neural network (CNN). Afterwards, the calving front is detected based on energy minimisation comparable to Krieger and Floricioiu (2017) (Appendix E). The results by Mohajerani et al. (2019) have slightly better accuracies of 96.3 m compared to the result in Krieger and Floricioiu (2017) in the case of a successful delineation (159 m). Of importance is however, to detect the calving fronts on SAR images as only this sensor allows to build up reliable time-series of the entire calving front without missing or partial coverages due to polar night or cloud cover. The applicability of my method to a SAR time-series is shown in Figure 4.8.

The focus of Baumhoer et al. (2019) lies on the circum-Antarctic detection of the calving front on SAR imagery based on pixel-wise segmentation of glacial ice and surrounding areas. The segmentation uses the coarse resolution (ca. 50×50 m) dual-pol Sentinel-1 EW mode and also requires additional DEM data compared to the proposed approach here which is applicable to smaller outlet glaciers with widths of 1–100 km. Baumhoer et al. (2019) is therefore not directly applicable on higher resolution SAR images of TSX that are needed for smaller sized outlet glaciers for example in the Patagonian Ice Fields. In general however, all mentioned approaches show the ability to produce accurate calving front delineations for glaciers in clear conditions. This includes cases in which sea ice shows distinct backscatter characteristics or the water is ice free close to the glacier calving front. This facilitates the detection of the actual calving front both for edge-detection based as well as region based approaches. If however, the tracked terminus becomes more crevassed, the exact calving front is more difficult to detect accurately with the methods described here. The resulting effect is that just at the dynamic outlet glaciers which are characterised by high ice export and strong crevassing, the algorithmic detection of the calving front is error prone and remains an unsolved topic in the remote sensing of the cryosphere (Section 5.2.4).

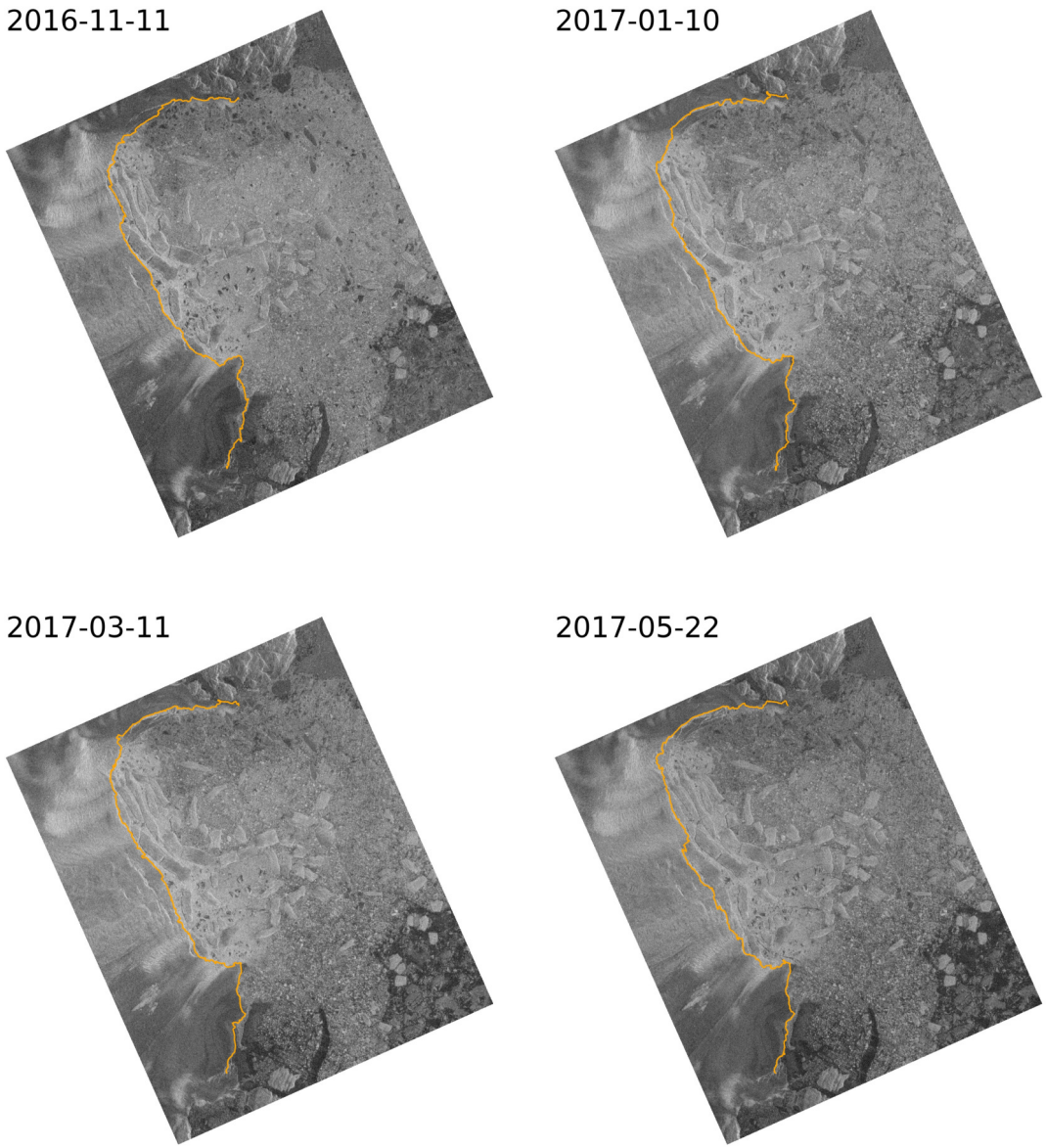

Figure 4.8: Calving front time-series for ZI detected on Sentinel-1 IW amplitude backscattering images. On the central part of the terminus a new crevasse is opening up that is finally tracked in the last image of the time-series.

4.3 GROUNDING LINE

In order to identify grounding line positions at 79North, a triplet of TSX acquisitions was formed for winter 2013 to apply differential interferometric SAR (InSAR) (DInSAR) and a single interferogram, using 3-day repeat pass European Remote Sensing Satellite (ERS) scenes, was calculated for winter 2010. The used acquisitions are detailed in Table 4.2. For the TSX stack, the middle scene was selected as master and forward and backward interferograms have been generated. The two resulting interferograms have been added to form the double difference interferogram. The grounding line was delineated by hand at the landward border of the visible fringe belts in the TSX and ERS interferograms. In this thesis, the exact location of the fringe belt has been approximated in decorrelated regions and the final delineation is shown in Figure 4.9.

The tide annotation has been calculated with the Arctic Ocean Tidal Inverse Model (AOTIM)-5 tide model, for a point at 79.6°N 19.5°E which is the closest point available on the modelling grid (Padman and Erofeeva, 2004). Afterwards, the modelled tide levels were corrected with air pressure provided by the NCEP/NCAR Reanalysis 1 project (Kalnay et al., 1996). Finally, the differential tide corresponds to the displacement measured in the double difference interferograms. Inconsistencies between the measured ice shelf displacement and the modelled differential tide are possible because of the unknown bathymetry under the ice shelves (Padman et al., 2002).

With Sentinel-1 I also applied this procedure for the Getz Ice Shelf in Antarctica where wide spread grounding line retreat could be detected (Figure 3.2). These results are not part of this thesis and stand exemplary for state of the art InSAR grounding line delineation. Tide annotations have been calculated with the Circum-Antarctic Tidal Simulation (CATS) model in this case (Padman et al., 2002).

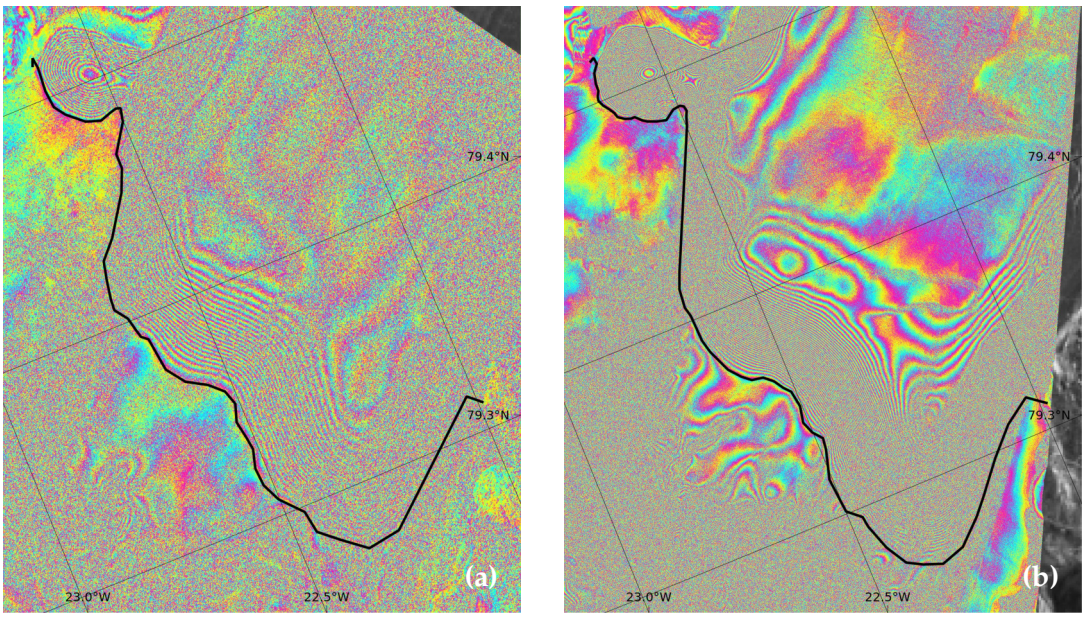

Figure 4.9: Fringe belts at the grounding line of 79North in (a) an ERS interferogram from 2011-03-20 and (b) a double difference interferogram of TSX from 2014-01-21.

Table 4.2: The TSX scenes used for the detection of the grounding line at 79North. Tide annotations have been calculated with the AOTIM-5 tide model and were corrected for air pressure with NCEP/NCAR Reanalysis data (Kalnay et al., 1996; Padman and Erofeeva, 2004).

Sensor	Date	Relative orbit	Orbit direction	Tide level [m]	Air pressure [hPa]	Corrected tide level [m]	Differential tide [m]
ERS	2011-03-20	15	A	0.527	995.56	0.351	-0.321
	2011-03-23			0.028	1013.41	0.030	
TSX	2014-01-10	50	D	-0.122	1001.82	-0.236	0.632
	2014-01-21			-0.336	1014.08	-0.328	
	2014-02-01			0.196	1013.45	0.198	

Grounding line detection with DInSAR is a well-established technique which is currently operationally used to deliver grounding lines within the projects Making Earth System Data Records for Use in Research Environments (MEaSUREs) and European Space Agency (ESA)'s Climate Change Initiative (CCI). All improvements on the generation of coherent interferograms directly result in a better detection of the grounding line in double difference interferograms. In this thesis, the same acquisitions as in Mouginot et al. (2015) were used, as they were suitable for the delineation of the grounding line at 79North but additionally the modelled tide levels corrected for air pressure were reported. Tide levels are not regularly annotated for many grounding line datasets including the largest available InSAR dataset of grounding line locations which was generated within the MEaSUREs project (Rignot, Mouginot, and Scheuchl, 2016). In many cases even the exact acquisition times of the used scenes are omitted which makes a retroactive calculation of the tide annotations unfeasible. These annotations are however essential to analyse tide-induced grounding line movement and to be able to distinguish it from actual migration of the grounding line driven by subglacial melting. The tide-induced migration of the grounding zone can be at the scale of kilometres depending on the slope of the bedrock at the grounding zone and the respective maximum tide occurring within the stack of the interferogram triplets (Milillo et al., 2017).

Two high impact improvements are apparent for the operational detection of the grounding line with DInSAR in the future. The first is a possible 1-day repeat-pass constellation of the future Sentinel-1 C mission which would produce more coherent interferograms especially over fast flowing outlet glaciers and therefore increases the coverage of possible grounding line delineations. Secondly, advances for the algorithmic detection of the landward border of the DInSAR fringe belt have to be developed to make use of the existing operational processing of the double differencing interferograms. One such approach, which is currently under investigation by the Remote Sensing Technology Institute (SAR Signal Processing), is to measure phase gradients in the double difference interferogram. The grounding line is then delineated with the help of a fixed elastic beam model for the tidal ice shelf displacement that can explain the measured phase gradients (Rignot, 1996).

Another contribution of DInSAR processing over ice shelves is the possibility to improve established tide models whose typical accuracies are worse than those

achieved with interferometric measurements from SAR (Wild, Marsh, and Rack, 2019). The shape of the fringe belt and the number of fringes can be used to draw conclusions about the local small scale bathymetry and ice thickness. The InSAR-derived displacement represents a direct measurement of the actual vertical tide motion. This can be used to combine the spatial benefits of DInSAR with the temporal sampling of tide models.

The two grounding lines presented here (Figure 4.9) were specifically produced to determine the seaward grounded ice extent of 79North which was required for the geodetic mass balance calculations in Section 4.6.

4.4 ICE VELOCITY

Ice velocity maps were derived from 11-day repeat pass TSX data. To this end, amplitude backscattering images were produced from pairs of TSX Single look Slant range Complex (SSC) products and normalised cross-correlation was used to track glacier features and speckle in range and azimuth direction. These shifts were projected on a DEM and transferred to northing and easting in order to report the velocity vector in a metric coordinate system. The Figures 4.10, 4.11, 4.12, 4.13 and 4.14 show velocity maps over the major outlet glaciers in Northeast Greenland. They were geo-referenced with elevations from the Greenland Ice Mapping Project (GIMP).

Erroneous velocity estimates were discarded by filtering according to Lüttig, Neckel, and Humbert (2017). First, velocity estimates exceeding a certain absolute velocity specific to each glacier were removed. Afterwards, remaining points were filtered based on the magnitude and flow direction in a 9×9 neighbourhood. If the flow direction differed by more than 20° from the mean flow direction in the neighbourhood or if the velocity magnitude deviated more than 40% from the neighbourhood median, the respective measurements were discarded.

The ice velocities presented here were produced initially to identify the fastest flowing and most dynamic glaciers in the study area. The processing of ice velocities itself has developed to a standard procedure for the use of SAR data in the recent years (Section 3.2). Especially, since the start of the Sentinel-1 mission, velocity products for the ice sheets are now operationally produced with dense temporal sampling. Still the higher resolution capabilities of TSX are needed to resolve velocities close to the glacier shear margin where systematic differences of up to $700\,\mathrm{m\,a^{-1}}$ to Sentinel-1 velocities have been found (Joughin, Smith, and Howat, 2018b). High resolution velocity fields are therefore important to calculate accurate discharge rates for flux gates that span the entire glacier widths.

In order to document the speed-up of ZI, a time-series of ice velocity along the central flowline is visualised in Figure 4.15. The plot shows the rapidly increasing ice velocity on the terminus of ZI from a maximum of $5\,\mathrm{m\,d^{-1}}$ in 2011 to $>8\,\mathrm{m\,d^{-1}}$ in the summer of 2016. With the help of this time-series and manually delineated calving fronts for Jan. 2011 and Jan. 2014 an average ice export of $12.83\,\mathrm{Gt\,a^{-1}}$ has been calculated for ZI for the time between Jan. 2011 and Jan. 2014. The necessary ice thickness at the flux gate has been calculated from Multichannel Coherent Radar Depth Sounder (MCoRDS) acquisitions of a crossing Operation IceBridge (OIB) flight line close to the glacier calving front on 2010-05-25 and the respective TDM DEMs as processed in Section 4.5 (Paden et al., 2010, updated 2019). The calculated ice export

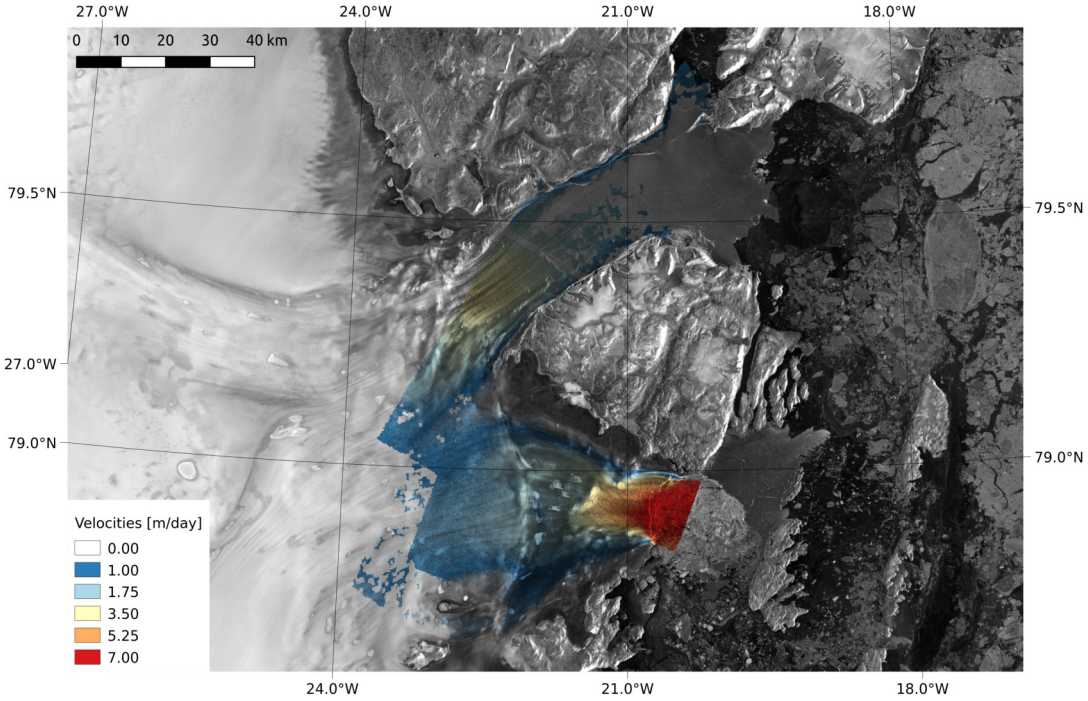

Figure 4.10: Ice velocity map of 79North and ZI overlaid on an amplitude backscattering mosaic by Joughin (2015).

rate is comparable to an average ice discharge of 13.27 Gt a^{-1} (mid. 2010 - mid. 2014) reported in a detailed study by Mouginot et al. (2019) spanning the time from 1972 until 2018 for 260 glaciers in Greenland. The ice export rate was used to validate our inferred ice export at ZI of 12.54 Gt a^{-1} (Section 4.6, Table 4.4) which is the result of subtracting modelled surface mass balance (SMB) from the geodetic mass balance.

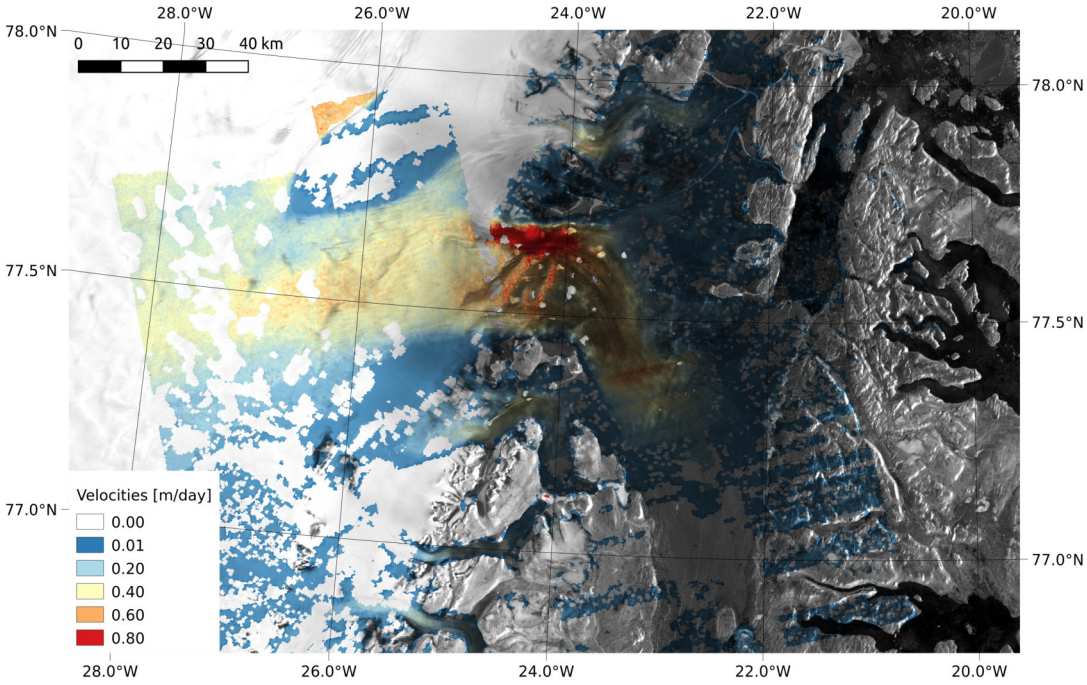

Figure 4.11: Ice velocity map of Storstrømmen and Kofoed-Hansen Bræ overlaid on an amplitude backscattering mosaic by Joughin (2015).

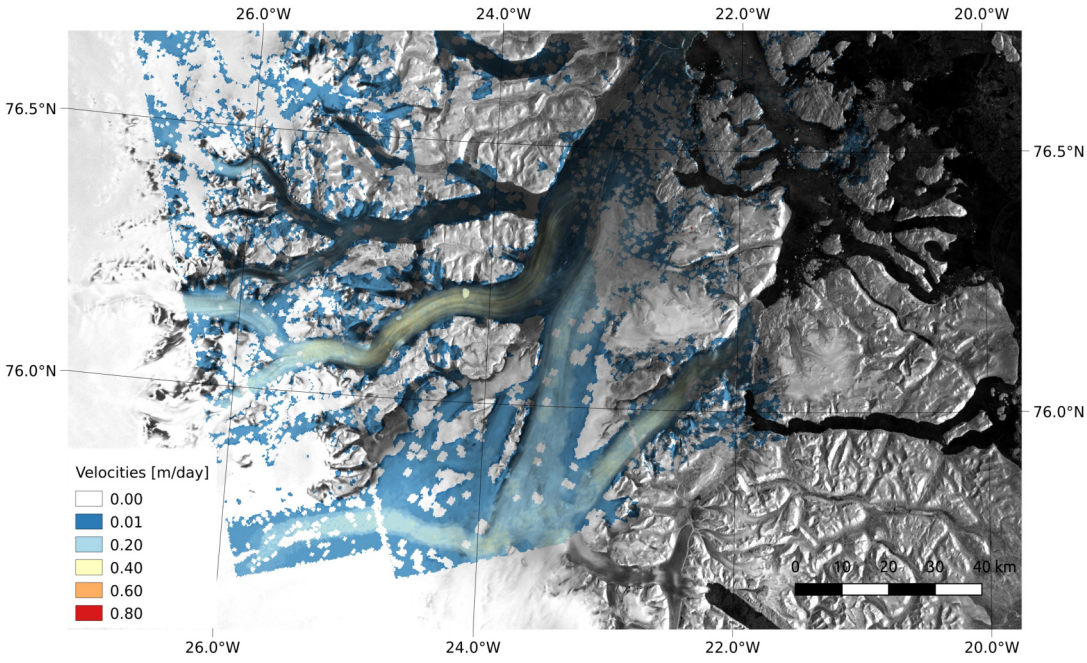

Figure 4.12: Ice velocity map of L. Bistrup Bræ and Storstrømmen overlaid on an amplitude backscattering mosaic by Joughin (2015).

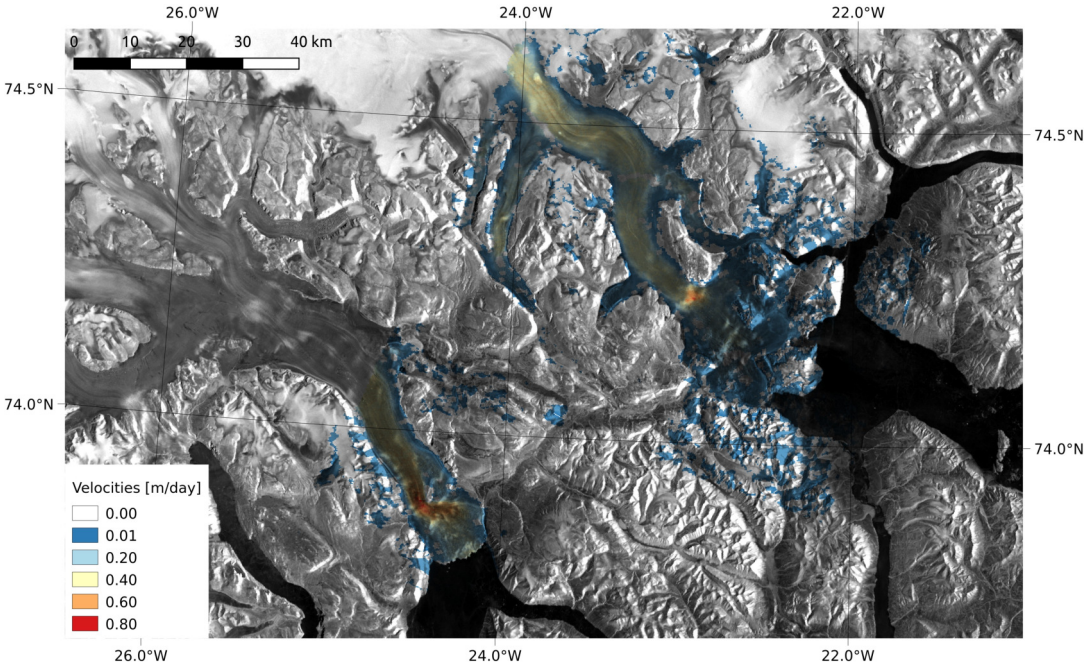

Figure 4.13: Ice velocity map of Waltershausen Gletscher and Wordie Gletscher overlaid on an amplitude backscattering mosaic by Joughin (2015).

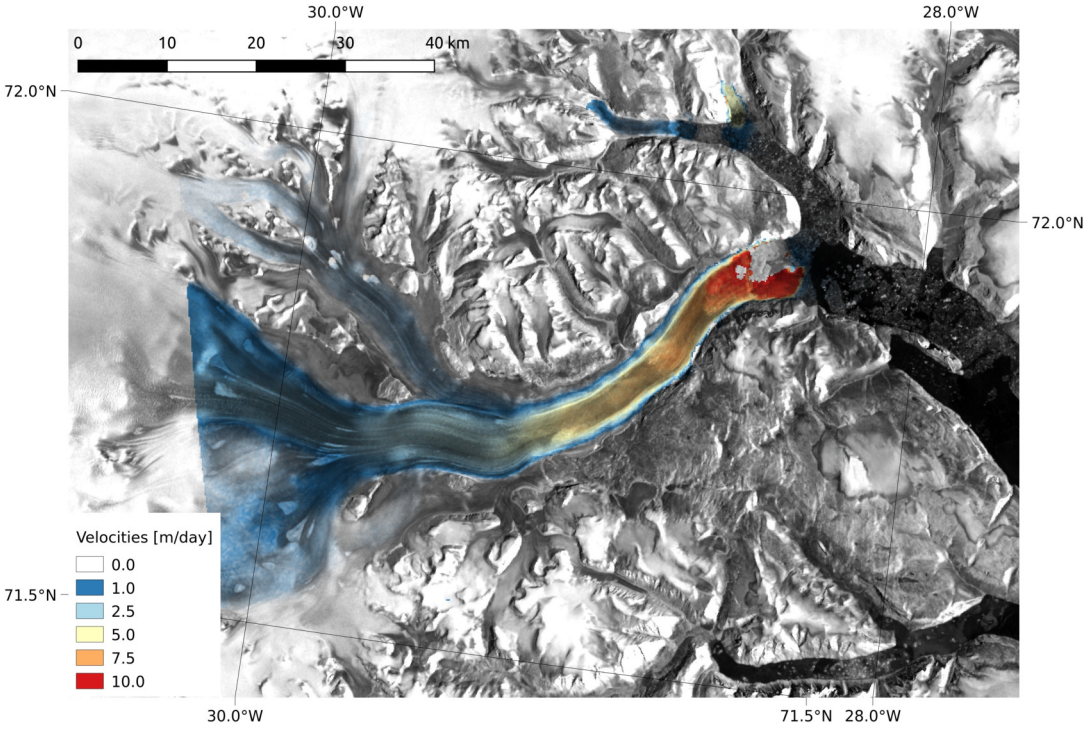

Figure 4.14: Ice velocity map of DJ overlaid on an amplitude backscattering mosaic by Joughin (2015).

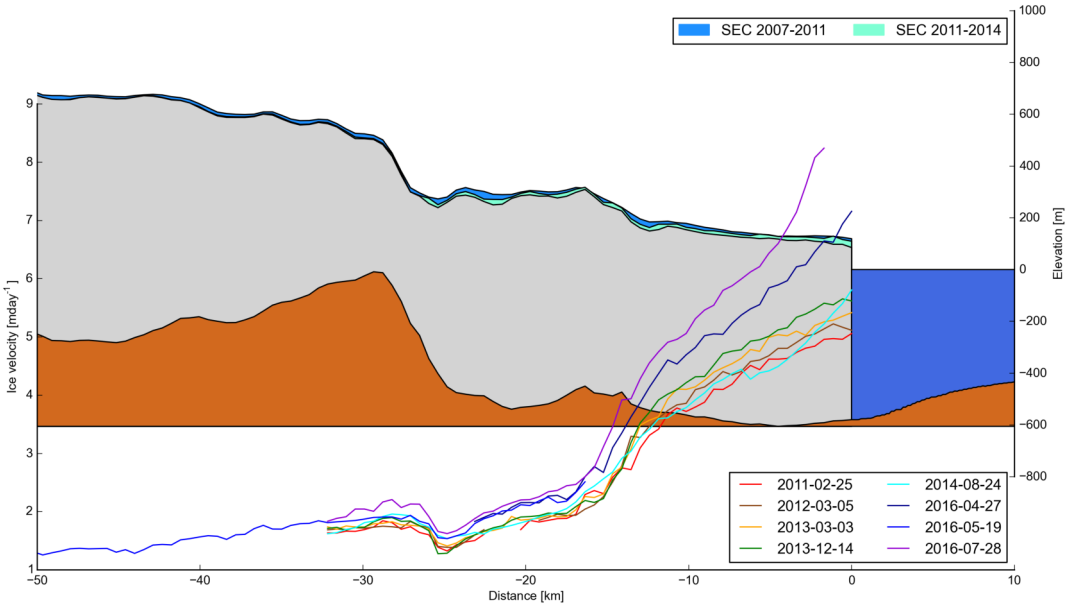

Figure 4.15: Ice velocity time-series along the central flow line of Zachariæ Isstrøm (ZI) between 2011 and 2016. The bed configuration shows the inland-facing bed slope from bedrock data published in Morlighem et al. (2017b) and the dynamic thinning is highlighted as a consequence of the increased ice export. Surface elevations are taken from a combination of photogrammetric measurements by Howat, Negrete, and Smith (2015) and TDM (see Section 4.5).

4.5 SURFACE ELEVATION CHANGE

Surface elevation change (SEC) was measured for ZI and 79North which are the two main outlet glaciers of NEGIS. The respective glacier catchments were derived in Section 4.1. Multiple DEMs were processed from bistatic TDM acquisitions which cover the glacier termini until approx. 50-100 km upstream of the glacier calving front or the grounding line at ZI and 79North. The acquisition dates for the used TDM scenes were in Dec./Jan. 2010/11 and Dec./Jan. 2013/14. The first acquisitions are termed as winter 2010 and the second as winter 2013 which roughly leads to a 3 year separation of all observed points (Table 4.3).

Table 4.3: Specifications for the TanDEM-X RawDEMs processed for ZI and 79North. All bistatic scenes were acquired for the initial generation of the TDM global DEM and therefore have optimal baselines for DEM generation. A – ascending, D – descending orbit direction.

		Acquisition Date	Acquisition Item Id	Scene Ids	Rel. orbit/ direction	Baseline	HoA	Inc. angle
Zachariæ Isstrøm & 79North	Master	2010-12-16	1009366	8	71/A	134.05	50.69	40.70
		2010-12-17	1009396	3,4,5	86/A	135.21	50.20	40.62
		2010-12-22	1009542	6,7,8	162/A	132.25	51.34	40.65
		2010-12-23	1009578	2,3,4	10/A	124.13	50.81	38.43
		2011-01-02	1009916	7,8,9	162/A	124.78	50.55	38.53
		2011-01-08	1010081	3,4,5	86/A	122.65	51.40	38.47
	Slave	2013-12-09	1169543	6,7	65/D	78.24	87.12	40.62
		2013-12-10	1169593	2,3	80/D	80.32	84.99	40.68
		2013-12-15	1169873	4,5,6	156/D	80.19	84.82	40.60
		2013-12-20	1170205	6,7	65/D	86.95	75.07	39.37
		2013-12-21	1170271	2,3	80/D	86.79	75.19	39.37
		2013-12-26	1170601	4,5,6	156/D	88.33	73.90	39.36
		2014-01-12	1171828	1,2,3	80/D	93.34	75.21	41.47
		2014-01-17	1172172	1,2,3,4	156/D	93.84	74.78	41.44

The InSAR processing of all bistatic acquisitions was performed with the Interferometric TDM Processor (ITP) developed at Deutsches Zentrum für Luft- und Raumfahrt (DLR) (Rossi et al., 2010). The resulting RawDEMs are continuous long stripes of DEM information framed into individual scenes of the same data take and thus are controlled by the same interferometric parameters (Table 4.3). For solving the 2π ambiguities during the absolute height determination a stereo-radargrammetric correction is implemented in ITP. Nevertheless, because of the short baselines of the bistatic formation, the elevation values can still be biased by 2π-multiples of the height of ambiguity h_a. Additional π-multiples of h_a can be introduced by the synchronisation link of the two satellites (Rizzoli et al., 2017b). Therefore the absolute elevation of each RawDEM was corrected by fine-tuning the absolute phase offset of the interferograms accordingly. Each RawDEM was vertically adjusted by Δh to a

reference DEM over ice free areas. The necessary modification for the absolute phase offset ϕ_{APO} is calculated as follows

$$\Delta\phi_{APO} = \frac{2\pi\Delta h}{h_a} \tag{4.1}$$

and the DEM generation from the unwrapped interferogram is repeated with the newly calculated $\phi_{APO} = \phi_{APO_{old}} + \Delta\phi_{APO}$. This method removes vertical offsets from the DEM and also corrects for horizontal range shifts introduced by the side looking geometry. The high geolocation accuracy below 1 m of the TDM data requires no further horizontal co-registration of the scenes (Abdel Jaber et al., 2019; Breit et al., 2010).

In order to estimate the vertical adjustment Δh that is needed to repeat the DEM generation with a newly calculated ϕ_{APO}, the median vertical offset of each RawDEM to the 12 m TDM global DEM (Rizzoli et al., 2017b) was measured over ice free terrain. Alternatively, if no areas with ice free terrain were found in the adjusted scene, previously corrected, overlapping RawDEMs were used for measuring Δh if the acquisition times were sufficiently close to each other to exclude changes in ice surface elevation. The locations of the ice free areas used for the vertical adjustment are shown in Figure 4.16. Areas with slopes higher than 15° were discarded during the calculation of the median offsets to the reference DEM.

The resulting absolutely height corrected RawDEMs were subsequently mosaicked to form elevation mosaics for winter 2010 and winter 2013. The mosaicking strategy was set in a way that minimises the days of seasonal separation between each pixel in the two mosaics. Afterwards, elevation changes seaward of the most retreated calving front or the grounding line were corrected. These areas include for example floating ice in the case of 79North or icebergs that were still present in the fjord of ZI and show up in the mosaicked DEM. Such elevations represent erroneous measurements when calculating mass loss from the volumetric changes. Therefore, the areas of retreat or advance at ZI or on the floating ice tongue at 79North were replaced with an elevation of 0 m in the slave and master mosaics, respectively. Note that this procedure ignores sub-aqueous ice volume changes. The resulting elevation mosaics have gapless measurements over both glacier termini. Phase unwrapping errors as well as ambiguous and missing measurements in areas of layover or radar shadow are restricted to smaller areas in the steep ice free terrain and were excluded from the vertical co-registration.

A simple difference of the elevation mosaics yields the absolute surface elevation change in the observed 3 years. Surface elevation change rate (SECR) maps (Figure 4.16) were calculated by scaling with the temporal separation of each pixel given by the individual scene acquisition times.

4.5.1 *Uncertainty of TDM surface elevation change rate*

Each RawDEM calculated by ITP is annotated with a height error map (HEM) which describes the standard error of the corresponding elevation value σ_h but does not include any systematic errors, which are discussed separately below. HEM is dependent on the interferometric error σ_ϕ which is estimated based on the number

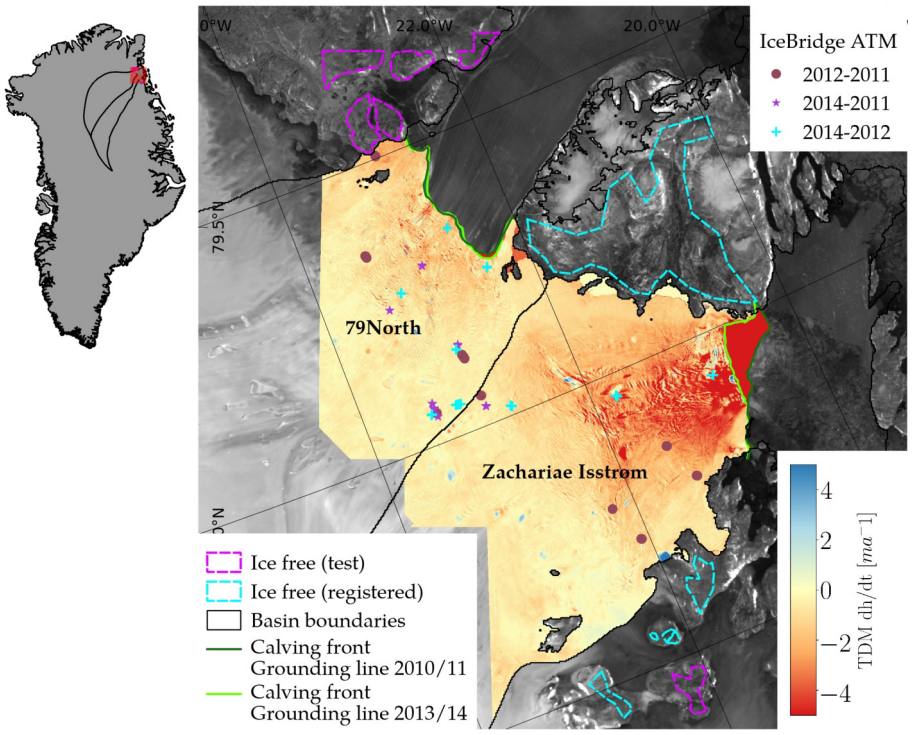

Figure 4.16: Surface elevation change rates for ZI and 79North measured by DEM differencing of TDM mosaics from winter 2010 and winter 2013. Ice free areas that have been used for vertical co-registration (blue) and uncertainty estimation (magenta) are superimposed on the TDM global DEM backscattering mosaic. Available locations of OIB Airborne Topographic Mapper (ATM) $\frac{dh}{dt}$ measurements are indicated for various sub-epochs. A detailed comparison to the OIB ATM data can be found in Appendix B.

of looks applied during interferometric processing and the interferometric coherence. σ_ϕ is scaled with the height of ambiguity (HoA) h_a (Rossi et al., 2010).

$$\sigma_h(x,y) = \sigma_\phi(x,y)\frac{h_a}{2\pi} \tag{4.2}$$

The random error of the TDM SECR σ_{HEM} is obtained by adding in quadrature the HEMs corresponding to the two RawDEMs used for differencing. When performing spatial averaging with conservative correlation distances, these interferometric errors are negligible compared to the other systematic error sources. Nevertheless, the estimated random error σ_{ran} was taken into account in the total uncertainty for TDM derived SECR (Equation 4.4). As in Abdel Jaber et al. (2019, Equation 7) the error of the mean elevation change rate in the observed area was calculated according to

$$\sigma_{ran} = \sqrt{\frac{\overline{\sigma^2_{HEM}}}{N}} \tag{4.3}$$

with N as the number of uncorrelated samples $N = \frac{9}{2}\frac{A}{A_c}$ of the correlated area $A_c = \pi d_c^2$ over a correlation distance d_c of 200 m. Since the total observed area $A \gg A_c$, N becomes very large and the random error of TDM SECR σ_{ran} is negligible.

The remaining errors in the surface elevation change map are a combination of the uncertainties in the vertical co-registration of the separate RawDEMs, phase jumps resulting from the phase unwrapping errors during the DEM generation and remaining biases due to SAR signal penetration. All these errors are of systematic nature and do not decrease during spatial averaging, thus they are dominating the total error budget. The following considerations about the errors were made:

1. The vertical bias between two differenced RawDEMs has been removed during vertical co-registration of all TDM RawDEMs. To estimate the uncertainty of this correction, the SECR was analysed over flat, ice free areas that were not used during vertical co-registration (magenta areas in Figure 4.16) where no elevation change is expected. Remaining biases between $-0.04\,\mathrm{m\,a^{-1}}$ and $0.13\,\mathrm{m\,a^{-1}}$ were measured and a value of $0.2\,\mathrm{m\,a^{-1}}$ was assumed as uncertainty in vertical co-registration for each pixel σ_{coreg}.

2. Interferometric phase jumps and the resulting biases in the surface elevation change map can occur due to phase unwrapping errors during DEM generation. They appear as constant offsets in the DEM difference measurements. Areas possibly affected by phase unwrapping errors, radar shadow and layover are provided in a layer by ITP (Rossi et al., 2010). The resulting DEMs have been checked for such cases and no occurrences have been found in the observed area.

3. Errors stemming from signal penetration into ice and snow could not be measured directly but are discussed in detail in Appendix B. Because only the differences in signal penetration affect the measured SEC, no uncertainties were assumed for areas with $\sigma^0 > -3\,\mathrm{dB}$ in both backscattering mosaics or where the absolute difference between the σ^0 values is $<1\,\mathrm{dB}$. In all other areas the uncertainty due to signal penetration was set to $0.1\,\mathrm{m\,a^{-1}}$. The mean SECR error in the entire TDM area due to signal penetration is termed $\sigma_{pen} = 0.1\,\mathrm{m\,a^{-1}}\,\frac{N_{pen}}{N_{all}}$. N_{pen} is the number of pixel for which penetration was taken into account and N_{all} denotes the overall number of pixels.

Finally the combined mean SECR uncertainty σ_{SECR} is calculated according to

$$\sigma^2_{SECR} = \sigma^2_{ran} + \sigma^2_{pen} + \sigma^2_{coreg} \tag{4.4}$$

A detailed discussion of the uncertainty budgets for vertical co-registration and signal penetration and their relation to mass change uncertainty can be found in Appendix B.

4.5.2 *Combination of surface elevation changes from TanDEM-X and CryoSat-2*

In addition to the InSAR measurements over the terminus, SEC measurements from CS-2 were utilised for the remaining unobserved parts of the drainage areas. Surface elevation change trends were observed for the same time period (Jan 2011 - Dec 2013) by project partners at the TU Dresden and are visualised in Figure 4.17. For a detailed description of the processing of this radar altimetry derived product the reader is referred to Appendix B.

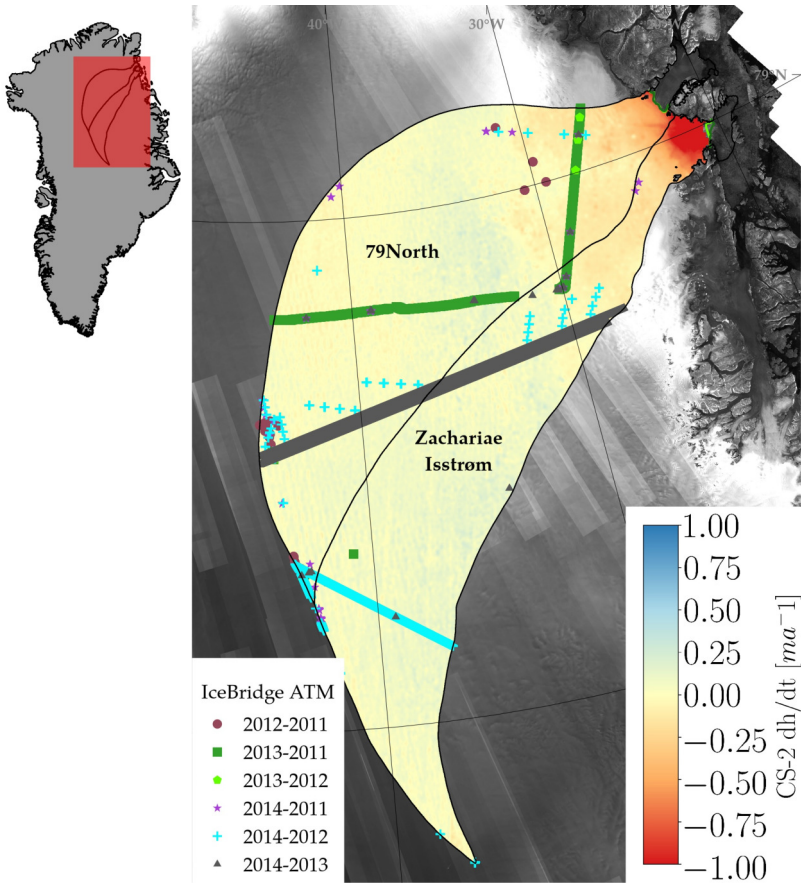

Figure 4.17: Surface elevation change rates for ZI and 79North measured by CryoSat-2 (CS-2) repeat altimetry analysis (RAA) from Jan. 2011 to Jan. 2014 and superimposed footprints of OIB ATM overflights. A detailed comparison to the OIB ATM data can be found in Appendix B. In the background, the TDM global DEM backscattering mosaic.

The TDM SECR over the glacier termini was combined with the CS-2 SECR of the entire drainage basins. While the TDM SECR is characterised by its high spatial resolution, CS-2 features a better vertical accuracy and reduced signal penetration after retracking of the radar waveform. TDM SECR is only available in the ablation zone approx. 50–100 km upstream of the glacier calving front or the grounding line and CS-2 SECR was replaced wherever TDM SECR is available. In the final combined dataset 2.6% of the basins are covered by TDM data and the remaining 97.4% by CS-2.

TDM and CS-2 SECR maps represent relative and independent measurements in which systematic biases have been removed during the processing. Therefore, both measurements were combined without correction. A difference map between the two SECR geophysical products is presented in Figure 4.18 and provides insight on how well the measured elevation change rates compare. As expected, the differences are high ($> -1\,\mathrm{m\,a^{-1}}$) for the areas close to the glacier front that experience high dynamic thinning and where the large footprint of the CS-2 SARIn mode of approx. $300 \times 1500\,\mathrm{m}$ leads to an underestimation of surface lowering (Mouginot et al., 2019; Wingham et al., 2006). Also, the small spatial variations in the TDM SECR map are

not captured in the CS-2 data. These locations include changes at the glacier margin, lake drainages or crevasse movement.

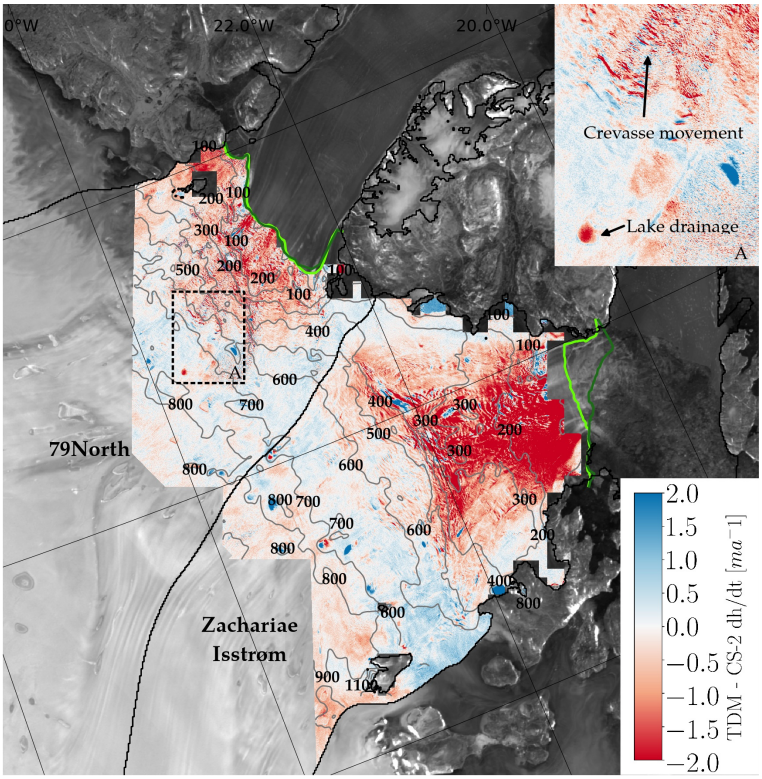

Figure 4.18: Difference of the TDM SECR map and the CS-2 SECR (TDM - CS-2) for the termini of ZI and 79North where measurements from both sensors overlap. Contour lines for absolute elevation are shown for the interpretation of Figure 4.19(a). Calving fronts (green lines) and basin delineation (black line) are as in Figure 4.16. Inset A highlights differences in elevation change because of lake drainage and crevasse movement which are only captured in the high resolution TDM dataset.

In order to study these differences in more detail, the altitude and slope dependence of the SECR differences was plotted for each basin and their combination (Figure 4.19). For elevations below 500 m a clear underestimation of CS-2 SECR is visible, while differences to the TDM SECR are slowly decreasing at higher elevations where the topography is flat. Especially for 79North, the areas above 600 m are located away from the complex topography in the ice free areas and the differences decrease on the flat terrain. Nevertheless, undulations in the difference map between TDM SECR and the CS-2 SECR are visible in Figure 4.18 and they are in the order of ± 0.2 m for elevations higher than 500 m (Figure 4.19(a)). This pattern is also visible in the slope dependence of the SECR difference (Figure 4.19(b)). The measured surface slope was averaged across 1×1 km patches from the 90 m TDM global DEM. Here, the differences decrease for shallower slopes until a difference of $-0.05\,\mathrm{m\,a^{-1}}$ for patches with a slope below 0.26°. For slopes steeper than 8°, higher differences were found, but these originate only from several measurements at the glacier margin and are not representative for the entire basin. The entire glaciated area observed by both sensors has a mean slope of 1.6°. The comparison shows that the two SECR maps

can be combined without correction as differences are within the expected accuracies of TDM DEM differencing (decimetre) and CS-2 radar altimetry (centimetre).

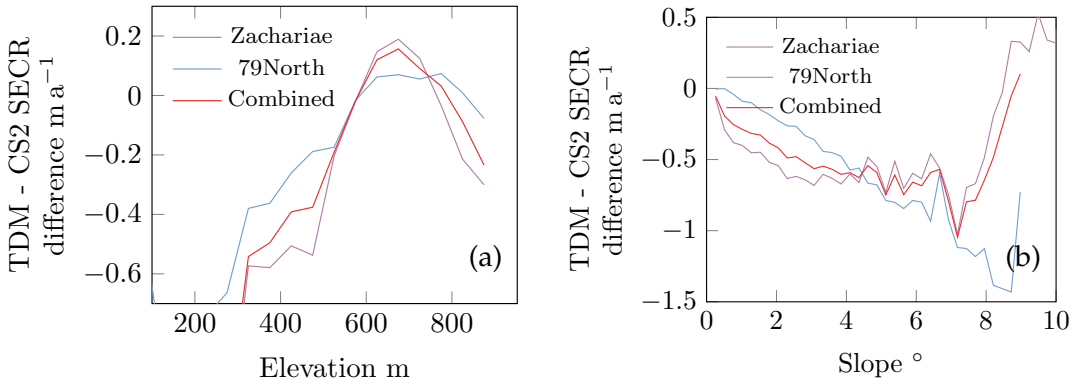

Figure 4.19: Differences of the TDM SECR map compared to the CS-2 SECR (TDM - CS-2) plotted over (a) elevation bins of 50 m and (b) surface slopes calculated from the TDM global DEM. The differences are calculated for the two basins separately and for all points combined.

Ice sheet SEC has been mainly derived with laser- or radar altimeters (Helm, Humbert, and Miller, 2014; Hurkmans et al., 2014; Khan et al., 2014) but on smaller ice bodies in the Andes or for small glacier catchments in the Antarctic Peninsula, volumetric measurements from InSAR and optical stereo DEM differencing have also been used to deliver SEC as input for the geodetic glacier mass balance (Abdel Jaber et al., 2019; Braun et al., 2019; Dussaillant et al., 2019; Rott et al., 2018). However, because of the sparse data availability of high resolution InSAR acquisitions, it has been challenging to cover entire glacier catchments of larger ice sheet outlet glaciers with timely, spatially distributed surface elevation measurements. This is why InSAR DEMs over the termini of large outlet glaciers have been mainly used for the interpretation of dynamic thinning and have not yet contributed to volumetric mass balance estimates of such glaciers (Joughin et al., 2019; Kehrl et al., 2017; Milillo et al., 2019) (Appendix D). The combined $\frac{dh}{dt}$ maps presented here cover 100% of the glaciated area of ZI and 79North which allows for the first time to apply SEC derived from TDM DEM differencing in a framework of volumetric mass balance measurements of large individual outlet glaciers on ice sheets (Section 4.6).

4.6 MASS BALANCE OF INDIVIDUAL OUTLET GLACIERS

The mass balance estimation of individual outlet glaciers can be performed with the glaciological parameters presented above. To assign the SECR measurements (Section 4.5) to the individual outlet glaciers, their catchments were calculated by a modified watershed algorithm from TDM global DEM elevations and Sentinel-1 velocity measurements in areas of fast ice flow (Section 4.1) (Krieger, Floricioiu, and Neckel, 2020). The seaward catchment extent was bounded by manually delineated calving fronts on the respective backscattering amplitude images and DInSAR grounding lines from Mar. 2011 and Jan. 2014 (Section 4.3). Integrating the SECR across the entire basin areas yields a volume change rate (VCR) for each observed outlet glacier. The measured volume loss cannot be entirely converted to mass loss because there

are other processes that result in volume change but that are not related to actual change in ice mass. Here firn compaction (FC) processes, glacial isostatic adjustment (GIA) and elastic bed uplift (EBU) were considered (Khan et al., 2015).

The present day vertical uplift resulting from GIA at the observed glacier termini is $<10\,\mathrm{mm\,a^{-1}}$ (Wake, Lecavalier, and Bevis, 2016). Its contribution to the VCR in the volume to mass conversion was accounted for by using modelled uplift rates $\frac{\Delta h_{GIA}}{\Delta t}$ from Peltier (2004) as they can be considered stable over a period of decades (Khan et al., 2015). EBU rates are more difficult to model and were only included in the uncertainty estimation as a relative fraction of the total Greenland volume change reported in Khan et al. (2015). Relative fractions for ZI (4.92%) and 79North (6.28%) were assigned based on the catchment areas compared to the total Greenland Ice Sheet (GrIS) area (Table 4.1). A potential underestimation of the relative fraction of EBU was ruled out by checking the spatial distribution of EBU rates in Khan et al. (2015) for anomalies of EBU uplift in either of the basins compared to the total distribution over Greenland. Regarding the firn compaction, the Institute for Marine and Atmospheric research Utrecht (IMAU)-firn densification model (FDM) v1.0 (Kuipers Munneke et al., 2015; Ligtenberg et al., 2018) was used to correct SECR in the study period based on firn processes. Following McMillan et al. (2016), compaction anomalies were calculated from compaction velocities which are modelled at a 10 day resolution by the IMAU-FDM. A linear trend was fitted to the observed time period T and compared to an assumed steady state between 1960 and 1979. The resulting rate of surface elevation change because of firn compaction $\frac{dh_{FC}}{dt}$ was subtracted from the measured SECR $\frac{dh}{dt}$ of both sensors.

Additionally, the mean density was calculated at the top layer of monthly modelled firn densities provided by the IMAU-FDM and a constant ice density of $917\,\mathrm{kg\,m^{-3}}$ was applied in the ablation zone. No additional areas of dynamic thinning were observed in the region outside the ablation zone and mean modelled firn densities between 2011-01-01 and 2013-12-31 were used. The resulting values for the ice or firn density are specified as ρ_{FDM}.

Finally, the pixel-wise mass change estimates are summed up over the glacier area $\mathcal{A}$ to form the total mass balance $\frac{dM}{dt}$ of the individual glacier catchments according to Equation 4.5.

$$\frac{dM}{dt} = \int_{\mathcal{A}} \left(\rho_{FDM} \left(\frac{dh}{dt} - \frac{dh_{FC}}{dt} - \frac{\Delta h_{GIA}}{\Delta t} \right) \right) d\mathcal{A} \tag{4.5}$$

Area distortions due to the polar-stereographic projection were corrected with a pixel-wise scaling factor $D(x,y)$ increasing with latitude ϕ away from the used standard parallel ϕ_s of 70°N (Hurkmans et al., 2014).

$$D(x,y) = \left(\frac{1+\sin(\phi)}{1+\sin(\phi_s)} \right)^2 \tag{4.6}$$

The final mass balance for both basins is reported in Table 4.4. Both glaciers display a negative mass balance. ZI has lost more than 3-times as much mass as its neighbouring glacier 79North. In this combination, 2.6% (ZI: 3.8%, 79North: 1.6%) of the basin was observed by TDM and the remaining 97.4% (ZI: 96.2%, 79North: 98.4%) by CS-2 resulting in an overall mass loss of $4.60 \pm 1.49\,\mathrm{Gt\,a^{-1}}$. If only CS-2

measurements were to be used for the entire basin without considering TDM data, the mass loss of NEGIS is only $1.87 \pm 1.35\,\mathrm{Gt\,a^{-1}}$. This difference highlights the difficulties of capturing the fast changing parts of the glacier termini accurately with conventional SARIn processing which underestimates mass loss by $2.73\,\mathrm{Gt\,a^{-1}}$ in this case.

Table 4.4: $\frac{dM}{dt}$ estimates from the TDM/CS-2 combination for ZI and 79North in the time period between 2011-01-01 and 2013-12-31 with and without contributions of the modelled firn compaction rate from the IMAU-FDM (Ligtenberg et al., 2018). CS-2 (contrib.) only states the mass change for the area that contributes to the combined estimate (TDM+CS-2). The total mass loss is calculated excluding subaqueous mass change. The ice discharge D is calculated from the difference between the volumetric mass balance and modelled SMB (RACMO2) (Noël et al., 2018). Units are $\mathrm{Gt\,a^{-1}}$.

Glacier name	TDM $\frac{dM}{dt}$	CS-2 (contrib.) $\frac{dM}{dt}$	TDM+CS-2 $\frac{dM}{dt}$	Subaqua. $\frac{dM}{dt}$	SMB	D
Including firn compaction:						
ZI	-5.37 ± 0.62	1.78 ± 0.96	-3.59 ± 1.15	-11.15 ± 0.03	8.95	-12.54
79North	-1.31 ± 0.34	0.30 ± 0.88	-1.01 ± 0.95	-0.05 ± 0.01	9.79	-10.80
Combined	-6.67 ± 0.71	2.08 ± 1.31	-4.60 ± 1.49	-11.20 ± 0.03	18.74	-23.34
No correction for firn compaction:						
ZI	-5.37 ± 0.62	1.11 ± 0.96	-4.27 ± 1.14	-11.15 ± 0.03	8.95	-13.21
79North	-1.31 ± 0.34	-0.39 ± 0.88	-1.70 ± 0.94	-0.05 ± 0.01	9.79	-11.50
Combined	-6.68 ± 0.71	0.71 ± 1.30	-5.97 ± 1.48	-11.20 ± 0.03	18.74	-24.71

Table 4.5: Mean TDM $\frac{dh}{dt}$ measurements and volume change rates $\frac{dV}{dt}$ for ZI and 79North in the time period between 2011-01-01 and 2013-12-31. Subaqueous volume changes are not considered in this table. A is the area observed by TDM and represents only a fraction A_{frac} of the entire catchments.

Glacier name	A [km²]	A_{frac} [%]	$\mu\frac{dh}{dt}$ [m a⁻¹]	$\frac{dV}{dt}$ [km³ a⁻¹]	$\frac{dM}{dt}$ [Gt a⁻¹]
ZI	3,221	3.8	-1.82 ± 0.55	-5.86 ± 0.67	-5.37 ± 0.62
79North	1,784	1.6	-0.80 ± 0.55	-1.43 ± 0.37	-1.31 ± 0.34
Combined	5,005	2.6	-2.62 ± 0.77	-7.29 ± 0.77	-6.67 ± 0.71

Close to the glacier terminus the glaciers are subject to similar atmospheric forcing and the small differences in SMB (Noël et al., 2018) cannot explain the high differences in SEC alone. Ice dynamics are therefore identified as the main driver of the pronounced thinning on ZI. It shows surface lowering of up to $10\,\mathrm{m\,a^{-1}}$ compared to approx. $3\,\mathrm{m\,a^{-1}}$ at 79North. Mean surface lowering and volume change rates are provided in Table 4.5 for areas observed by TDM.

While ZI's floating ice tongue has steadily disintegrated from 2002 to 2014 (Mouginot et al., 2015), 79North's ice tongue is thinning but still intact (Mayer et al., 2018). The loss of a buttressing ice tongue or ice shelf has been previously associated to subsequent speed-up and increased dynamic thinning (Rott et al., 2002). Moreover,

ZI has been rapidly retreating into the over 500 m deep fjord by an average of 2.1 km during the observed time period. Using bedrock elevations from a combination of ice-penetrating radar measurements and a mass conservation approach (Morlighem et al., 2017a). A substantial subaqueous mass loss of over 11 Gt a^{-1} was calculated assuming the glacier was grounded at both dates at the delineated calving front locations. Although subaqueous mass change does not have a direct impact on global sea level change, it still represents an important mass loss component that cannot be measured without calving front time-series on high to medium resolution imagery. In the case of ZI, the subaqueous ice mass loss is about 3-times larger than the total glacier mass loss. The floating ice tongue of 79North has been excluded from the analysis, because of the tidal influence on surface elevation changes. Based on a combination of seismic bed profiles, optical data and TDM DEMs, 79North's ice shelf has been shown to be losing mass through subglacial melting (Appendix C) (Mayer et al., 2018).

The error bounds reported in Table 4.4 are relatively large ranging between 0.34 Gt a^{-1} and 0.96 Gt a^{-1}. In the case of the TDM measurements, these are mainly attributed to the conservative systematic error budget for the vertical co-registration and signal penetration. For the CS-2 dataset the errors are large mostly because of the large spatial correlation distances over 500 km and 140 km. For a detailed description of the error estimation for the TDM and CS-2 SECR and the resulting mass change the reader is referred to Appendix B. The reported error budgets are approx. 1 Gt smaller in comparison to the volumetric mass balance estimates by Hurkmans et al. (2014) and similar to the uncertainties for the mass-budget method employed by Mouginot and Rignot (2019).

4.6.1 *Comparison with previous mass balance estimates*

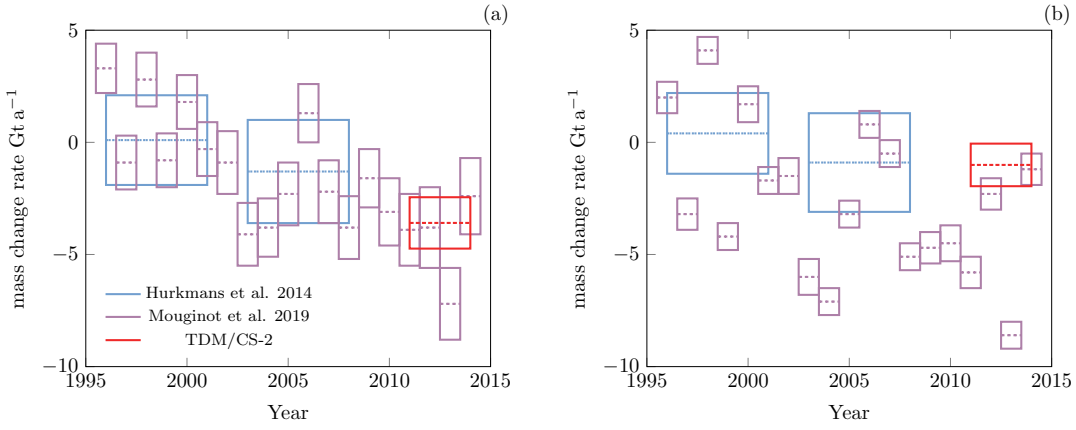

Figure 4.20: Comparison of mass balance results of the TDM/CS-2 combination with the volumetric approach of Hurkmans et al. (2014) and the mass-budget method by Mouginot et al. (2019) for individual glacier basins of (a) ZI and (b) 79North.

Hurkmans et al. (2014) report values for ZI of 0.1 ± 2.0 Gt a^{-1} for 1996 – 2001 and -1.3 ± 2.3 Gt a^{-1} for 2003 – 2008 that are derived from volumetric changes measured by ERS-1 and Ice, Cloud and land Elevation Satellite (ICESat). For the

same time periods 79North's mass balance was estimated to be $0.4 \pm 1.8\,\mathrm{Gt\,a^{-1}}$ and $-0.9 \pm 2.2\,\mathrm{Gt\,a^{-1}}$, respectively. These epochs are 7 and 14 years prior to my TDM/CS-2 results. The mass balance development shows increasing mass loss at ZI and a more stable situation at 79North which is partly balanced by larger mass gains in the accumulation zone. Another volumetric mass balance study in the same time period as the present experiment has been published by McMillan et al. (2016) stating a total mass loss of 8 Gt ($2.7\,\mathrm{Gt\,a^{-1}}$) restricted to the ZI terminus region. Mass balance was calculated for the entirety of Greenland but has not been partitioned to the individual glacier level for all glaciers. Finally, Mouginot et al. (2019) provide yearly estimates for individual glacier mass balances derived with the mass-budget method. Even though both glaciers have accelerated, the evolution of the mass balance for 79North is driven by year-to-year variations in SMB as ice discharge is only slightly increasing by approx. $1\,\mathrm{Gt\,a^{-1}}$ from 1995 – 2014 (Mouginot et al., 2019).

The comparisons of the different mass balance estimates are visualised in Figure 4.20. While results for ZI agree well, the volumetric mass losses reported at 79North are more than $2\,\mathrm{Gt\,a^{-1}}$ smaller than the average mass loss measured with the mass-budget method during the 3 years. The reason for the discrepancy on 79North together with a good agreement at ZI is difficult to determine but can be caused by inaccuracies in the SMB model, the ice thickness or ice velocity measurements in case of the mass-budget method whereas the geodetic method is influenced by the FDM model, the ice density assumptions, and the SEC measurements. As the CS-2 SECR shows less than $1\,\mathrm{cm\,a^{-1}}$ difference to validation OIB ATM points (Appendix B), possible error sources for the ice sheet interior are more likely for the density model or the firn compaction rates which dominate the volume change. For the region closer to the terminus an erroneous vertical co-registration of TDM is unlikely because of the good agreement on ZI which is comprised of the same RawDEM combination. A possible uncertainty in the vertical co-registration is accounted for in the TDM/CS-2 mass balance uncertainty but it cannot explain the difference of $2\,\mathrm{Gt\,a^{-1}}$. Nevertheless, biases in the SEC due to a difference in penetration cannot be ruled out and may be different for the two glaciers. Because of the discrepancies in the mass balance measurements on 79North, different CS-2 $\frac{dh}{dt}$ measurements were analysed with the developed methodology in Section 4.6.2.

The presented individual glacier mass balances are calculated with a novel combination of data provided by the TDM and CS-2 missions using the InSAR measurements in an established framework of volumetric mass balance measurements. On the one hand, the high resolution surface elevation change measurements with TDM provide spatial details over the glacier termini where greater dynamic variability is expected and CS-2 altimetry underestimates mass loss because of its large footprint (Mouginot et al., 2019). On the other hand, CS-2 Synthetic Aperture Interferometric Radar Altimeter (SIRAL) measurements are utilised for the ice sheet interior where InSAR data is not available and the better vertical accuracy of the altimeter is advantageous. I propose to repeat these synergistic mass balance measurements for other major outlet glaciers in Greenland or Antarctica complementary to budget-method derived mass balance observations for individual outlet glaciers in order to study discrepancies between the two methods and increase confidence in the reported mass balances of individual outlet glaciers on ice sheets.

4.6.2 *Comparison of different CS-2 processing strategies*

The mass loss for ZI and 79North was calculated with different CS-2 processing strategies. Thus the CS-2 SECR maps were exchanged for $\frac{dh}{dt}$ applying the processing of Helm, Humbert, and Miller (2014) (Alfred-Wegener-Institut (AWI)) and the methodology developed in Sections 4.5.2 and 4.6. These SECR maps are based on the same measurements from the CS-2 Level-1B (Baseline C) data archive between 2011 and 2014. Similar pre-processing as for the CS-2 SECR map from TU Dresden (Figure 4.17) was performed but different outlier elimination strategies were applied.

A total of 4 versions of CS-2 SECR maps are available which are described in Table 4.6. A more detailed description can be found in Appendix B.

Table 4.6: The analysed CS-2 processing strategies with 10% offset center of gravity (OCOG) (Schröder et al., 2019) and threshold first-maximum retracker (TFMRA) (Helm, Humbert, and Miller, 2014) retracker combinations for low resolution mode (LRM) and SARIn mode. The inclusion of the LeW and *bs* parameters in the regression is detailed in Appendix B.

	LRM retracking	SARIn retracking	LeW in LRM regression	*bs* in SARIn regression
TU Dresden	10% OCOG	TFMRA	✓	✓
AWI swath	TFMRA	swath	-	-
AWI TFMRA	TFMRA	TFMRA	-	-
AWI TFMRA + LeW	TFMRA	TFMRA	✓	-

Mass balance was calculated for the different CS-2 input datasets with and without replacing the SEC rates in the terminus region by TDM data. The resulting measurements are reported in Table 4.7 and Figure 4.21. In all results which use solely CS-2 SECR, remaining data gaps at the glacier margin have been interpolated by a nearest neighbour interpolation and values over the retreating terminus (between the two calving fronts in Figure 4.16) were discarded. Instead, the TDM-derived mass balance due to terminus retreat of $-0.45\,\mathrm{Gt\,a^{-1}}$ at ZI and $-0.01\,\mathrm{Gt\,a^{-1}}$ at 79North was taken into account to make the dataset comparable.

Table 4.7: $\frac{dM}{dt}$ estimates for ZI and 79North in the time period between 2011-01-01 and 2013-12-31 for different CS-2 processing strategies. Units are $\mathrm{Gt\,a^{-1}}$

CS-2 processing	TDM processing	Zachariæ Isstrøm	79North	Total mass loss
TU Dresden	✓	-3.59 ± 1.15	-1.01 ± 0.95	-4.60 ± 1.49
TU Dresden	-	-1.25 ± 1.00	-0.62 ± 0.91	-1.87 ± 1.35
AWI swath	✓	-4.07 ± 3.86	-1.85 ± 3.48	-5.92 ± 5.19
AWI swath	-	-3.33 ± 3.88	-1.73 ± 3.53	-5.05 ± 5.24
AWI TFMRA	✓	-3.30 ± 1.53	-0.54 ± 1.29	-3.84 ± 2.00
AWI TFMRA	-	-1.15 ± 1.45	-0.18 ± 1.29	-1.33 ± 1.94
AWI TFMRA + LeW	✓	-3.95 ± 1.60	-1.05 ± 1.36	-5.00 ± 2.10
AWI TFMRA + LeW	-	-1.81 ± 1.53	-0.67 ± 1.35	-2.48 ± 2.04

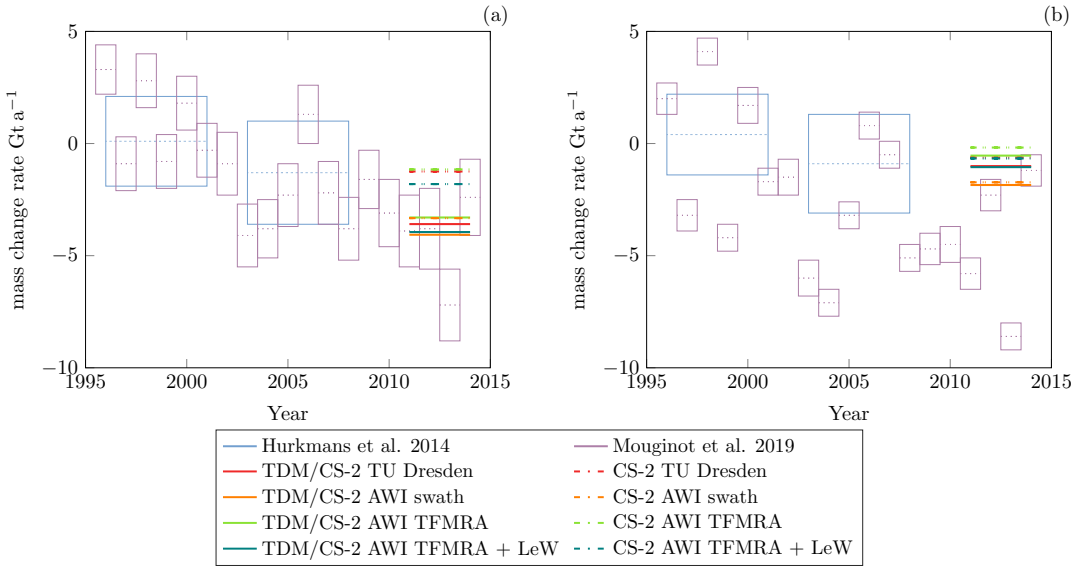

Figure 4.21: Mass loss from the volumetric approach of Hurkmans et al. (2014) and the mass-budget method by Mouginot et al. (2019) together with results from different combinations of surface elevation change measurements as in Table 4.7. The mass losses are partitioned to the individual glacier basins of (a) ZI and (b) 79North. For better visibility the mass losses are plotted without uncertainty bars.

Variations of volumetric mass balances between the four different CS-2 processing methodologies have been found even without including the SECR from TDM. A reason for this can be the 2012 melt event with a following change of the radar scattering scheme and the resulting decrease of LeW (Nilsson et al., 2015). Simonsen and Sørensen (2017) showed a correlation between LeW and elevation change and suggested to apply a LeW parameter within the regression for data products provided by ESA, which rely on OCOG (50%) or model fits. Nilsson et al. (2016) suggested a retracker (20%) to account for this effect. The AWI TFMRA (25%) introduced in Helm, Humbert, and Miller (2014) as well as a 10% OCOG by TU Dresden are accounting for the majority of melt effect but a residual contribution might be present. Therefore the LeW correlation was applied within the regression for LRM data by AWI and TU Dresden.

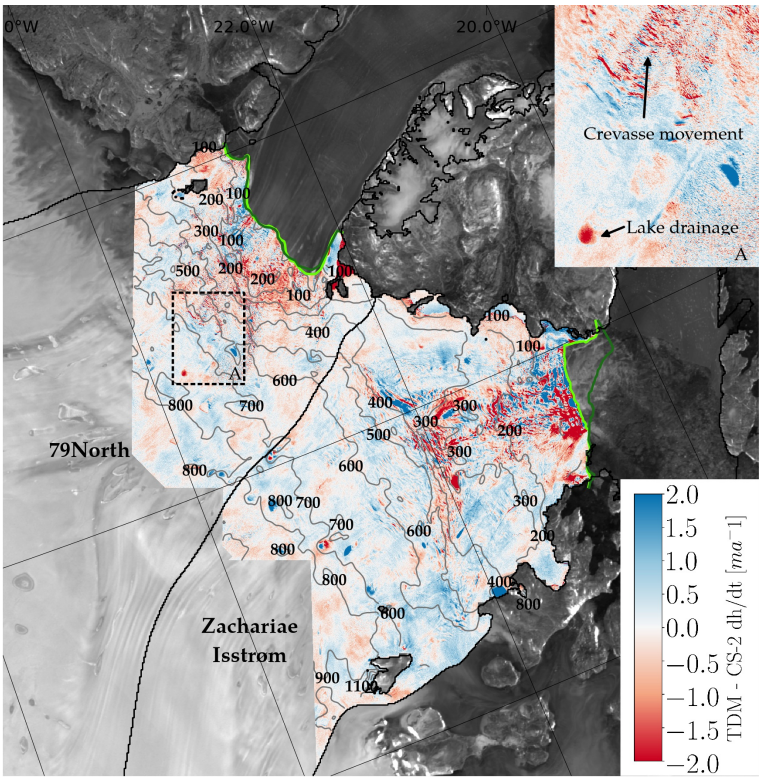

Figure 4.22: Differences of the TDM SECR map compared to the CS-2 surface elevation change trends from AWI swath processing (TDM - CS-2 AWI swath) for the terminus region of ZI and 79North where SEC from both sensors is available.

When focusing on the SECR differences between the four different CS-2 datasets and the TDM $\frac{dh}{dt}$ map, it was found that the CS-2 swath processing has the potential to improve CS-2 SECR over the fast changing parts of the glacier termini and shows smaller differences to TDM than conventional SARIn processing. However, the $\frac{dh}{dt}$ resulting from CS-2 swath processing is still underestimated compared to the TDM SECR. As a result, 0.87 Gt a^{-1} more mass loss is measured over ZI and 79North, by including TDM SECR in a combined analysis with AWI swath $\frac{dh}{dt}$. A difference of spatially distributed SECR (TDM - CS-2) is presented in Figure 4.22.

The overall accuracy of our mass loss estimates is difficult to assess due to the unavailability of ground truth data for individual Greenland glaciers. Gravimetry is not applicable to the individual glacier scale, thus the mass-budget method represents the only other independent remote sensing technique delivering mass balance estimates for single glaciers. Because of the lack of ground truth mass change data we focused on validating the SEC measurements instead. The derived SECRs from both sensors (TDM, CS-2) were compared in a detailed analysis over slope, elevation and surface roughness (Section 4.5.2). Additionally, IceBridge ATM $\frac{dh}{dt}$ measurements were analysed for available crossover locations (Appendix B). In the following the range of possible mass balance estimates is discussed with different CS-2 processing strategies, which furthers the understanding of the accuracy of the synergistic method.

Especially for ZI, a good agreement of the synergistic mass loss values is reached and the values vary from 3.30–4.07 Gt a^{-1} (Table 4.7). Whenever the TDM dataset was included, the derived mass loss increased for both glaciers (Figure 4.21). For the

SARIn strategies this gap to the synergistic mass balance (TDM included) varies from 2.14–2.34 Gt a^{-1} at ZI and 0.33–0.38 Gt a^{-1} at 79North. These constant offsets indicate that all SARIn strategies retrieve similar, but underestimated $\frac{dh}{dt}$ over the glacier termini. A special case is represented by CS-2 swath processing. Here, the inclusion of additional TDM data results only in 0.74 Gt a^{-1} and 0.12 Gt a^{-1} more mass loss at ZI and 79North respectively. The differences between TDM and CS-2-only processing are reduced in the CS-2 swath case compared to conventional SARIn processing. 79North shows surface lowering of up to 3 m a^{-1}, and CS-2 swath is almost able to capture these changes to the same extent as TDM. However, the higher SECRs of up to 10 m a^{-1} are not recorded in the CS-2 swath data. This indicates an increasing importance of the synergistic TDM/CS-2 mass loss for glaciers with high SECR.

The synergistic method is able to reduce the discrepancies of mass balance estimates between the mass-budget method and volumetric methods. All estimates which include TDM measurements perform closer to the values of Mouginot et al. (2019) than their CS-2-only counterparts (Figure 4.21). On 79North however, none of the above-presented volumetric techniques is able to reproduce the budget-derived mass loss (including and excluding TDM). Therefore I believe that the discharge at 79North is possibly overestimated. Complementary mass balance estimates from the geodetic method and the mass-budget method for the same time frame will provide the basis for investigating possible remaining error sources in either of the measurements.

4.7 BUOYANCY DERIVED ICE THICKNESS CHANGES AT THE FLOATING ICE TONGUE OF 79NORTH

Here I summarise the specific contributions to a thickness change study of the floating ice tongue of 79North published in Appendix C (Mayer et al., 2018). In this experiment, four bistatic InSAR acquisitions from TDM were used (Table 4.8). The data set is characterised by effective baselines ranging from 182 to 75 m with a corresponding HoA of 38 - 113 m. The InSAR DEMs cover about 30 × 50 km^2 and were generated using the ITP (Rossi et al., 2010).

Table 4.8: The TDM RawDEMs used for this study with the HoA of the bistatic InSAR acquisitions. The mean backscattering coefficient σ^0 was calculated over the floating ice tongue.

Date	Acquisition Item Id	Eff. Baseline [m]	HoA [m]	Relative orbit	Orbit direction	Incidence angle [°]	σ^0 [dB]
2011-01-08	1010081_5	121.32	51.96	86	A	38.43	-6.8
2012-11-14	1107756_7	182.41	38.08	162	A	41.42	-7.6
2014-12-08	1249997_6	75.73	112.64	86	A	38.60	-5.3
2016-09-28	1381068_11	87.07	74.89	86	A	39.33	-12.1

The co-authors of Appendix C were able to identify a grounding line feature which is visible on the ice shelf surface. Its horizontal displacements were related to thickness changes of the ice shelf with additional bedrock elevations from a seismic profile collected during a field experiment in 1998. By tracking the location of the

surface feature on time-series of optical imagery, ice thickness changes were inferred between 1998 and 2015 (Figure 4.23).

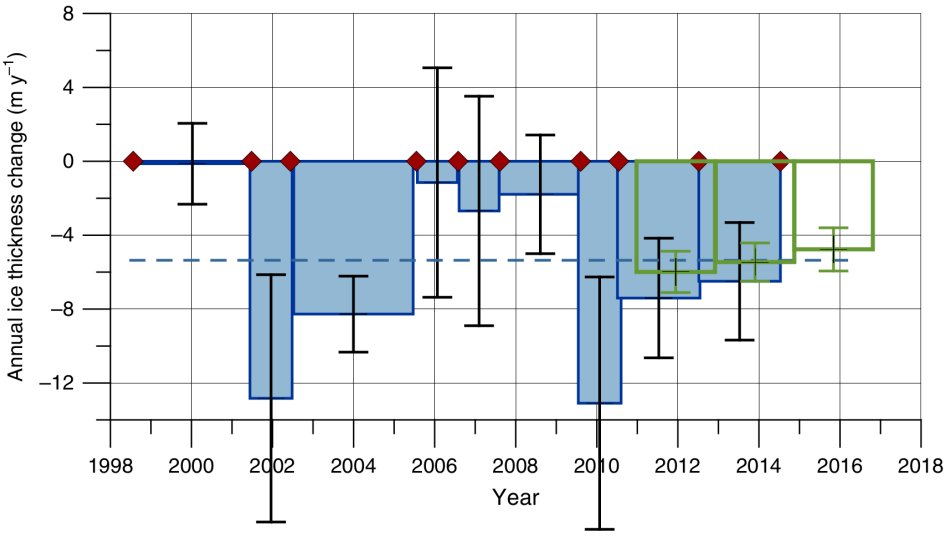

Figure 4.23: The time-series of ice shelf thickness changes on 79North taken from Appendix C. In blue are thickness changes derived from the persistent surface feature at the lateral grounding line. Green are the TDM derived thickness change rates. The plot is taken from (Mayer et al., 2018).

I contributed mean ice shelf thickness changes Δt retrieved from mean TDM surface elevation changes Δh over a freely floating part of the ice tongue. Archimedes' principle was applied with densities of ice $\rho_i = 900\,\mathrm{kg\,m^{-3}}$ and water $\rho_w = 1028\,\mathrm{kg\,m^{-3}}$.

$$\Delta t = \frac{\rho_w}{\rho_w - \rho_i} \Delta h \tag{4.7}$$

In order to estimate the errors for the thickness change rates, vertical co-registration errors of the scenes as well as the interferometric errors from the individual RawDEM HEM layers were taken into account. The HEM layer computed by ITP is based on interferometric coherence and geometrical considerations (Equation 4.2).

In the present study, which relies on TDM-TDM DEM differencing, the absolute height error was quantified separately for each scene by measuring offsets to the TDM global DEM over ice-free terrain. It is different for each RawDEM and during the DEM differencing the respective absolute height errors add up independently to absolute vertical co-registration error $SE_{\Delta z}$. The absolute horizontal error is negligible, because of the excellent geolocation accuracy of the ITP processor (Rizzoli et al., 2017b).

The interferometric errors were estimated from the HEM layers of the individual scenes. Mean HEM values ranging from 0.65 to 1.35 m were found over the floating part. They reduce to a statistical error $SE_{\Delta h}$ of the elevation difference after spatial averaging over the common area of the floating tongue in the tree DEM difference maps.

The absolute vertical co-registration error $SE_{\Delta z}$ and the interferometric error $SE_{\Delta h}$ are combined to the overall uncertainty of the elevation change $\epsilon_{\Delta h}$.

$$\epsilon_{\Delta h} = \sqrt{SE_{\Delta z}^2 + SE_{\Delta h}^2} \tag{4.8}$$

The uncertainties are reported in Table 4.9. Based on the time periods between the acquisitions, ice thickness change rates and their respective errors are reported from buoyancy calculations (Equation 4.7). Concerning additional errors from signal penetration, the backscattering coefficient σ^0 has been analysed over the floating ice tongue (Table 4.8). Values ranging from approx. −6 to −12 dB were found and a dominating surface scattering was assumed because of the crevassed and rough surface. The error of TDM-TDM surface elevation differences over the floating part of the ice tongue is therefore estimated to be 0.21 m (Table 4.9), which results in an error of the thickness change rate ϵ_{TCR} of less than ± 1.2 m.

Table 4.9: The TDM - TDM elevation difference statistics: $SE_{\Delta z}$ is the estimated error remaining after the vertical co-registration of each raw TDM scene to the TDM global DEM reference; $SE_{\Delta h}$ is the statistical error of the difference measurement over the floating ice tongue; $\epsilon_{\Delta h}$ is the overall uncertainty of the difference measurement; TCR is the buoyancy derived thickness change rate and ϵ_{TCR} denotes its error.

Date (Slave - Master)	Mean [m]	Std. deviation [m]	$SE_{\Delta h}$ [m]	$SE_{\Delta z}$ [m]	$\epsilon_{\Delta h}$ [m]	TCR [m a^{-1}]	ϵ_{TCR} [m a^{-1}]
2012-11-14 - 2011-01-08	-1.11	5.19	0.21	0.04	0.21	-5.99	1.12
2014-12-08 - 2012-11-14	-1.13	5.32	0.21	0.06	0.21	-5.46	1.04
2016-09-28 - 2014-12-08	-0.86	5.30	0.21	0.09	0.21	-4.77	1.17

The experiment described above provided a unique study case to investigate TDM DEM differencing over ice shelves to retrieve mean ice shelf thickness changes. The TDM results are in good agreement with independently inferred thickness changes based on the surface feature displacement. With the help of additional TDM results, the time-series of thickness changes was prolonged until Sept. 2016 (Figure 4.23).

Apart from DEM differencing, several other remote sensing techniques have been used for the detection of ice shelf thinning. Direct measurement of ice shelf thickness can be measured with ice penetrating radar by identifying the radar returns from the top and bottom of the ice shelf. With this technique Mouginot et al. (2015) found a bottom melt rate of 13.3 ± 4.0 m a^{-1} from 2000–2015 by analysing radar echograms 5 km downstream of the grounding line at 79North. Altimetry is another approach that also employs the buoyancy principle to measure thickness changes of ice shelves (Pritchard et al., 2012) and similar to the above-described TDM results, Shean et al. (2019) examined basal melt rates with high resolution DEM differencing for the Amundsen Sea Sector in Antarctica. At 79North this principle was applied to derive submarine melting of the ice tongue (Wilson, Straneo, and Heimbach, 2017) but none of the above mentioned techniques has examined the temporal variation of ice thickness changes at 79North. Contrary to the investigation of spatially distributed thickness changes, I calculated mean thickness change rates over a large area of the ice shelf in Table 4.9. Therefore, strain induced thickness change was not taken into account.

In Appendix C, in situ measurements to infer ice thickness changes are for the first time combined with buoyancy-derived thickness variation from InSAR DEM differencing. These independent measurements were used to cross-validate the respective techniques and to build up a long, densely sampled time-series. The temporal variation of ice shelf thickness changes in Greenland and Antarctica is poorly studied and long time-series of thickness changes are the exception (Shean et al., 2019). It remains important to continuously track the evolution of thickness changes at 79North's extensive ice tongue because a possible disintegration of the ice shelf through continuous thinning has extensive effects on the stability of the entire NEGIS sector (Choi et al., 2017; Mayer et al., 2018; Wilson, Straneo, and Heimbach, 2017).

5 CONCLUSION & OUTLOOK

This chapter presents the conclusions drawn from the thesis. Additionally an outlook on future research identifies key topics which need to be addressed in order to provide regular volumetric glacier mass balance measurements with TanDEM-X (TDM) and future synthetic aperture radar (SAR) and interferometric SAR (InSAR) missions.

5.1 SUMMARY AND CONCLUSION

The present thesis discusses the derivation of glaciological parameters with SAR and InSAR in the context of the Northeast Greenland Ice Sheet (GrIS). The mass balance of two major outlet glaciers in the region has been modelled with the geodetic method. For this purpose, ice velocity measurements and surface elevation time-series have been derived from TerraSAR-X (TSX) and TDM products and have been partitioned to newly defined drainage basins of the individual outlet glaciers. A previously defined framework for deriving geodetic glacier mass balance with TDM (Abdel Jaber, 2016) has been expanded to be applicable to large outlet glaciers on the ice sheet in a synergistic combination with radar altimeter measurements of CryoSat-2 (CS-2). The following conclusions can be drawn for the research objectives presented in Chapter 1

- Individual glacier catchments have been specified for the Northeast Greenland region. They allow a direct comparison of study results and lead to more robust estimates of glacier mass balances in case of their usage in other scientific works. Therefore I aim to include the catchments in the Randolph Glacier Inventory (RGI). In this work the basins are applied to partition surface elevation change measurements and outputs of a regional climate model for two outlet glaciers of the Northeast Greenland Ice Stream (NEGIS). The focus on individual ice sheet outlet glaciers therefore reduces the need for widespread coverage with TDM scenes as it would have been the case with previous, large-scale drainage sector delineations. The developed method uses objective decision criteria for tracing basin outlines by combining a digital elevation model (DEM) and velocity information with a modified watershed algorithm. A new partitioning of the Northeast Greenland region into 31 individual glacier catchments has been performed. As an independent, high accuracy data base for full validation of the results is lacking, quality assessment was supported by performing an inter-comparison with different input data combinations of DEMs and ice velocity products showing discrepancies of up to 16% in the extent of the catchment areas (Appendix A).
- Time-series of calving fronts have been delineated for Zachariæ Isstrøm (ZI) and Daugaard-Jensen (DJ). To this end, an algorithm has been developed that is able to delineate calving front locations of outlet glaciers on SAR amplitude backscattering images. Calving fronts are produced for Sentinel-1 and TSX data

by first enhancing edges and then using a path optimisation to find the best calving front candidate line. It is shown that results can even be obtained in conditions where the glacier front is crevassed and large icebergs are present in the fjord. Because the algorithm is not stable enough to be used without supervision and only two calving fronts are needed for the main objective of calculating the geodetic mass balance, these have been delineated by hand and the entire time-series of calving fronts is not used. Nevertheless, the developed algorithm has the potential to produce inter-annual and multi-annual calving fronts to investigate calving fluctuations for a large number of small and medium sized Greenland outlet glaciers of widths of 1–100 km. To date there exists no established method for the automatic derivation of glacier calving fronts on small dynamic outlet glaciers with high ice export rates (Appendix E).

- For Nioghalvfjersfjorden (79North) the grounding line was delineated applying differential InSAR (DInSAR) on repeat pass TSX and European Remote Sensing Satellite (ERS) acquisitions. Although the relatively fast flow velocity of 1400 m a^{-1} is causing some temporal decorrelation at the grounding zone, the high resolution of TSX and the short repeat cycle of ERS is able to retrieve a visible fringe belt over most of the grounding zone. The technique for delineating DInSAR grounding lines is not novel and has previously been applied at 79North by Mouginot et al. (2015). Here the data have been reprocessed and the grounding lines were additionally annotated with modelled tide levels for the time of the acquisitions. The grounding line positions for 79North were necessary for restricting the seaward extent of mass changes which contribute to global sea level rise. To this end, they were used for the main objective of modelling the geodetic mass balance of individual ice sheet outlet glaciers. In the time period between 2010 and 2014 there was no noticeable grounding line migration at 79North (Appendix B).

- Surface elevation change (SEC) for major outlet glaciers in the Northeast Greenland region has been processed from TDM data with the DEM differencing method. The used acquisitions from winter 2010 and 2013 show absolute thinning of some terminus regions of up to 30 m corresponding to thinning rates of >10 m a^{-1} near the terminus. For the DEM difference of a total of 14 RawDEMs, a scheme for vertical co-registration has been developed and penetration was accounted for in the uncertainty estimation based on σ^0 backscattering amplitude images. This result provided direct input for geodetic mass balance calculations (Appendix B).

- A novel combination of CS-2 and TDM elevation changes was developed to be used in the context of calculating the geodetic mass balance of individual outlet glaciers on ice sheets. This makes it feasible for InSAR DEM differencing to contribute to volumetric mass balance estimates on major outlet glaciers in Greenland and eliminates the need to cover the entire glacier basin with timely bistatic InSAR acquisitions. Furthermore, the two sensors complement each other with their different horizontal resolutions as well as vertical accuracies making it a superior approach compared to using data from a single sensor only. Utilising the entire time-series of elevation measurements together with the ability to retrack the radar waveform makes radar altimetry the better

suited method to measure the smaller elevation changes in the firn and snow covered areas of the ice sheet interior and allows a gapless observation of 100% of the drainage basin. Complementary, single-pass interferometry is able to resolve the higher resolution spatial details on the glacier terminus with larger surface elevation changes where surface scattering dominates because of the rough ice surface. Conventional CS-2 SARIn processing was found to underestimate mass loss in these areas. The range of mass balance results using different CS-2 processing strategies was investigated and the potential of CS-2 swath processing over the fast changing glacier termini was highlighted. Although CS-2 swath processing improves the detection of SEC over the fast changing glacier termini, $\frac{dh}{dt}$ is still underestimated compared to TDM DEM differencing (Appendix B).

- The mass balance for ZI has been $-3.59 \pm 1.15\,\mathrm{Gt\,a^{-1}}$ in the time between 2011-01-01 and 2013-12-31. Moreover, because of ZI's rapid retreat by an average of 2.1 km into the over 500 m deep fjord there has been substantial subaqueous mass loss of over $11\,\mathrm{Gt\,a^{-1}}$. Its neighbouring glacier 79North lost $1.01 \pm 0.95\,\mathrm{Gt\,a^{-1}}$ of ice mass during the same time period and its grounding line remained stable. These results were calculated by combining surface elevation change measurements from CS-2 and TDM with snow and firn characteristics provided by a regional climate model. It is the first time that volumetric measurements of TDM contribute directly to volumetric mass balance measurements of large ice sheet outlet glaciers with extensive basins after geodetic mass balances have already been calculated for smaller ice bodies like the Patagonian Ice Fields (Abdel Jaber et al., 2019) or glaciers on the Antarctic Peninsula (Rott et al., 2018). The developed method provides an alternative to the already established mass-budget method which has been previously employed for individual outlet glaciers in Greenland. It presents the only other source of mass balance estimates for the same time period (Mouginot et al., 2019). For 79North, the volumetric mass losses reported here are more than 2 Gt smaller than the ones measured with the mass-budget method, while results for ZI agree well. The exact origin for this discrepancy could not be identified but while the mass-budget method relies on the accuracy of the modelled surface mass balance (SMB) and the ice discharge at the glacier grounding line, volumetric mass balance measurements result from spatially distributed SEC measurements and only use modelled firn densities. Contrary to gravimetric measurements, both methods can be applied on the small scale of individual outlet glaciers and it is of benefit to monitor the mass balance regularly with both methods to investigate both the dynamic process of ice mass loss as well as its spatial distribution (Appendix B).

- A detailed study of the floating tongue of 79North revealed mean thinning rates of $-5.3\,\mathrm{m\,a^{-1}}$ between 1998 and 2016. Within this work, a time-series of bistatic TDM to TDM differences was used to calculate buoyancy derived thickness changes of the floating ice tongue. The study attributed the thickness changes to an increased amount of warmer ocean water in the fjord as ice dynamics and atmospheric forcing cannot fully explain the observed magnitude of thickness change. This experiment provided the rare opportunity to infer thickness changes from a visible surface feature at the lateral grounding line by utilising its time-variable location in combination with in situ bedrock measurements

collected by the co-authors. The buoyancy derived TDM thickness change measurements are in good agreement ($< 1.5\,\mathrm{m\,a^{-1}}$) with these inferred changes. The time-series of ice shelf thickness changes was prolonged until 2016 by using additional TDM data and provided an unprecedented temporal sampling of thickness change variations of 79North's floating ice tongue (Appendix C).

5.2 OUTLOOK

The methodology presented in this thesis builds towards a framework for regularly observing volumetric ice sheet mass balances of individual outlet glaciers with the help of high resolution bistatic InSAR. In order to fully achieve a regular observation of volumetric ice sheet mass balances the following topics have to be further investigated.

5.2.1 *Drainage basins for Greenland and Antarctica*

At the time of writing, the only complete delineation of glacier catchments in Greenland is provided by Mouginot and Rignot (2019) although a detailed description of the methodology used to derive the glacier catchments is missing for these results. The approach detailed in Appendix A has the potential to produce outlines of drainage basins for entire Greenland and Antarctica while at the same time providing a fully traceable methodology. As ice sheet velocities are known to experience seasonal or multiyear variations, there is a possibility that also drainage areas are affected by such changes. Therefore, repeated investigations of glacier drainage systems should be carried out in the future with multi-temporal velocity datasets and accurate, high-resolution DEMs. Moreover, the procedure is also directly applicable on smaller scales for the delineation of ice divides between outlet glaciers of ice caps and ice fields. It can be used to refine and update glacier inventories like the RGI, e.g. by adding separate basins for each glacier on continuous ice bodies (RGI Consortium, 2017).

5.2.2 *Regular volumetric mass balance from TanDEM-X and CryoSat-2*

Appendix B developed a framework to measure volumetric mass balances from a combination of TDM and CS-2 measurements at the example of two major outlet glaciers in Northeast Greenland. The surface elevation change rate (SECR) from CS-2 is already regularly produced within the ESA Greenland Ice Sheet Climate Change Initiative (CCI) (Simonsen and Sørensen, 2017), however consistent observations using high resolution InSAR DEM differencing over the various outlet glacier termini are missing. Mass balance monitoring of Greenland's major outlet glaciers with the geodetic method would complement results by the mass-budget method, that are already observed over four decades for all outlet glaciers of the GrIS (Mouginot et al., 2019). With respect to possible new bistatic InSAR missions like TanDEM-L, an operational framework for InSAR DEM differencing becomes more important.

5.2.3 *Vertical co-registration and penetration*

The largest sources for error in the TDM-TDM volumetric mass balance measurements are the systematic errors stemming from the vertical co-registration and signal penetration. Because InSAR DEMs do not measure absolute elevation directly, the choice of a suitable reference point has always been important and difficult to achieve in some glaciated areas where the surface cannot be considered stable over time. In Dec. 2018 the laser altimeter Ice, Cloud and land Elevation Satellite (ICESat)-2 has begun operation and its small footprint paired with the laser reflections at the surface provide new possibilities to correct vertical offsets in TDM DEMs (Abdalati et al., 2010). The high revisit time of the satellite compared to the sparse flight lines of Operation IceBridge (OIB) provides new opportunities to further the operational vertical co-registration especially in areas where no ice free areas can be found within the scene. A correction for the elevation bias due to signal penetration is possible because the laser signal does not penetrate into ice and snow layers. This becomes especially important for possible future InSAR missions like TanDEM-L where the larger wavelength will magnify the effect of signal penetration (Krieger et al., 2009).

5.2.4 *Derivation of the calving front and the grounding line with deep learning methods*

Both for the delineation of the glacier calving front and for digitising the grounding line, the input images are already automatically processed and widely available. In case of the calving front these are just regular SAR amplitude backscattering images. For the grounding line some interferometric processing is needed which is already automated. Therefore, the only obstacle for the regular monitoring of the grounding line and the calving front of a great number of outlet glaciers is the time consuming manual delineation of the respective line. In Appendix E I worked towards the algorithmic detection of the calving front with classical computer vision methods. Recently deep neural networks gained widespread popularity in many imaging applications which opens up the possibility to find better edge candidates similar to Mohajerani et al. (2019) or to perform a pixel wise segmentation of the land cover at front line (Baumhoer et al., 2019). This would lead the way to a real, widespread monitoring of grounding lines and calving fronts for the ice sheets.

BIBLIOGRAPHY

Abdalati, W. et al. (2010). "The ICESat-2 Laser Altimetry Mission." In: *Proceedings of the IEEE* 98.5, pp. 735–751. ISSN: 0018-9219, 1558-2256. DOI: 10.1109/JPROC.2009.2034765.

Abdel Jaber, W. (2016). "Derivation of Mass Balance and Surface Velocity of Glaciers by Means of High Resolution Synthetic Aperture Radar: Applicationto the Patagonian Icefields and Antarctica." PhD Thesis. Technische Universität München. URL: http://elib.dlr.de/109075/.

Abdel Jaber, W., H. Rott, D. Floricioiu, J. Wuite, and N. Miranda (2019). "Heterogeneous Spatial and Temporal Pattern of Surface Elevation Change and Mass Balance of the Patagonian Ice Fields between 2000 and 2016." In: *The Cryosphere* 13.9, pp. 2511–2535. ISSN: 1994-0416. DOI: https://doi.org/10.5194/tc-13-2511-2019.

Abdullahi, S., B. Wessel, T. Leichtle, M. Huber, C. Wohlfart, and A. Roth (2018). "Investigation of Tandem-X Penetration Depth Over the Greenland Ice Sheet." In: *IGARSS 2018 - 2018 IEEE International Geoscience and Remote Sensing Symposium*. IGARSS 2018 - 2018 IEEE International Geoscience and Remote Sensing Symposium, pp. 1336–1339. DOI: 10.1109/IGARSS.2018.8518930.

Ahlenius, H. (2007). Published: UNEP/GRID-Arenda. URL: http://www.grida.no/resources/5222 (visited on 10/29/2019).

Alley, R. B., M. K. Spencer, and S. Anandakrishnan (2007). "Ice-Sheet Mass Balance: Assessment, Attribution and Prognosis." In: *Annals of Glaciology* 46, pp. 1–7. ISSN: 0260-3055, 1727-5644. DOI: 10.3189/172756407782871738.

Angelis, H. D. and P. Skvarca (2003). "Glacier Surge After Ice Shelf Collapse." In: *Science* 299.5612, pp. 1560–1562. ISSN: 0036-8075, 1095-9203. DOI: 10.1126/science.1077987.

Bamber, J. L. (1994). "A Digital Elevation Model of the Antarctic Ice Sheet Derived from ERS-1 Altimeter Data and Comparison with Terrestrial Measurements." In: *Annals of Glaciology* 20. ed, pp. 48–54. ISSN: 0260-3055, 1727-5644. DOI: 10.3189/1994AoG20-1-48-54.

Bamler, R. and M. Eineder (2005). "Accuracy of Differential Shift Estimation by Correlation and Split-Bandwidth Interferometry for Wideband and Delta-k SAR Systems." In: *IEEE Geoscience and Remote Sensing Letters* 2.2, pp. 151–155. ISSN: 1545-598X. DOI: 10.1109/LGRS.2004.843203.

Barnes, R., C. Lehman, and D. Mulla (2014). "Priority-Flood: An Optimal Depression-Filling and Watershed-Labeling Algorithm for Digital Elevation Models." In: *Computers & Geosciences* 62, pp. 117–127. ISSN: 0098-3004. DOI: 10.1016/j.cageo.2013.04.024.

Baumhoer, C. A., A. J. Dietz, S. Dech, and C. Kuenzer (2018). "Remote Sensing of Antarctic Glacier and Ice-Shelf Front Dynamics—A Review." In: *Remote Sensing* 10.9, p. 1445. DOI: 10.3390/rs10091445.

Baumhoer, C. A., A. J. Dietz, C. Kneisel, and C. Kuenzer (2019). "Automated Extraction of Antarctic Glacier and Ice Shelf Fronts from Sentinel-1 Imagery Using Deep Learning." In: *Remote Sensing* 11.21, p. 2529. DOI: 10.3390/rs11212529.

Bechor, N. B. D. and H. A. Zebker (2006). "Measuring Two-Dimensional Movements Using a Single InSAR Pair." In: *Geophysical Research Letters* 33.16. ISSN: 1944-8007. DOI: 10.1029/2006GL026883.

Benson, C. S. (1962). *STRATIGRAPHIC STUDIES IN THE SNOW AND FIRN OF THE GREENLAND ICE SHEET*. RR70. COLD REGIONS RESEARCH AND ENGINEERING LAB HANOVER N H. URL: https://apps.dtic.mil/docs/citations/AD0288219.

Berthier, E., H. Vadon, D. Baratoux, Y. Arnaud, C. Vincent, K. L. Feigl, F. Rémy, and B. Legrésy (2005). "Surface Motion of Mountain Glaciers Derived from Satellite Optical Imagery." In: *Remote Sensing of Environment* 95.1, pp. 14–28. ISSN: 0034-4257. DOI: 10.1016/j.rse.2004.11.005.

Berthier, E. et al. (2014). "Glacier Topography and Elevation Changes Derived from Pléiades Sub-Meter Stereo Images." In: *The Cryosphere* 8.6, pp. 2275–2291. ISSN: 1994-0416. DOI: https://doi.org/10.5194/tc-8-2275-2014.

Beucher, S. et al. (1992). "The Watershed Transformation Applied to Image Segmentation." In: *SCANNING MICROSCOPY-SUPPLEMENT-*, pp. 299–299.

Bindschadler, R. A. (1998). "Monitoring Ice Sheet Behavior from Space." In: *Reviews of Geophysics* 36.1, pp. 79–104. ISSN: 1944-9208. DOI: 10.1029/97RG02669.

Bindschadler, R. A., K. C. Jezek, and J. Crawford (1987). "Glaciological Investigations Using the Synthetic Aperture Radar Imaging System." In: *Annals of Glaciology* 9. ed, pp. 11–19. ISSN: 0260-3055, 1727-5644. DOI: 10.3189/S0260305500200694.

Bindschadler, R. A. et al. (2011). "Getting around Antarctica: New High-Resolution Mappings of the Grounded and Freely-Floating Boundaries of the Antarctic Ice Sheet Created for the International Polar Year." In: *The Cryosphere* 5.3, pp. 569–588. ISSN: 1994-0416. DOI: https://doi.org/10.5194/tc-5-569-2011.

Braun, M. H., P. Malz, C. Sommer, D. Farías-Barahona, T. Sauter, G. Casassa, A. Soruco, P. Skvarca, and T. C. Seehaus (2019). "Constraining Glacier Elevation and Mass Changes in South America." In: *Nature Climate Change* 9.2, pp. 130–136. ISSN: 1758-6798. DOI: 10.1038/s41558-018-0375-7.

Breit, H., T. Fritz, U. Balss, M. Lachaise, A. Niedermeier, and M. Vonavka (2010). "TerraSAR-X SAR Processing and Products." In: *IEEE Transactions on Geoscience and Remote Sensing* 48.2, pp. 727–740. ISSN: 0196-2892, 1558-0644. DOI: 10.1109/TGRS.2009.2035497.

Broeke, M. R. van den, J. L. Bamber, J. Ettema, E. Rignot, E. J. O. Schrama, W. J. van de Berg, E. van Meijgaard, I. Velicogna, and B. Wouters (2009). "Partitioning Recent Greenland Mass Loss." In: *Science* 326.5955, pp. 984–986. ISSN: 0036-8075, 1095-9203. DOI: 10.1126/science.1178176.

Brooks, R. L., W. J. Campbell, R. O. Ramseier, H. R. Stanley, and H. J. Zwally (1978). "Ice Sheet Topography by Satellite Altimetry." In: *Nature* 274.5671, pp. 539–543. ISSN: 1476-4687. DOI: 10.1038/274539a0.

Brunt, K. M., H. A. Fricker, L. Padman, T. A. Scambos, and S. O'Neel (2010). "Mapping the Grounding Zone of the Ross Ice Shelf, Antarctica, Using ICESat Laser Altimetry." In: *Annals of Glaciology* 51.55. ed, pp. 71–79. ISSN: 0260-3055, 1727-5644. DOI: 10.3189/172756410791392790.

Cabral, B. and L. C. Leedom (1993). *Imaging Vector Fields Using Line Integral Convolution*. UCRL-JC-112935; CONF-9208240-1. Lawrence Livermore National Lab., CA (United States). URL: https://www.osti.gov/biblio/10185520.

Choi, Y., M. Morlighem, E. Rignot, J. Mouginot, and M. Wood (2017). "Modeling the Response of Nioghalvfjerdsfjorden and Zachariae Isstrøm Glaciers, Greenland,

to Ocean Forcing Over the Next Century." In: *Geophysical Research Letters* 44.21, pp. 11,071–11,079. ISSN: 1944-8007. DOI: 10.1002/2017GL075174.

Cogley, J. G. (2003). *GGHYDRO-Global Hydrographic Data, Release 2.3. 1 Trent Technical Note 2003-1*.

Csatho, B. M., A. F. Schenk, C. J. van der Veen, G. Babonis, K. Duncan, S. Rezvanbehbahani, M. R. van den Broeke, S. B. Simonsen, S. Nagarajan, and J. H. van Angelen (2014). "Laser Altimetry Reveals Complex Pattern of Greenland Ice Sheet Dynamics." In: *Proceedings of the National Academy of Sciences* 111.52, pp. 18478–18483. ISSN: 0027-8424, 1091-6490. DOI: 10.1073/pnas.1411680112.

Dall, J. (2007). "InSAR Elevation Bias Caused by Penetration Into Uniform Volumes." In: *IEEE Transactions on Geoscience and Remote Sensing* 45.7, pp. 2319–2324. ISSN: 0196-2892, 1558-0644. DOI: 10.1109/TGRS.2007.896613.

Dall, J., K. P. Papathanassiou, and H. Skriver (2004). "Polarimetric SAR Interferometry Applied to Land Ice: Modeling." In: *Proceedings of the EUSAR 2004 Conference*. 5th European Conference on Synthetic Aperture Radar. Ulm, Germany, pp. 247–250.

Dall, J., S. N. Madsen, K. Keller, and R. Forsberg (2001). "Topography and Penetration of the Greenland Ice Sheet Measured with Airborne SAR Interferometry." In: *Geophysical Research Letters* 28.9, pp. 1703–1706. ISSN: 1944-8007. DOI: 10.1029/2000GL011787.

Dawson, G. J. and J. L. Bamber (2017). "Antarctic Grounding Line Mapping From CryoSat-2 Radar Altimetry." In: *Geophysical Research Letters* 44.23, pp. 11,886–11,893. ISSN: 1944-8007. DOI: 10.1002/2017GL075589.

Debella-Gilo, M. and A. Kääb (2012). "Measurement of Surface Displacement and Deformation of Mass Movements Using Least Squares Matching of Repeat High Resolution Satellite and Aerial Images." In: *Remote Sensing* 4.1, pp. 43–67. DOI: 10.3390/rs4010043.

Dirscherl, M., A. J. Dietz, S. Dech, and C. Kuenzer (2020). "Remote Sensing of Ice Motion in Antarctica – A Review." In: *Remote Sensing of Environment* 237, p. 111595. ISSN: 0034-4257. DOI: 10.1016/j.rse.2019.111595.

Dussaillant, I., E. Berthier, F. Brun, M. Masiokas, R. Hugonnet, V. Favier, A. Rabatel, P. Pitte, and L. Ruiz (2019). "Two Decades of Glacier Mass Loss along the Andes." In: *Nature Geoscience* 12.10, pp. 802–808. ISSN: 1752-0908. DOI: 10.1038/s41561-019-0432-5.

Dussaillant, I., E. Berthier, and F. Brun (2018). "Geodetic Mass Balance of the Northern Patagonian Icefield from 2000 to 2012 Using Two Independent Methods." In: *Frontiers in Earth Science* 6. ISSN: 2296-6463. DOI: 10.3389/feart.2018.00008.

Dwyer, J. L. (1995). "Mapping Tide-Water Glacier Dynamics in East Greenland Using Landsat Data." In: *Journal of Glaciology* 41.139. ed, pp. 584–595. ISSN: 0022-1430, 1727-5652. DOI: 10.3189/S0022143000034900.

Enderlin, E. M., I. M. Howat, S. Jeong, M.-J. Noh, J. H. van Angelen, and M. R. van den Broeke (2014). "An Improved Mass Budget for the Greenland Ice Sheet." In: *Geophysical Research Letters* 41.3, pp. 866–872. ISSN: 1944-8007. DOI: 10.1002/2013GL059010.

Fahnestock, M. A., R. A. Bindschadler, R. Kwok, and K. C. Jezek (1993). "Greenland Ice Sheet Surface Properties and Ice Dynamics from ERS-1 SAR Imagery." In: *Science* 262.5139, pp. 1530–1534. ISSN: 0036-8075, 1095-9203. DOI: 10.1126/science.262.5139.1530.

Felikson, D. et al. (2017). "Inland Thinning on the Greenland Ice Sheet Controlled by Outlet Glacier Geometry." In: *Nature Geoscience* 10.5, pp. 366–369. ISSN: 1752-0908. DOI: 10.1038/ngeo2934.

Fischer, G., K. P. Papathanassiou, and I. Hajnsek (2019). "Modeling Multifrequency Pol-InSAR Data From the Percolation Zone of the Greenland Ice Sheet." In: *IEEE Transactions on Geoscience and Remote Sensing* 57.4, pp. 1963–1976. ISSN: 0196-2892, 1558-0644. DOI: 10.1109/TGRS.2018.2870301.

Fischer, G., G. Parrella, K. P. Papathanassiou, and I. Hajnsek (2017). "Sensitivity of Polarimetric SAR Interferometry Data to Different Vertical Subsurface Structures of the Greenland Ice Sheet." In: *2017 IEEE International Geoscience and Remote Sensing Symposium (IGARSS)*. 2017 IEEE International Geoscience and Remote Sensing Symposium (IGARSS), pp. 3581–3584. DOI: 10.1109/IGARSS.2017.8127774.

Fjortoft, R., A. Lopes, P. Marthon, and E. Cubero-Castan (1998). "An Optimal Multiedge Detector for SAR Image Segmentation." In: *IEEE Transactions on Geoscience and Remote Sensing* 36.3, pp. 793–802. ISSN: 0196-2892, 1558-0644. DOI: 10.1109/36.673672.

GEBCO Compilation Group (2019). *GEBCO 2019 Grid*. DOI: 10.5285/836f016a-33be-6ddc-e053-6c86abc0788e.

GLIMS and NSIDC (2005, updated 2018). *Global Land Ice Measurements from Space Glacier Database.* DOI: https://doi.org/10.7265/N5V98602.

Gleyzes, M., L. Perret, and P. Kubik (2012). "PLEIADES System Architecture and Main Performances." In: International Archives of the Photogrammetry, Remote Sensing and Spatial Information Sciences - ISPRS Archives. Vol. 39, pp. 537–542.

Goldstein, R. M., H. Engelhardt, B. Kamb, and R. M. Frolich (1993). "Satellite Radar Interferometry for Monitoring Ice Sheet Motion: Application to an Antarctic Ice Stream." In: *Science* 262.5139, pp. 1525–1530. ISSN: 0036-8075, 1095-9203. DOI: 10.1126/science.262.5139.1525.

Gomba, G. (2016). "Estimation and Compensation of Ionospheric Propagation Delay in Synthetic Aperture Radar (SAR) Signals." PhD Thesis. Technische Universität München. URL: https://elib.dlr.de/109038/.

Gomba, G., A. Parizzi, F. De Zan, M. Eineder, and R. Bamler (2016). "Toward Operational Compensation of Ionospheric Effects in SAR Interferograms: The Split-Spectrum Method." In: *IEEE Transactions on Geoscience and Remote Sensing* 54.3, pp. 1446–1461. ISSN: 0196-2892, 1558-0644. DOI: 10.1109/TGRS.2015.2481079.

Gourmelen, N., S. W. Kim, A. Shepherd, J. W. Park, A. V. Sundal, H. Björnsson, and F. Pálsson (2011). "Ice Velocity Determined Using Conventional and Multiple-Aperture InSAR." In: *Earth and Planetary Science Letters* 307.1, pp. 156–160. ISSN: 0012-821X. DOI: 10.1016/j.epsl.2011.04.026.

Gray, A. L., K. E. Mattar, and G. Sofko (2000). "Influence of Ionospheric Electron Density Fluctuations on Satellite Radar Interferometry." In: *Geophysical Research Letters* 27.10, pp. 1451–1454. ISSN: 1944-8007. DOI: 10.1029/2000GL000016.

Gray, L. (2011). "Using Multiple RADARSAT InSAR Pairs to Estimate a Full Three-Dimensional Solution for Glacial Ice Movement." In: *Geophysical Research Letters* 38.5. ISSN: 1944-8007. DOI: 10.1029/2010GL046484.

Hall, D. K. and G. A. Riggs (2015). *MODIS/Terra Snow Cover Monthly L3 Global 0.05Deg CMG, Version 6*. DOI: https://doi.org/10.5067/MODIS/MOD10CM.006.

Hardy, R. J., J. L. Bamber, and S. Orford (2000). "The delineation of drainage basins on the Greenland ice sheet for mass-balance analyses using a combined modelling and geographical information system approach." In: *Hydrological Processes* 14.11-

12, pp. 1931–1941. ISSN: 1099-1085. DOI: 10.1002/1099-1085(20000815/30)14:11/12<1931::AID-HYP46>3.0.CO;2-2.

Helm, V., A. Humbert, and H. Miller (2014). "Elevation and Elevation Change of Greenland and Antarctica Derived from CryoSat-2." In: *The Cryosphere* 8.4, pp. 1539–1559. ISSN: 1994-0416. DOI: https://doi.org/10.5194/tc-8-1539-2014.

Heo, J., J. H. Kim, and J. W. Kim (2009). "A New Methodology for Measuring Coastline Recession Using Buffering and Non-linear Least Squares Estimation." In: *International Journal of Geographical Information Science* 23.9, pp. 1165–1177. ISSN: 1365-8816. DOI: 10.1080/13658810802035642.

Hill, E. A., J. R. Carr, C. R. Stokes, and G. H. Gudmundsson (2018). "Dynamic Changes in Outlet Glaciers in Northern Greenland from 1948 to 2015." In: *The Cryosphere* 12.10, pp. 3243–3263. ISSN: 1994-0416. DOI: https://doi.org/10.5194/tc-12-3243-2018.

Hogg, A. E., A. Shepherd, N. Gourmelen, and M. Engdahl (2016). "Grounding Line Migration from 1992 to 2011 on Petermann Glacier, North-West Greenland." In: *Journal of Glaciology* 62.236, pp. 1104–1114. ISSN: 0022-1430, 1727-5652. DOI: 10.1017/jog.2016.83.

Holland, D. M., R. H. Thomas, B. de Young, M. H. Ribergaard, and B. Lyberth (2008). "Acceleration of Jakobshavn Isbræ Triggered by Warm Subsurface Ocean Waters." In: *Nature Geoscience* 1.10, pp. 659–664. ISSN: 1752-0908. DOI: 10.1038/ngeo316.

Howat, I. M., I. R. Joughin, and T. A. Scambos (2007). "Rapid Changes in Ice Discharge from Greenland Outlet Glaciers." In: *Science* 315.5818, pp. 1559–1561. ISSN: 0036-8075, 1095-9203. DOI: 10.1126/science.1138478.

Howat, I. M., A. Negrete, and B. E. Smith (2014). "The Greenland Ice Mapping Project (GIMP) Land Classification and Surface Elevation Data Sets." In: *The Cryosphere* 8.4, pp. 1509–1518. ISSN: 1994-0416. DOI: https://doi.org/10.5194/tc-8-1509-2014.

– (2015). *MEaSUREs Greenland Ice Sheet Mapping Project (GIMP) Digital Elevation Model, Version 1*. DOI: https://doi.org/10.5067/NV34YUIXLP9W.

Howat, I. M., I. R. Joughin, S. Tulaczyk, and S. Gogineni (2005). "Rapid Retreat and Acceleration of Helheim Glacier, East Greenland." In: *Geophysical Research Letters* 32.22. ISSN: 1944-8007. DOI: 10.1029/2005GL024737.

Howat, I. M., J. E. Box, Y. Ahn, A. Herrington, and E. M. McFadden (2010). "Seasonal Variability in the Dynamics of Marine-Terminating Outlet Glaciers in Greenland." In: *Journal of Glaciology* 56.198. ed, pp. 601–613. ISSN: 0022-1430, 1727-5652. DOI: 10.3189/002214310793146232.

Hurkmans, R. T.W. L., J. L. Bamber, C. H. Davis, I. R. Joughin, K. S. Khvorostovsky, B. S. Smith, and N. Schoen (2014). "Time-Evolving Mass Loss of the Greenland Ice Sheet from Satellite Altimetry." In: *The Cryosphere* 8.5, pp. 1725–1740. ISSN: 1994-0416. DOI: https://doi.org/10.5194/tc-8-1725-2014.

Jezek, K. C., D. Floricioiu, K. Farness, N. Yague-Martinez, and M. Eineder (2009). "TerraSAR-X Observations of the Recovery Glacier System, Antarctica." In: *2009 IEEE International Geoscience and Remote Sensing Symposium*. 2009 IEEE International Geoscience and Remote Sensing Symposium. Vol. 2, pp. II–226–II–229. DOI: 10.1109/IGARSS.2009.5418049.

Joughin, I. R. (2015). *MEaSUREs Greenland Ice Sheet Mosaics from SAR Data, Version 1*. DOI: https://doi.org/10.5067/6187DQUL3FR5.

Joughin, I. R., M. A. Fahnestock, and J. L. Bamber (2000). "Ice Flow in the Northeast Greenland Ice Stream." In: *Annals of Glaciology* 31. ed, pp. 141–146. ISSN: 0260-3055, 1727-5644. DOI: 10.3189/172756400781820002.

Joughin, I. R., R. Kwok, and M. A. Fahnestock (1998). "Interferometric Estimation of Three-Dimensional Ice-Flow Using Ascending and Descending Passes." In: *IEEE Transactions on Geoscience and Remote Sensing* 36.1, pp. 25–37. ISSN: 0196-2892, 1558-0644. DOI: 10.1109/36.655315.

Joughin, I. R., B. E. Smith, and I. M. Howat (2018a). "A Complete Map of Greenland Ice Velocity Derived from Satellite Data Collected over 20 Years." In: *Journal of Glaciology* 64.243, pp. 1–11. ISSN: 0022-1430, 1727-5652. DOI: 10.1017/jog.2017.73.

Joughin, I. R., I. M. Howat, R. B. Alley, G. Ekstrom, M. A. Fahnestock, T. Moon, M. Nettles, M. Truffer, and V. C. Tsai (2008). "Ice-Front Variation and Tidewater Behavior on Helheim and Kangerdlugssuaq Glaciers, Greenland." In: *Journal of Geophysical Research: Earth Surface* 113.F1. ISSN: 2156-2202. DOI: 10.1029/2007JF000837.

Joughin, I. R., B. E. Smith, I. M. Howat, T. A. Scambos, and T. Moon (2010). "Greenland Flow Variability from Ice-Sheet-Wide Velocity Mapping." In: *Journal of Glaciology* 56.197. ed, pp. 415–430. ISSN: 0022-1430, 1727-5652. DOI: 10.3189/002214310792447734.

Joughin, I. R., B. E. Smith, I. M. Howat, D. Floricioiu, R. B. Alley, M. Truffer, and M. A. Fahnestock (2012). "Seasonal to Decadal Scale Variations in the Surface Velocity of Jakobshavn Isbrae, Greenland: Observation and Model-Based Analysis." In: *Journal of Geophysical Research: Earth Surface* 117.F2. ISSN: 2156-2202. DOI: 10.1029/2011JF002110.

Joughin, I. R., B. E. Smith, D. E. Shean, and D. Floricioiu (2014). "Brief Communication: Further Summer Speedup of Jakobshavn Isbræ." In: *The Cryosphere* 8.1, pp. 209–214. ISSN: 1994-0416. DOI: https://doi.org/10.5194/tc-8-209-2014.

Joughin, I. R., D. E. Shean, B. E. Smith, and D. Floricioiu (2019). "A Decade of Variability on Jakobshavn Isbrae: Ocean Temperatures Pace Speed Through Influence on Mélange Rigidity." In: *The Cryosphere Discussions*, pp. 1–27. ISSN: 1994-0416. DOI: https://doi.org/10.5194/tc-2019-197.

Joughin, I., B. E. Smith, and I. Howat (2018b). "Greenland Ice Mapping Project: Ice Flow Velocity Variation at Sub-Monthly to Decadal Timescales." In: *The Cryosphere* 12.7, pp. 2211–2227. ISSN: 1994-0416. DOI: https://doi.org/10.5194/tc-12-2211-2018.

Jung, H.-S., S.-H. Yun, and M.-J. Jo (2015). "An Improvement of Multiple-Aperture SAR Interferometry Performance in the Presence of Complex and Large Line-of-Sight Deformation." In: *IEEE Journal of Selected Topics in Applied Earth Observations and Remote Sensing* 8.4, pp. 1743–1752. ISSN: 2151-1535. DOI: 10.1109/JSTARS.2015.2399249.

Kääb, A. (2002). "Monitoring High-Mountain Terrain Deformation from Repeated Air- and Spaceborne Optical Data: Examples Using Digital Aerial Imagery and ASTER Data." In: *ISPRS Journal of Photogrammetry and Remote Sensing*. Geomatics in Mountainous Areas – The International Year of the Mountains, 2002 57.1, pp. 39–52. ISSN: 0924-2716. DOI: 10.1016/S0924-2716(02)00114-4.

Kalnay, E. et al. (1996). "The NCEP/NCAR 40-Year Reanalysis Project." In: *Bulletin of the American Meteorological Society* 77.3, pp. 437–472. ISSN: 0003-0007. DOI: 10.1175/1520-0477(1996)077<0437:TNYRP>2.0.CO;2.

Kehrl, L. M., I. R. Joughin, D. E. Shean, D. Floricioiu, and L. Krieger (2017). "Seasonal and Interannual Variabilities in Terminus Position, Glacier Velocity, and Surface Elevation at Helheim and Kangerlussuaq Glaciers from 2008 to 2016." In: *Journal of Geophysical Research: Earth Surface* 122.9, pp. 1635–1652. ISSN: 2169-9011. DOI: 10.1002/2016JF004133.

Kelley, M. C. (2009). *The Earth's Ionosphere: Plasma Physics and Electrodynamics*. Vol. 96. Academic press.

Khan, S. A. et al. (2014). "Sustained Mass Loss of the Northeast Greenland Ice Sheet Triggered by Regional Warming." In: *Nature Climate Change* 4.4, pp. 292–299. ISSN: 1758-6798. DOI: 10.1038/nclimate2161.

Khan, S. A., A. Aschwanden, A. A. Bjørk, J. Wahr, K. K. Kjeldsen, and K. H. Kjær (2015). "Greenland Ice Sheet Mass Balance: A Review." In: *Reports on Progress in Physics* 78.4, p. 046801. ISSN: 0034-4885, 1361-6633. DOI: 10.1088/0034-4885/78/4/046801.

Korona, J., E. Berthier, M. Bernard, F. Rémy, and E. Thouvenot (2009). "SPIRIT. SPOT 5 Stereoscopic Survey of Polar Ice: Reference Images and Topographies during the Fourth International Polar Year (2007–2009)." In: *ISPRS Journal of Photogrammetry and Remote Sensing* 64.2, pp. 204–212. ISSN: 0924-2716. DOI: 10.1016/j.isprsjprs.2008.10.005.

Krieger, G., A. Moreira, H. Fiedler, I. Hajnsek, M. Werner, M. Younis, and M. Zink (2007). "TanDEM-X: A Satellite Formation for High-Resolution SAR Interferometry." In: *IEEE Transactions on Geoscience and Remote Sensing* 45.11, pp. 3317–3341. ISSN: 0196-2892, 1558-0644. DOI: 10.1109/TGRS.2007.900693.

Krieger, G. et al. (2009). "The Tandem-L Mission Proposal: Monitoring Earth's Dynamics with High Resolution SAR Interferometry." In: *2009 IEEE Radar Conference*. 2009 IEEE Radar Conference, pp. 1–6. DOI: 10.1109/RADAR.2009.4977077.

Krieger, L. and D. Floricioiu (2017). "Automatic Glacier Calving Front Delineation on TerraSAR-X and Sentinel-1 SAR Imagery." In: *2017 IEEE International Geoscience and Remote Sensing Symposium (IGARSS)*. 2017 IEEE International Geoscience and Remote Sensing Symposium (IGARSS), pp. 2817–2820. DOI: 10.1109/IGARSS.2017.8127584.

– (2019). "Improved Delineation of Individual Outlet Glacier Drainage Basins From Tandem-X Elevations And Sentinel-1 Velocities." In: *IGARSS 2019 - 2019 IEEE International Geoscience and Remote Sensing Symposium*. IGARSS 2019 - 2019 IEEE International Geoscience and Remote Sensing Symposium, pp. 3998–4001. DOI: 10.1109/IGARSS.2019.8897921.

Krieger, L., D. Floricioiu, and N. Neckel (2019). *Drainage Basin Delineation for Outlet Glaciers of Northeast Greenland Based on Sentinel-1 Ice Velocities and TanDEM-X Elevations*. DOI: https://doi.org/10.1594/PANGAEA.908594.

– (2020). "Drainage Basin Delineation for Outlet Glaciers of Northeast Greenland Based on Sentinel-1 Ice Velocities and TanDEM-X Elevations." In: *Remote Sensing of Environment* 237, p. 111483. ISSN: 0034-4257. DOI: 10.1016/j.rse.2019.111483.

Krieger, L., U. Strößenreuther, V. Helm, D. Floricioiu, and M. Horwath (2020). "Synergistic Use of Single-Pass Interferometry and Radar Altimetry to Measure Mass Loss of NEGIS Outlet Glaciers between 2011 and 2014." In: *Remote Sensing* 12.6, p. 996. DOI: 10.3390/rs12060996.

Kuipers Munneke, P. et al. (2015). "Elevation Change of the Greenland Ice Sheet Due to Surface Mass Balance and Firn Processes, 1960–2014." In: *The Cryosphere* 9.6, pp. 2009–2025. ISSN: 1994-0416. DOI: https://doi.org/10.5194/tc-9-2009-2015.

Kurtz, N. T., S. L. Farrell, M. Studinger, N. Galin, J. P. Harbeck, R. Lindsay, V. D. Onana, B. Panzer, and J. G. Sonntag (2013). "Sea Ice Thickness, Freeboard, and Snow Depth Products from Operation IceBridge Airborne Data." In: *The Cryosphere* 7.4, pp. 1035–1056. ISSN: 1994-0416. DOI: https://doi.org/10.5194/tc-7-1035-2013.

Lea, J. M., D. W. F. Mair, and B. R. Rea (2014). "Evaluation of Existing and New Methods of Tracking Glacier Terminus Change." In: *Journal of Glaciology* 60.220. ed, pp. 323–332. ISSN: 0022-1430, 1727-5652. DOI: 10.3189/2014JoG13J061.

Lemos, A., A. Shepherd, M. McMillan, and A. E. Hogg (2018). "Seasonal Variations in the Flow of Land-Terminating Glaciers in Central-West Greenland Using Sentinel-1 Imagery." In: *Remote Sensing* 10.12, p. 1878. DOI: 10.3390/rs10121878.

Lewis, J. P. (1995). "Fast Normalized Cross-Correlation." In: *Vision Interface*, pp. 120–123.

Lewis, S. M. and L. C. Smith (2009). "Hydrologic drainage of the Greenland Ice Sheet." In: *Hydrological Processes* 23.14, pp. 2004–2011. ISSN: 1099-1085. DOI: 10.1002/hyp.7343.

Ligtenberg, S. R. M., P. Kuipers Munneke, B. P. Y. Noël, and M. R. van den Broeke (2018). "Brief Communication: Improved Simulation of the Present-Day Greenland Firn Layer (1960–2016)." In: *The Cryosphere* 12.5, pp. 1643–1649. ISSN: 1994-0416. DOI: https://doi.org/10.5194/tc-12-1643-2018.

Liu, H. and K. C. Jezek (2004). "Automated Extraction of Coastline from Satellite Imagery by Integrating Canny Edge Detection and Locally Adaptive Thresholding Methods." In: *International Journal of Remote Sensing* 25.5, pp. 937–958. ISSN: 0143-1161. DOI: 10.1080/0143116031000139890.

Lucchitta, B. K. and H. M. Ferguson (1986). "Antarctica: Measuring Glacier Velocity from Satellite Images." In: *Science* 234.4780, pp. 1105–1108. ISSN: 0036-8075, 1095-9203. DOI: 10.1126/science.234.4780.1105.

Luckman, A., T. Murray, R. de Lange, and E. Hanna (2006). "Rapid and Synchronous Ice-Dynamic Changes in East Greenland." In: *Geophysical Research Letters* 33.3. ISSN: 1944-8007. DOI: 10.1029/2005GL025428.

Lüttig, C., N. Neckel, and A. Humbert (2017). "A Combined Approach for Filtering Ice Surface Velocity Fields Derived from Remote Sensing Methods." In: *Remote Sensing* 9.10, p. 1062. DOI: 10.3390/rs9101062.

Malz, P., W. Meier, G. Casassa, R. Jaña, P. Skvarca, and M. H. Braun (2018). "Elevation and Mass Changes of the Southern Patagonia Icefield Derived from TanDEM-X and SRTM Data." In: *Remote Sensing* 10.2, p. 188. DOI: 10.3390/rs10020188.

Martin, T. V., H. J. Zwally, A. C. Brenner, and R. A. Bindschadler (1983). "Analysis and Retracking of Continental Ice Sheet Radar Altimeter Waveforms." In: *Journal of Geophysical Research: Oceans* 88.C3, pp. 1608–1616. ISSN: 2156-2202. DOI: 10.1029/JC088iC03p01608.

Marzeion, B., A. H. Jarosch, and M. Hofer (2012). "Past and Future Sea-Level Change from the Surface Mass Balance of Glaciers." In: *The Cryosphere* 6.6, pp. 1295–1322. ISSN: 1994-0416. DOI: https://doi.org/10.5194/tc-6-1295-2012.

Mätzler, C. (1987). "Applications of the Interaction of Microwaves with the Natural Snow Cover." In: *Remote Sensing Reviews* 2.2, pp. 259–387. ISSN: 0275-7257. DOI: 10.1080/02757258709532086.

Mayer, C., N. Reeh, F. Jung-Rothenhäusler, P. Huybrechts, and H. Oerter (2000). "The Subglacial Cavity and Implied Dynamics under Nioghalvfjerdsfjorden Glacier, NE-Greenland." In: *Geophysical Research Letters* 27.15, pp. 2289–2292. ISSN: 1944-8007. DOI: 10.1029/2000GL011514.

Mayer, C., J. Schaffer, T. Hattermann, D. Floricioiu, L. Krieger, P. A. Dodd, T. Kanzow, C. Licciulli, and C. Schannwell (2018). "Large Ice Loss Variability at Nioghalvfjerdsfjorden Glacier, Northeast-Greenland." In: *Nature Communications* 9.1, pp. 1–11. ISSN: 2041-1723. DOI: 10.1038/s41467-018-05180-x.

McGrath, D., W. Colgan, N. Bayou, A. Muto, and K. Steffen (2013). "Recent Warming at Summit, Greenland: Global Context and Implications." In: *Geophysical Research Letters* 40.10, pp. 2091–2096. ISSN: 1944-8007. DOI: 10.1002/grl.50456.

McMillan, M., A. Shepherd, A. V. Sundal, K. H. Briggs, A. Muir, A. J. Ridout, A. E. Hogg, and D. J. Wingham (2014). "Increased Ice Losses from Antarctica Detected by CryoSat-2." In: *Geophysical Research Letters* 41.11, pp. 3899–3905. ISSN: 1944-8007. DOI: 10.1002/2014GL060111.

McMillan, M. et al. (2016). "A High-Resolution Record of Greenland Mass Balance." In: *Geophysical Research Letters* 43.13, pp. 7002–7010. ISSN: 1944-8007. DOI: 10.1002/2016GL069666.

Meehl, G. A., T. F. Stocker, W. D. Collins, P. Friedlingstein, T Gaye, J. M. Gregory, A. Kitoh, R. Knutti, J. M. Murphy, A. Noda, et al. (2007). "Global Climate Projections." In: *AR4 Climate Change 2007: The Physical Science Basis*.

Meyer, F. J., J. Nicoll, and B. Bristow (2009). "Mapping Aurora Activity with SAR — a Case Study." In: *2009 IEEE International Geoscience and Remote Sensing Symposium*. 2009 IEEE International Geoscience and Remote Sensing Symposium. Vol. 4, pp. IV–1–IV–4. DOI: 10.1109/IGARSS.2009.5417610.

Milillo, P., B. Riel, B. Minchew, S.-H. Yun, M. Simons, and P. Lundgren (2016). "On the Synergistic Use of SAR Constellations' Data Exploitation for Earth Science and Natural Hazard Response." In: *IEEE Journal of Selected Topics in Applied Earth Observations and Remote Sensing* 9.3, pp. 1095–1100. ISSN: 1939-1404, 2151-1535. DOI: 10.1109/JSTARS.2015.2465166.

Milillo, P., E. Rignot, J. Mouginot, B. Scheuchl, M. Morlighem, X. Li, and J. T. Salzer (2017). "On the Short-Term Grounding Zone Dynamics of Pine Island Glacier, West Antarctica, Observed With COSMO-SkyMed Interferometric Data." In: *Geophysical Research Letters* 44.20, pp. 10,436–10,444. ISSN: 1944-8007. DOI: 10.1002/2017GL074320.

Milillo, P., E. Rignot, P. Rizzoli, B. Scheuchl, J. Mouginot, J. Bueso-Bello, and P. Prats-Iraola (2019). "Heterogeneous Retreat and Ice Melt of Thwaites Glacier, West Antarctica." In: *Science Advances* 5.1, eaau3433. ISSN: 2375-2548. DOI: 10.1126/sciadv.aau3433.

Mohajerani, Y., M. Wood, I. Velicogna, and E. Rignot (2019). "Detection of Glacier Calving Margins with Convolutional Neural Networks: A Case Study." In: *Remote Sensing* 11.1, p. 74. DOI: 10.3390/rs11010074.

Mohr, J. J., N. Reeh, and S. N. Madsen (1998). "Three-Dimensional Glacial Flow and Surface Elevation Measured with Radar Interferometry." In: *Nature* 391.6664, pp. 273–276. ISSN: 1476-4687. DOI: 10.1038/34635.

Moon, T. and I. R. Joughin (2008). "Changes in Ice Front Position on Greenland's Outlet Glaciers from 1992 to 2007." In: *Journal of Geophysical Research: Earth Surface* 113.F2. ISSN: 2156-2202. DOI: 10.1029/2007JF000927.

Moon, T., I. R. Joughin, and B. Smith (2015). "Seasonal to Multiyear Variability of Glacier Surface Velocity, Terminus Position, and Sea Ice/Ice Mélange in Northwest Greenland." In: *Journal of Geophysical Research: Earth Surface* 120.5, pp. 818–833. ISSN: 2169-9011. DOI: 10.1002/2015JF003494.

Moon, T., I. R. Joughin, B. Smith, and I. M. Howat (2012). "21st-Century Evolution of Greenland Outlet Glacier Velocities." In: *Science* 336.6081, pp. 576–578. ISSN: 0036-8075, 1095-9203. DOI: 10.1126/science.1219985.

Morlighem, M. et al. (2017a). "BedMachine v3: Complete Bed Topography and Ocean Bathymetry Mapping of Greenland From Multibeam Echo Sounding Combined

With Mass Conservation." In: *Geophysical Research Letters* 44.21, pp. 11,051–11,061. ISSN: 1944-8007. DOI: 10.1002/2017GL074954.

Morlighem, M., C. N. Williams, E. Rignot, L. An, J. E. Arndt, J. L. Bamber, G. A. Catania, N. Chauché, J. A. Dowdeswell, B. Dorschel, et al. (2017b). *IceBridge BedMachine Greenland, Version 3*. DOI: https://doi.org/10.5067/2CIX82HUV88Y.

Motyka, R. J. et al. (2017). "Asynchronous Behavior of Outlet Glaciers Feeding Godthåbsfjord (Nuup Kangerlua) and the Triggering of Narsap Sermia's Retreat in SW Greenland." In: *Journal of Glaciology* 63.238, pp. 288–308. ISSN: 0022-1430, 1727-5652. DOI: 10.1017/jog.2016.138.

Mouginot, J. and E. Rignot (2019). *Glacier Catchments/Basins for the Greenland Ice Sheet*. Published: UC Irvine Dash. DOI: 10.7280/D1WT11.

Mouginot, J., E. Rignot, and B. Scheuchl (2019). "Continent-Wide, Interferometric SAR Phase, Mapping of Antarctic Ice Velocity." In: *Geophysical Research Letters* 46.16, pp. 9710–9718. ISSN: 1944-8007. DOI: 10.1029/2019GL083826.

Mouginot, J., B. Scheuchl, and E. Rignot (2012). "Mapping of Ice Motion in Antarctica Using Synthetic-Aperture Radar Data." In: *Remote Sensing* 4.9, pp. 2753–2767. DOI: 10.3390/rs4092753.

Mouginot, J., E. Rignot, B. Scheuchl, I. Fenty, A. Khazendar, M. Morlighem, A. Buzzi, and J. Paden (2015). "Fast Retreat of Zachariæ Isstrøm, Northeast Greenland." In: *Science* 350.6266, pp. 1357–1361. ISSN: 0036-8075, 1095-9203. DOI: 10.1126/science.aac7111.

Mouginot, J., E. Rignot, B. Scheuchl, and R. Millan (2017). "Comprehensive Annual Ice Sheet Velocity Mapping Using Landsat-8, Sentinel-1, and RADARSAT-2 Data." In: *Remote Sensing* 9.4, p. 364. DOI: 10.3390/rs9040364.

Mouginot, J., E. Rignot, A. A. Bjørk, M. R. van den Broeke, R. Millan, M. Morlighem, B. P. Y. Noël, B. Scheuchl, and M. Wood (2019). "Forty-Six Years of Greenland Ice Sheet Mass Balance from 1972 to 2018." In: *Proceedings of the National Academy of Sciences* 116.19, pp. 9239–9244. ISSN: 0027-8424. DOI: 10.1073/pnas.1904242116.

Nagler, T., H. Rott, M. Hetzenecker, J. Wuite, and P. Potin (2015a). *Greenland Ice Velocity Map 2015 v. 1*. URL: http://products.esa-icesheets-cci.org.

– (2015b). "The Sentinel-1 Mission: New Opportunities for Ice Sheet Observations." In: *Remote Sensing* 7.7, pp. 9371–9389. DOI: 10.3390/rs70709371.

Nghiem, S. V., D. K. Hall, T. L. Mote, M. Tedesco, M. R. Albert, K. Keegan, C. A. Shuman, N. E. DiGirolamo, and G. Neumann (2012). "The Extreme Melt across the Greenland Ice Sheet in 2012." In: *Geophysical Research Letters* 39.20. ISSN: 1944-8007. DOI: 10.1029/2012GL053611.

Nilsson, J. et al. (2015). "Greenland 2012 Melt Event Effects on CryoSat-2 Radar Altimetry." In: *Geophysical Research Letters* 42.10, pp. 3919–3926. ISSN: 1944-8007. DOI: 10.1002/2015GL063296.

Nilsson, J., A. Gardner, L. Sandberg Sørensen, and R. Forsberg (2016). "Improved Retrieval of Land Ice Topography from CryoSat-2 Data and Its Impact for Volume-Change Estimation of the Greenland Ice Sheet." In: *The Cryosphere* 10.6, pp. 2953–2969. ISSN: 1994-0416. DOI: https://doi.org/10.5194/tc-10-2953-2016.

Noël, B. P. Y., W. J. van de Berg, H. Machguth, S. Lhermitte, I. M. Howat, X. Fettweis, and M. R. van den Broeke (2016). "A Daily, 1 Km Resolution Data Set of Downscaled Greenland Ice Sheet Surface Mass Balance (1958–2015)." In: *The Cryosphere* 10.5, pp. 2361–2377. ISSN: 1994-0416. DOI: https://doi.org/10.5194/tc-10-2361-2016.

Noël, B. P. Y. et al. (2018). "Modelling the Climate and Surface Mass Balance of Polar Ice Sheets Using RACMO2 – Part 1: Greenland (1958–2016)." In: *The Cryosphere* 12.3, pp. 811–831. ISSN: 1994-0416. DOI: https://doi.org/10.5194/tc-12-811-2018.

Nolin, A. W. and M. C. Payne (2007). "Classification of Glacier Zones in Western Greenland Using Albedo and Surface Roughness from the Multi-Angle Imaging SpectroRadiometer (MISR)." In: *Remote Sensing of Environment*. Multi-Angle Imaging SpectroRadiometer (MISR) Special Issue 107.1, pp. 264–275. ISSN: 0034-4257. DOI: 10.1016/j.rse.2006.11.004.

Paden, J., J. Li, C. Leuschen, F. Rodriguez-Morales, and R. Hale (2010, updated 2019). *IceBridge MCoRDS L2 Ice Thickness, Version 1*. DOI: https://doi.org/10.5067/GDQ0CUCVTE2Q.

Padman, L. and S. Erofeeva (2004). "A Barotropic Inverse Tidal Model for the Arctic Ocean." In: *Geophysical Research Letters* 31.2. ISSN: 1944-8007. DOI: 10.1029/2003GL019003.

Padman, L., H. A. Fricker, R. Coleman, S. Howard, and L. Erofeeva (2002). "A New Tide Model for the Antarctic Ice Shelves and Seas." In: *Annals of Glaciology* 34. ed, pp. 247–254. ISSN: 0260-3055, 1727-5644. DOI: 10.3189/172756402781817752.

Parizzi, A. and W. Abdel Jaber (2018). "Estimating Strain and Rotation From Wrapped SAR Interferograms." In: *IEEE Geoscience and Remote Sensing Letters* 15.9, pp. 1367–1371. ISSN: 1545-598X, 1558-0571. DOI: 10.1109/LGRS.2018.2838763.

Paterson, W. S. B. (2016). *The Physics of Glaciers*. Elsevier. 491 pp. ISBN: 978-1-4832-8725-6.

Peltier, W. R. (2004). "GLOBAL GLACIAL ISOSTASY AND THE SURFACE OF THE ICE-AGE EARTH: The ICE-5G (VM2) Model and GRACE." In: *Annual Review of Earth and Planetary Sciences* 32.1, pp. 111–149. ISSN: 0084-6597. DOI: 10.1146/annurev.earth.32.082503.144359.

Pritchard, H. D., S. R. M. Ligtenberg, H. A. Fricker, D. G. Vaughan, M. R. van den Broeke, and L. Padman (2012). "Antarctic Ice-Sheet Loss Driven by Basal Melting of Ice Shelves." In: *Nature* 484.7395, pp. 502–505. ISSN: 1476-4687. DOI: 10.1038/nature10968.

RGI Consortium (2017). *Randolph Glacier Inventory – A Dataset of Global Glacier Outlines: Version 6.0*. Published: Technical Report, Global Land Ice Measurements from Space, Colorado, USA. Digital Media. DOI: 10.7265/N5-RGI-60.

Reeh, N., C. E. Bøggild, and H. Oerter (1994). "Surge of Storstrømmen, a Large Outlet Glacier from the Inland Ice of North-East Greenland." In: *Grønlands Geologiske Undersøgelse Rapport 162*, pp. 201–209. ISSN: 0418-6559. URL: https://epic.awi.de/id/eprint/2534/ (visited on 11/04/2019).

Rignot, E., J. Mouginot, and B. Scheuchl (2011a). "Ice Flow of the Antarctic Ice Sheet." In: *Science* 333.6048, pp. 1427–1430. ISSN: 0036-8075, 1095-9203. DOI: 10.1126/science.1208336.

Rignot, E., J. Mouginot, and B. Scheuchl (2016). *MEaSUREs Antarctic Grounding Line from Differential Satellite Radar Interferometry, Version 2*. DOI: https://doi.org/10.5067/IKBWW4RYHF1Q.

Rignot, E. (1996). "Tidal Motion, Ice Velocity and Melt Rate of Petermann Gletscher, Greenland, Measured from Radar Interferometry." In: *Journal of Glaciology* 42.142. edited, pp. 476–485. ISSN: 0022-1430, 1727-5652. DOI: 10.3189/S0022143000003464.

– (2008). "Changes in West Antarctic Ice Stream Dynamics Observed with ALOS PALSAR Data." In: *Geophysical Research Letters* 35.12. ISSN: 1944-8007. DOI: 10.1029/2008GL033365.

Rignot, E., K. Echelmeyer, and W. Krabill (2001). "Penetration Depth of Interferometric Synthetic-Aperture Radar Signals in Snow and Ice." In: *Geophysical Research Letters* 28.18, pp. 3501–3504. ISSN: 1944-8007. DOI: 10.1029/2000GL012484.

Rignot, E. and P. Kanagaratnam (2006). "Changes in the Velocity Structure of the Greenland Ice Sheet." In: *Science* 311.5763, pp. 986–990. ISSN: 0036-8075, 1095-9203. DOI: 10.1126/science.1121381.

Rignot, E. and J. Mouginot (2012). "Ice Flow in Greenland for the International Polar Year 2008–2009." In: *Geophysical Research Letters* 39.11. ISSN: 1944-8007. DOI: 10.1029/2012GL051634.

Rignot, E., J. Mouginot, and B. Scheuchl (2011b). "Antarctic Grounding Line Mapping from Differential Satellite Radar Interferometry." In: *Geophysical Research Letters* 38.10. ISSN: 1944-8007. DOI: 10.1029/2011GL047109.

Rignot, E., J. Mouginot, M. Morlighem, H. Seroussi, and B. Scheuchl (2014). "Widespread, Rapid Grounding Line Retreat of Pine Island, Thwaites, Smith, and Kohler Glaciers, West Antarctica, from 1992 to 2011." In: *Geophysical Research Letters* 41.10, pp. 3502–3509. ISSN: 1944-8007. DOI: 10.1002/2014GL060140.

Rignot, E., I. Fenty, Y. Xu, C. Cai, I. Velicogna, C. O. Cofaigh, J. A. Dowdeswell, W. Weinrebe, G. A. Catania, and D. Duncan (2016). "Bathymetry Data Reveal Glaciers Vulnerable to Ice-Ocean Interaction in Uummannaq and Vaigat Glacial Fjords, West Greenland." In: *Geophysical Research Letters* 43.6, pp. 2667–2674. ISSN: 1944-8007. DOI: 10.1002/2016GL067832.

Rizzoli, P., M. Martone, H. Rott, and A. Moreira (2017a). "Characterization of Snow Facies on the Greenland Ice Sheet Observed by TanDEM-X Interferometric SAR Data." In: *Remote Sensing* 9.4, p. 315. DOI: 10.3390/rs9040315.

Rizzoli, P. et al. (2017b). "Generation and Performance Assessment of the Global TanDEM-X Digital Elevation Model." In: *ISPRS Journal of Photogrammetry and Remote Sensing* 132, pp. 119–139. ISSN: 0924-2716. DOI: 10.1016/j.isprsjprs.2017.08.008.

Rolstad, C., T. Haug, and B. Denby (2009). "Spatially Integrated Geodetic Glacier Mass Balance and Its Uncertainty Based on Geostatistical Analysis: Application to the Western Svartisen Ice Cap, Norway." In: *Journal of Glaciology* 55.192, pp. 666–680. ISSN: 0022-1430, 1727-5652. DOI: 10.3189/002214309789470950.

Rosenau, R., M. Scheinert, and R. Dietrich (2015). "A Processing System to Monitor Greenland Outlet Glacier Velocity Variations at Decadal and Seasonal Time Scales Utilizing the Landsat Imagery." In: *Remote Sensing of Environment* 169, pp. 1–19. ISSN: 0034-4257. DOI: 10.1016/j.rse.2015.07.012.

Rossi, C., M. Eineder, T. Fritz, and H. Breit (2010). "TanDEM-X Mission: Raw DEM Generation." In: *8th European Conference on Synthetic Aperture Radar*. 8th European Conference on Synthetic Aperture Radar. Aachen, pp. 1–4.

Rott, H., W. Rack, and T. Nagler (2007). "Increased Export of Grounded Ice after the Collapse of Northern Larsen Ice Shelf, Antarctic Peninsula, Observed by Envisat ASAR." In: *2007 IEEE International Geoscience and Remote Sensing Symposium*. 2007 IEEE International Geoscience and Remote Sensing Symposium, pp. 1174–1176. DOI: 10.1109/IGARSS.2007.4423013.

Rott, H., W. Rack, P. Skvarca, and H. D. Angelis (2002). "Northern Larsen Ice Shelf, Antarctica: Further Retreat after Collapse." In: *Annals of Glaciology* 34. ed, pp. 277–282. ISSN: 0260-3055, 1727-5644. DOI: 10.3189/172756402781817716.

Rott, H., W. Abdel Jaber, J. Wuite, S. Scheiblauer, D. Floricioiu, J. M. van Wessem, T. Nagler, N. Miranda, and M. R. van den Broeke (2018). "Changing Pattern of

Ice Flow and Mass Balance for Glaciers Discharging into the Larsen A and B Embayments, Antarctic Peninsula, 2011 to 2016." In: *The Cryosphere* 12.4, pp. 1273–1291. ISSN: 1994-0416. DOI: https://doi.org/10.5194/tc-12-1273-2018.

Ryan, J. C., L. C. Smith, D. van As, S. W. Cooley, M. G. Cooper, L. H. Pitcher, and A. Hubbard (2019). "Greenland Ice Sheet Surface Melt Amplified by Snowline Migration and Bare Ice Exposure." In: *Science Advances* 5.3, eaav3738. ISSN: 2375-2548. DOI: 10.1126/sciadv.aav3738.

Sakumura, C., S. Bettadpur, and S. Bruinsma (2014). "Ensemble Prediction and Intercomparison Analysis of GRACE Time-Variable Gravity Field Models." In: *Geophysical Research Letters* 41.5, pp. 1389–1397. ISSN: 1944-8007. DOI: 10.1002/2013GL058632.

Scambos, T. A., M. J. Dutkiewicz, J. C. Wilson, and R. A. Bindschadler (1992). "Application of Image Cross-Correlation to the Measurement of Glacier Velocity Using Satellite Image Data." In: *Remote Sensing of Environment* 42.3, pp. 177–186. ISSN: 0034-4257. DOI: 10.1016/0034-4257(92)90101-O.

Scambos, T. A., T. M. Haran, M. A. Fahnestock, T. H. Painter, and J. Bohlander (2007). "MODIS-Based Mosaic of Antarctica (MOA) Data Sets: Continent-Wide Surface Morphology and Snow Grain Size." In: *Remote Sensing of Environment*. Remote Sensing of the Cryosphere Special Issue 111.2, pp. 242–257. ISSN: 0034-4257. DOI: 10.1016/j.rse.2006.12.020.

Schild, K. M. and G. S. Hamilton (2013). "Seasonal Variations of Outlet Glacier Terminus Position in Greenland." In: *Journal of Glaciology* 59.216. ed, pp. 759–770. ISSN: 0022-1430, 1727-5652. DOI: 10.3189/2013JoG12J238.

Schoof, C. (2007). "Ice Sheet Grounding Line Dynamics: Steady States, Stability, and Hysteresis." In: *Journal of Geophysical Research: Earth Surface*. ISSN: 2156-2202. DOI: 10.1029/2006JF000664@10.1002/(ISSN)2169-9011.TIDEWATER1.

Schröder, L. et al. (2017). "Validation of Satellite Altimetry by Kinematic GNSS in Central East Antarctica." In: *The Cryosphere* 11.3, pp. 1111–1130. ISSN: 1994-0416. DOI: https://doi.org/10.5194/tc-11-1111-2017.

Schröder, L., M. Horwath, R. Dietrich, V. Helm, M. R. van den Broeke, and S. R. M. Ligtenberg (2019). "Four Decades of Antarctic Surface Elevation Changes from Multi-Mission Satellite Altimetry." In: *The Cryosphere* 13.2, pp. 427–449. ISSN: 1994-0416. DOI: https://doi.org/10.5194/tc-13-427-2019.

Schutz, B. E., H. J. Zwally, C. A. Shuman, D. Hancock, and J. P. DiMarzio (2005). "Overview of the ICESat Mission." In: *Geophysical Research Letters* 32.21. ISSN: 1944-8007. DOI: 10.1029/2005GL024009.

Seale, A., P. Christoffersen, R. I. Mugford, and M. O'Leary (2011). "Ocean Forcing of the Greenland Ice Sheet: Calving Fronts and Patterns of Retreat Identified by Automatic Satellite Monitoring of Eastern Outlet Glaciers." In: *Journal of Geophysical Research: Earth Surface* 116.F3. ISSN: 2156-2202. DOI: 10.1029/2010JF001847.

Shannon, S. R. et al. (2013). "Enhanced Basal Lubrication and the Contribution of the Greenland Ice Sheet to Future Sea-Level Rise." In: *Proceedings of the National Academy of Sciences* 110.35, pp. 14156–14161. ISSN: 0027-8424, 1091-6490. DOI: 10.1073/pnas.1212647110.

Sharma, J. J., I. Hajnsek, K. P. Papathanassiou, and A. Moreira (2013). "Estimation of Glacier Ice Extinction Using Long-Wavelength Airborne Pol-InSAR." In: *IEEE Transactions on Geoscience and Remote Sensing* 51.6, pp. 3715–3732. ISSN: 0196-2892, 1558-0644. DOI: 10.1109/TGRS.2012.2220855.

Shean, D. E., O. Alexandrov, Z. M. Moratto, B. E. Smith, I. R. Joughin, C. Porter, and P. Morin (2016). "An Automated, Open-Source Pipeline for Mass Production of Digital Elevation Models (DEMs) from Very-High-Resolution Commercial Stereo Satellite Imagery." In: *ISPRS Journal of Photogrammetry and Remote Sensing* 116, pp. 101–117. ISSN: 0924-2716. DOI: 10.1016/j.isprsjprs.2016.03.012.

Shean, D. E., I. R. Joughin, P. Dutrieux, B. E. Smith, and E. Berthier (2019). "Ice Shelf Basal Melt Rates from a High-Resolution Digital Elevation Model (DEM) Record for Pine Island Glacier, Antarctica." In: *The Cryosphere* 13.10, pp. 2633–2656. ISSN: 1994-0416. DOI: https://doi.org/10.5194/tc-13-2633-2019.

Shepherd, A. and D. J. Wingham (2007). "Recent Sea-Level Contributions of the Antarctic and Greenland Ice Sheets." In: *Science* 315.5818, pp. 1529–1532. ISSN: 0036-8075, 1095-9203. DOI: 10.1126/science.1136776.

Shepherd, A., D. J. Wingham, and E. Rignot (2004). "Warm Ocean Is Eroding West Antarctic Ice Sheet." In: *Geophysical Research Letters* 31.23. ISSN: 1944-8007. DOI: 10.1029/2004GL021106.

Shepherd, A. et al. (2012). "A Reconciled Estimate of Ice-Sheet Mass Balance." In: *Science* 338.6111, pp. 1183–1189. ISSN: 0036-8075, 1095-9203. DOI: 10.1126/science.1228102.

Shepherd, A. et al. (2018). "Mass Balance of the Antarctic Ice Sheet from 1992 to 2017." In: *Nature* 558, pp. 219–222. DOI: 10.1038/s41586-018-0179-y.

Shepherd, A. et al. (2019). "Mass Balance of the Greenland Ice Sheet from 1992 to 2018." In: *Nature*, pp. 1–7. ISSN: 0028-0836, 1476-4687. DOI: 10.1038/s41586-019-1855-2.

Simonsen, S. B. and L. S. Sørensen (2017). "Implications of Changing Scattering Properties on Greenland Ice Sheet Volume Change from Cryosat-2 Altimetry." In: *Remote Sensing of Environment* 190, pp. 207–216. ISSN: 0034-4257. DOI: 10.1016/j.rse.2016.12.012.

Sole, A. J., T. Payne, J. L. Bamber, P. W. Nienow, and W. Krabill (2008). "Testing Hypotheses of the Cause of Peripheral Thinning of the Greenland Ice Sheet: Is Land-Terminating Ice Thinning at Anomalously High Rates?" In: *The Cryosphere* 2.2, pp. 205–218. ISSN: 1994-0416. DOI: https://doi.org/10.5194/tc-2-205-2008.

Stiles, W. and F. Ulaby (1981). "Dielectric Properties of Snow." In: *Universityof Kansas Center for Research* RSL Technical Report 527-1.

Stocker, T. F., D. Qin, G.-K. Plattner, M. Tignor, S. K. Allen, J. Boschung, A. Nauels, Y. Xia, V. Bex, P. M. Midgley, et al. (2013). *Climate Change 2013: The Physical Science Basis*. Cambridge University Press Cambridge.

Strozzi, T., A. Luckman, T. Murray, U. Wegmuller, and C. Werner (2002). "Glacier Motion Estimation Using SAR Offset-Tracking Procedures." In: *IEEE Transactions on Geoscience and Remote Sensing* 40.11, pp. 2384–2391. ISSN: 1558-0644. DOI: 10.1109/TGRS.2002.805079.

Tapley, B. D., S. Bettadpur, J. C. Ries, P. F. Thompson, and M. M. Watkins (2004). "GRACE Measurements of Mass Variability in the Earth System." In: *Science* 305.5683, pp. 503–505. ISSN: 0036-8075, 1095-9203. DOI: 10.1126/science.1099192.

Tedesco, M., X. Fettweis, T. L. Mote, J. Wahr, P. Alexander, J. E. Box, and B. Wouters (2013). "Evidence and Analysis of 2012 Greenland Records from Spaceborne Observations, a Regional Climate Model and Reanalysis Data." In: *The Cryosphere* 7.2, pp. 615–630. ISSN: 1994-0416. DOI: https://doi.org/10.5194/tc-7-615-2013.

Vallelonga, P. et al. (2014). "Initial Results from Geophysical Surveys and Shallow Coring of the Northeast Greenland Ice Stream (NEGIS)." In: *The Cryosphere* 8.4, pp. 1275–1287. ISSN: 1994-0416. DOI: https://doi.org/10.5194/tc-8-1275-2014.

Vaughan, D. G., J. C. Comiso, I. Allison, J. Carrasco, G. Kaser, R. Kwok, P. Mote, T. Murray, F. Paul, J. Ren, et al. (2013). "Observations: Cryosphere." In: *Climate change* 2013, pp. 317–382.

Veen, C. J. van der (2013). *Fundamentals of Glacier Dynamics*. CRC Press. ISBN: 978-0-429-06380-0. DOI: 10.1201/b14059.

Velicogna, I., T. C. Sutterley, and M. R. van den Broeke (2014). "Regional Acceleration in Ice Mass Loss from Greenland and Antarctica Using GRACE Time-Variable Gravity Data." In: *Geophysical Research Letters* 41.22, pp. 8130–8137. ISSN: 1944-8007. DOI: 10.1002/2014GL061052.

Velicogna, I. and J. Wahr (2005). "Greenland Mass Balance from GRACE." In: *Geophysical Research Letters* 32.18. ISSN: 1944-8007. DOI: 10.1029/2005GL023955.

Vincent, L. and P. Soille (1991). "Watersheds in Digital Spaces: An Efficient Algorithm Based on Immersion Simulations." In: *IEEE Transactions on Pattern Analysis and Machine Intelligence* 13.6, pp. 583–598. ISSN: 0162-8828, 2160-9292, 1939-3539. DOI: 10.1109/34.87344.

Wahr, J., M. Molenaar, and F. Bryan (1998). "Time Variability of the Earth's Gravity Field: Hydrological and Oceanic Effects and Their Possible Detection Using GRACE." In: *Journal of Geophysical Research: Solid Earth* 103.B12, pp. 30205–30229. ISSN: 2156-2202. DOI: 10.1029/98JB02844.

Wake, L. M., B. S. Lecavalier, and M. Bevis (2016). "Glacial Isostatic Adjustment (GIA) in Greenland: A Review." In: *Current Climate Change Reports* 2.3, pp. 101–111. ISSN: 2198-6061. DOI: 10.1007/s40641-016-0040-z.

Weber Hoen, E. and H. Zebker (2000). "Penetration Depths Inferred from Interferometric Volume Decorrelation Observed over the Greenland Ice Sheet." In: *IEEE Transactions on Geoscience and Remote Sensing* 38.6, pp. 2571–2583. ISSN: 0196-2892, 1558-0644. DOI: 10.1109/36.885204.

Wild, C. T., O. J. Marsh, and W. Rack (2019). "Differential Interferometric Synthetic Aperture Radar for Tide Modelling in Antarctic Ice-Shelf Grounding Zones." In: *The Cryosphere* 13.12, pp. 3171–3191. ISSN: 1994-0416. DOI: https://doi.org/10.5194/tc-13-3171-2019.

Williams, R. S., D. K. Hall, and C. S. Benson (1991). "Analysis of Glacier Facies Using Satellite Techniques." In: *Journal of Glaciology* 37.125. ed, pp. 120–128. ISSN: 0022-1430, 1727-5652. DOI: 10.3189/S0022143000042878.

Williams, R. S., J. G. Ferrigno, T. M. Kent, and J. W. Schoonmaker (1982). "Landsat Images and Mosaics of Antarctica for Mapping and Glaciological Studies." In: *Annals of Glaciology* 3. ed, pp. 321–326. ISSN: 0260-3055, 1727-5644. DOI: 10.3189/S0260305500003001.

Willis, M. J., A. K. Melkonian, M. E. Pritchard, and A. Rivera (2012). "Ice Loss from the Southern Patagonian Ice Field, South America, between 2000 and 2012." In: *Geophysical Research Letters* 39.17. ISSN: 1944-8007. DOI: 10.1029/2012GL053136.

Wilson, N., F. Straneo, and P. Heimbach (2017). "Satellite-Derived Submarine Melt Rates and Mass Balance (2011–2015) for Greenland's Largest Remaining Ice Tongues." In: *The Cryosphere* 11.6, pp. 2773–2782. ISSN: 1994-0416. DOI: https://doi.org/10.5194/tc-11-2773-2017.

Wingham, D. J., A. J. Ridout, R. Scharroo, R. J. Arthern, and C. K. Shum (1998). "Antarctic Elevation Change from 1992 to 1996." In: *Science* 282.5388, pp. 456–458. ISSN: 0036-8075, 1095-9203. DOI: 10.1126/science.282.5388.456.

Wingham, D. J. et al. (2006). "CryoSat: A Mission to Determine the Fluctuations in Earth's Land and Marine Ice Fields." In: *Advances in Space Research*. Natural Hazards and Oceanographic Processes from Satellite Data 37.4, pp. 841–871. ISSN: 0273-1177. DOI: 10.1016/j.asr.2005.07.027.

Wright, T. J., B. E. Parsons, and Z. Lu (2004). "Toward Mapping Surface Deformation in Three Dimensions Using InSAR." In: *Geophysical Research Letters* 31.1. ISSN: 1944-8007. DOI: 10.1029/2003GL018827.

Wuite, J., T. Nagler, N. Gourmelen, M. J. Escorihuela, A. E. Hogg, and M. R. Drinkwater (2019). "Sub-Annual Calving Front Migration, Area Change and Calving Rates from Swath Mode CryoSat-2 Altimetry, on Filchner-Ronne Ice Shelf, Antarctica." In: *Remote Sensing* 11.23, p. 2761. DOI: 10.3390/rs11232761.

Zwally, H. J., R. A. Bindschadler, A. C. Brenner, T. V. Martin, and R. H. Thomas (1983). "Surface Elevation Contours of Greenland and Antarctic Ice Sheets." In: *Journal of Geophysical Research: Oceans* 88.C3, pp. 1589–1596. ISSN: 2156-2202. DOI: 10.1029/JC088iC03p01589.

Zwally, H. J., M. B. Giovinetto, M. A. Beckley, and J. L. Saba (2012). *Antarctic and Greenland Drainage Systems, GSFC Cryospheric Sciences Laboratory*. URL: http://icesat4.gsfc.nasa.gov/cryo_data/ant_grn_drainage_systems.php (visited on 10/29/2019).

A

KRIEGER, L., D. FLORICIOIU, AND N. NECKEL (2020). "DRAINAGE BASIN DELINEATION FOR OUTLET GLACIERS OF NORTHEAST GREENLAND BASED ON SENTINEL-1 ICE VELOCITIES AND TANDEM-X ELEVATIONS." IN: REMOTE SENSING OF ENVIRONMENT

The following research was published in

L. Krieger, D. Floricioiu, and N. Neckel (2020). "Drainage Basin Delineation for Outlet Glaciers of Northeast Greenland Based on Sentinel-1 Ice Velocities and TanDEM-X Elevations." In: *Remote Sensing of Environment* 237, p. 111483. ISSN: 0034-4257. DOI: 10.1016/j.rse.2019.111483

ABSTRACT The drainage divides of ice sheets separate the overall glaciated area into multiple sectors. These drainage basins are essential for partitioning mass changes of the ice sheet, as they specify the area over which basin specific measurements are integrated. The delineation of drainage basins on ice sheets is challenging due to their gentle slopes accompanied by local terrain disturbances and complex patterns of ice movement. Until now, in Greenland the basins have been mostly delineated along the major ice divides, which results in large drainage sectors containing multiple outlet glaciers. However, when focusing on measuring glaciological parameters of individual outlet glaciers, more detailed drainage basin delineations are needed. Here we present for the first time a detailed and fully traceable approach that combines ice sheet wide velocity measurements by Sentinel-1 and the high resolution TanDEM-X global DEM to derive individual glacier drainage basins. We delineated catchments for the Northeast Greenland Ice Sheet with a modified watershed algorithm and present results for 31 drainage basins. Even though validation of drainage basins remains a difficult task, we estimated basin probabilities from Monte-Carlo experiments and applied the method to a variety of different ice velocity and DEM datasets finding discrepancies of up to 16% in the extent of catchment areas. The proposed approach has the potential to produce drainage areas for the entirety of the Greenland and Antarctic ice sheets.

INDIVIDUAL CONTRIBUTIONS My individual contributions which are compiled in this cumulative thesis were estimated to account for **90%** of the following publication. They include the specific contributions:

- Literature review and shaping the research question
- Development of the modified watershed algorithm
- Analysis of ice flow directions from DEM and SAR offset tracking
- Processing of the drainage basins for all input dataset combinations
- Coordinating the research
- Writing the manuscript

- Revising the manuscript completely after the first submission

B

KRIEGER, L., U. STRÖSSENREUTHER, V. HELM, D. FLORICIOIU, AND M. HORWATH (2020). "SYNERGISTIC USE OF SINGLE-PASS INTERFEROMETRY AND RADAR ALTIMETRY TO MEASURE MASS LOSS OF NEGIS OUTLET GLACIERS BETWEEN 2011 AND 2014." IN: REMOTE SENSING

The following research was published in

L. Krieger, U. Strößenreuther, V. Helm, D. Floricioiu, and M. Horwath (2020). "Synergistic Use of Single-Pass Interferometry and Radar Altimetry to Measure Mass Loss of NEGIS Outlet Glaciers between 2011 and 2014." In: *Remote Sensing* 12.6, p. 996. DOI: 10.3390/rs12060996

ABSTRACT Mass balances of individual glaciers on ice sheets have been previously reported by forming a mass budget of discharged ice and modelled ice sheet surface mass balance or a complementary method which measures volume changes over the glaciated area that are subsequently converted to glacier mass change. On ice sheets, volume changes have been measured predominantly with radar and laser altimeters but InSAR DEM differencing has also been applied on smaller ice bodies. Here, we report for the first time on the synergistic use of volumetric measurements from the CryoSat-2 radar altimetry mission together with TanDEM-X DEM differencing and calculate the mass balance of the two major outlet glaciers of the Northeast Greenland Ice Stream: Zachariæ Isstrøm and Nioghalvfjerdsfjorden (79North). The glaciers lost $3.59 \pm 1.15\,\mathrm{Gt\,a^{-1}}$ and $1.01 \pm 0.95\,\mathrm{Gt\,a^{-1}}$, respectively, between January 2011 and January 2014. Additionally, there has been substantial sub-aqueous mass loss on Zachariæ Isstrøm of more than $11\,\mathrm{Gt\,a^{-1}}$. We attribute the mass changes on both glaciers to dynamic downwasting. The presented methodology now permits using TanDEM-X bistatic InSAR data in the context of geodetic mass balance investigations for large ice sheet outlet glaciers. In the future, this will allow monitoring the mass changes of dynamic outlet glaciers with high spatial resolution while the superior vertical accuracy of CryoSat-2 can be used for the vast accumulation zones in the ice sheet interior.

INDIVIDUAL CONTRIBUTIONS My individual contributions which are compiled in this cumulative thesis were estimated to account for **70%** of the following publication. They include the specific contributions:

- Literature review and shaping the research question
- Generation of the TanDEM-X surface elevation change maps
- Error assessment of the TanDEM-X surface elevation change
- Correction of SEC with the firn densification model
- SEC validation with Operation IceBridge ATM data
- Error assessment of the mass change

- Comparison of Cryosat-2 and TanDEM-X SEC
- Coordinating the research
- Writing the manuscript

C

MAYER, C., J. SCHAFFER, T. HATTERMANN, D. FLORICIOIU, L. KRIEGER, P. A. DODD, T. KANZOW, C. LICCIULLI, AND C. SCHANNWELL (2018). "LARGE ICE LOSS VARIABILITY AT NIOGHALVFJERDSFJORDEN GLACIER, NORTHEAST-GREENLAND." IN: NATURE COMMUNICATIONS

The following research was published in

C. Mayer, J. Schaffer, T. Hattermann, D. Floricioiu, L. Krieger, P. A. Dodd, T. Kanzow, C. Licciulli, and C. Schannwell (2018). "Large Ice Loss Variability at Nioghalvfjerdsfjorden Glacier, Northeast-Greenland." In: *Nature Communications* 9.1, pp. 1–11. ISSN: 2041-1723. DOI: 10.1038/s41467-018-05180-x

ABSTRACT Nioghalvfjerdsfjorden is a major outlet glacier in Northeast-Greenland. Although earlier studies showed that the floating part near the grounding line thinned by 30% between 1999 and 2014, the temporal ice loss evolution, its relation to external forcing and the implications for the grounded ice sheet remain largely unclear. By combining observations of surface features, ice thickness and bedrock data, we find that the ice shelf mass balance has been out of equilibrium since 2001, with large variations of the thinning rates on annual/multiannual time scales. Changes in ice flux and surface ablation are too small to produce this variability. An increased ocean heat flux is the most plausible cause of the observed thinning. For sustained environmental conditions, the ice shelf will lose large parts of its area within a few decades and ice modeling shows a significant, but locally restricted thinning upstream of the grounding line in response.

INDIVIDUAL CONTRIBUTIONS My individual contributions which are compiled in this cumulative thesis were estimated to account for **10%** of the following publication. They include the specific contributions:

- Proposal Submission for the TanDEM-X global DEM (for the access to the 12m tiles over NE Greenland)
- Interferometric processing of all TanDEM-X CoSSCs needed for the paper into DEMs
- Vertical co-registration of all TanDEM-X DEMs from CoSSCs
- Calculation of the buoyancy derived thickness changes of the floating ice tongue from TanDEM- X elevations
- Error analysis of the TanDEM-X derived thickness changes of the floating ice tongue
- Writing the TanDEM-X related parts of the manuscript
- Providing suggestions on revising the manuscript

D

KEHRL, L. M., I. R. JOUGHIN, D. E. SHEAN, D. FLORICIOIU, AND L. KRIEGER (2017). "SEASONAL AND INTERANNUAL VARIABILITIES IN TERMINUS POSITION, GLACIER VELOCITY, AND SURFACE ELEVATION AT HELHEIM AND KANGERLUSSUAQ GLACIERS FROM 2008 TO 2016." IN: JOURNAL OF GEOPHYSICAL RESEARCH: EARTH SURFACE

The following research was published in

L. M. Kehrl, I. R. Joughin, D. E. Shean, D. Floricioiu, and L. Krieger (2017). "Seasonal and Interannual Variabilities in Terminus Position, Glacier Velocity, and Surface Elevation at Helheim and Kangerlussuaq Glaciers from 2008 to 2016." In: *Journal of Geophysical Research: Earth Surface* 122.9, pp. 1635–1652. ISSN: 2169-9011. DOI: 10.1002/2016JF004133

ABSTRACT The dynamic response of Greenland tidewater glaciers to oceanic and atmospheric change has varied both spatially and temporally. While some of this variability is likely related to regional climate signals, glacier geometry also appears to be important. In this study, we investigated the environmental and geometric controls on the seasonal and interannual evolution of Helheim and Kangerlussuaq Glaciers, Southeast Greenland, from 2008 to 2016, by combining year-round, satellite measurements of terminus position, glacier velocity, and surface elevation. While Helheim remained relatively stable with a lightly grounded terminus over this time period, Kangerlussuaq continued to lose mass as its grounding line retreated into deeper water. By summer 2011, Kangerlussuaq's grounding line had retreated into shallower water, and the glacier had an ~5 km long floating ice tongue. We also observed seasonal variations in surface velocity and elevation at both glaciers. At Helheim, seasonal speedups and dynamic thinning occurred in the late summer when the terminus was most retreated. At Kangerlussuaq, we observed summer speedups due to surface-melt-induced basal lubrication and winter speedups due to ice-shelf retreat. We suggest that Helheim and Kangerlussuaq behaved differently on a seasonal timescale due to differences in the spatial extent of floating ice near their termini, which affected iceberg-calving behavior. Given that seasonal speedups and dynamic thinning can alter this spatial extent, these variations may be important for understanding the long-term evolution of these and other Greenland tidewater glaciers.

INDIVIDUAL CONTRIBUTIONS My individual contributions which are compiled in this cumulative thesis were estimated to account for **5%** of the following publication. They include the specific contributions:

- Reading the manuscript
- Writing the TanDEM-X related part of the manuscript
- Processing of TanDEM-X CoSSC data to DEMs
- Performing the vertical co-registration of the TanDEM-X data

- Performing the phase offset correction of the TanDEM-X data

E

KRIEGER, L. AND D. FLORICIOIU (2017). "AUTOMATIC GLACIER CALVING FRONT DELINEATION ON TERRASAR-X AND SENTINEL-1 SAR IMAGERY." IN: 2017 IEEE INTERNATIONAL GEOSCIENCE AND REMOTE SENSING SYMPOSIUM (IGARSS)

The following research was published in

L. Krieger and D. Floricioiu (2017). "Automatic Glacier Calving Front Delineation on TerraSAR-X and Sentinel-1 SAR Imagery." In: *2017 IEEE International Geoscience and Remote Sensing Symposium (IGARSS)*. 2017 IEEE International Geoscience and Remote Sensing Symposium (IGARSS), pp. 2817–2820. DOI: 10.1109/IGARSS.2017.8127584

ABSTRACT This paper presents an approach for automatic calving front delineation of marine-terminating outlet glaciers. We utilize a Canny edge detection approach together with a shortest path optimization problem to find calving front locations (CFL) on SAR backscattering images from Sentinel-1 and TerraSAR-X. The CFLs are detected on Stripmap images acquired over Zachariæ Isstrøm in Northeast Greenland where difficult conditions for CFL retrieval exist. We compare our results to CFLs that are delineated by hand and find good agreement, independent of the used sensor.

INDIVIDUAL CONTRIBUTIONS My individual contributions which are compiled in this cumulative thesis were estimated to account for **90%** of the following publication. They include the specific contributions:

- Conceiving and designing the algorithm to delineate calving fronts on SAR amplitude backscattering images
- Download and preparation of the used SAR imagery
- Writing the manuscript

F

KRIEGER, L. AND D. FLORICIOIU (2019). "IMPROVED DELINEATION OF INDIVIDUAL OUTLET GLACIER DRAINAGE BASINS FROM TANDEM-X ELEVATIONS AND SENTINEL-1 VELOCITIES." IN: 2019 IEEE INTERNATIONAL GEOSCIENCE AND REMOTE SENSING SYMPOSIUM (IGARSS)

The following research was published in

L. Krieger and D. Floricioiu (2019). "Improved Delineation of Individual Outlet Glacier Drainage Basins From Tandem-X Elevations And Sentinel-1 Velocities." In: *IGARSS 2019 - 2019 IEEE International Geoscience and Remote Sensing Symposium*. IGARSS 2019 - 2019 IEEE International Geoscience and Remote Sensing Symposium, pp. 3998–4001. DOI: 10.1109/IGARSS.2019.8897921

ABSTRACT Individual drainage basins of ice sheets specify the glaciated area that is drained by a single outlet glacier. These catchments are needed to partition mass balance measurements to the single glacier level. Until now complete glacier inventories that contain annotated basin information are missing for the Earth's two ice sheets. Here we present delineations of all major outlet glacier catchments in Northeast Greenland that have been produced by a modified watershed algorithm using TanDEM-X elevations and Sentinel-1 velocity measurements. The approach shows the potential to generate a complete basin inventory for entire Greenland and Antarctica.

INDIVIDUAL CONTRIBUTIONS My individual contributions which are compiled in this cumulative thesis were estimated to account for **90%** of the following publication. They include the specific contributions:

- Conceiving and designing the modified watershed algorithm
- Development of the modified watershed algorithm
- Analysis of ice flow directions from DEM and SAR offset tracking
- Processing of the drainage basins for all input dataset combinations
- Writing the manuscript